MEASUREMENTS IN A COMPRESSIBLE PLANAR SHEAR LAYER WITH A THERMAL GRADIENT

BY

NICHOLAS JOSEPH TYMKIW

THESIS

Submitted in partial fulfillment of the requirements
for the degree of Master of Science in Aerospace Engineering
in the Graduate College of the
University of Illinois at Urbana-Champaign, 2021

Urbana, Illinois

Advisors:

Professor J. Craig Dutton
Professor Gregory S. Elliott

ABSTRACT

Experiments on a compressible planar shear layer with a sharp thermal gradient between the mixing streams were conducted with the goal of adding to a set of benchmark computational fluid dynamics validation datasets for unheated mixing layers as well as obtaining the first temperature measurements within this kind of shear layer. The shear layer itself was a dual-stream air mixing layer with a convective Mach number of 0.541 and a stagnation temperature difference of about 200 K between the streams. A preexisting mixing layer facility was modified to provide for the addition of the heated stream while maintaining the original operational capacities of the facility. Three-component velocity fields along the central streamwise-transverse plane of the shear layer were obtained through the use of stereo-particle image velocimetry. Even with the novel stagnation temperature gradient, it was found that there were minor to negligible effects on the turbulence or mean velocity fields compared to previous similar investigations into the compressible shear layer, albeit with a higher shear layer growth rate. Temperature probe traverses throughout the shear layer were obtained at different streamwise points, as well as static pressure measurements along the entire test section side-wall. Schlieren visualizations in the form of high-speed videos as well as instantaneous images were also obtained, giving additional qualitative insight. Temperature field measurements were made via Filtered Rayleigh Scattering along the central streamwise-transverse plane, and the mean transverse profiles of those temperature fields calculated. It was found that the temperature field of the thermal mixing layer becomes fully self-similar much closer to the splitter plate in the streamwise direction than that of the velocity field. This work provides a basis for future studies to build upon and to further investigate compressible shear layers with gradients in stagnation temperature between the streams.

ACKNOWLEDGEMENTS

This project was supported by the D.3 Transformation Tools and Technologies Project (TTT1) issued by NASA Headquarters: Award No. NNX15AU94A. I wish to thank the project technical managers at NASA Glenn Research Center for their assistance, especially Jim DeBonis.

Of course, beyond the funding, this research project never would have occurred had it not been for the insight and guidance given by my advisors, Professor Craig Dutton and Professor Gregory Elliott. Your continued patience, direction, advice, and understanding throughout these past two-and-a-half years have been invaluable to my growth not only as a researcher and graduate student, but as a person as well. I cannot thank you sufficiently; I am humbled to have known you.

To my colleagues in the Gas Dynamics group: Kevin Kim, Branden Kirchner, Matt Koll, Gyu-Sub Lee, and Griffin Bojan: it's been a fun ride. Thank you for always being willing to lend a hand, or even just your ear. From my first day in the office, I enjoyed the camaraderie that you all have maintained, and I could not have completed my work if not for the many discussions and help you have given throughout the years. To Kevin especially, who taught me how to use the tunnel as well as the many arts of stereo-PIV: I cannot thank you enough. I must also thank those undergraduates who have helped me along the way, Matt Dickinson and Aman Agrawal—you both tolerated my idiosyncrasies and were always willing to come work in the tunnel and take "just one more data run," and for that I am eternally grateful.

I last turn my thanks to my family, from whom I always found support, solace, and love. To my wife, Emma, I thank you for never failing to inspire my best work, helping me when I am down, and unconditionally believing in me. To my parents, thank you for nurturing me throughout the years, even when you didn't understand what I was telling you: it is only through you that I could be where I am today.

TABLE OF CONTENTS

CHAPTER 1: INTRODUCTION

1.1 Background

1.1.1 Previous Experimental Planar Shear Layer Studies

The work of Brown and Roshko (1974)[1] is the fundamental study in the planar mixing world, setting the foundation for all future work. Their experiment compared a series of incompressible mixing layer flows with verying density differentials between the two flows; originally their intent was to study the effects of the density difference on turbulent mixing, but the study revealed much more about the flow structure itself. Of particular note was their discovery that compressibility effects were separate from the effects of the density ratio at low Mach numbers. However, they do note that compressible flows have the capacity to introduce new effects that may tie into the effects of the density ratio.

Continued work on the mixing layer led to the compressibility parameter definition by Bogdanoff (1983)[2] and Papamouschou and Roshko (1988)[3] of the convective Mach number, M_c, by arguing that the two streams have a shared stagnation point in the mixing layer. In cases where the static pressures are equivalent between the streams and the gases are identical in composition, M_c can be defined as shown in Equation (1), where U_1 and U_2 are the two freestream velocities in the streamwise direction and a_1 and a_2 their respective speeds of sound. This definition is quite easy to determine in all studies, both computational and experimental, and therefore has been widely adopted in the literature, including this one.

$$M_c = \frac{U_1 - U_2}{a_1 + a_2} \tag{1}$$

The shear layer thickness itself, b, has been variously defined depending on the experimentalist, study, and measurement method in use (as well as the mood of the researchers). For this study, the 10% ΔU thickness is utilized, defined as the transverse distance between two

points in the flow y_1 and y_2, where ΔU is the difference in the freestream velocities U_1 and U_2, y_1 is the location at which the mean velocity is $U_1 - 0.1\Delta U$ and y_2 is the location at which the velocity is $U_2 + 0.1\Delta U$. Other approaches have included the vorticity thickness and the visual thickness; the 10% ΔU definition is most typically used in velocimetry studies of the mixing layer such as this one.

The growth rate of the shear layer, $^{db}/_{dx}$, has been of great interest in many of the studies, including the oldest experiments. Early on researchers used a similarity variable, dependent on the velocity ratio r (U_2/U_1), to collapse the growth rate to a linear function, as borne out in Sabin (1965)[4]; Brown and Roshko[1], for instance, use this parameter for their work. However, all of the works using this similarity variable assumed uniform density; for the experiment of interest here, as well as others in the past, a more robust function was required. Papamoschou and Roshko (1988) argued for a proportional growth rate for incompressible mixing layers related to the differential velocity ΔU divided by the convective velocity U_c that accounted for the difference in density. Their equation, for a variable-density shear layer, is given below in Equation (2). [3]

$$\frac{db}{dx}\Big|_0 = c\,\frac{(1-r)(1-\sqrt{s})}{1+r\sqrt{s}} \tag{2}$$

The constant of proportionality in Equation (2), c, was determined to be 0.165/2 by Goebel and Dutton (1991)[5]; this relation has borne out well for experimental studies of incompressible shear layers. As many studies of shear layers are incompressible, the easiest method of comparing compressible growth rates of all studies is to normalize by this term, as was performed by Barre and Bonnet (2015)[6] or Kim et al. (2019)[7]. The work of Kim is of particular interest to this study, as it was the previous work performed in the same facility, and it is discussed in greater detail in Section 1.1.3.

1.1.2 Mixing Enhancement in the Shear Layer

The mixing within the shear layer is of particular interest from an application-based perspective. Enhancement of the mixing process is highly desired in combustion applications, especially for those of novel or limited geometries. Supersonic combustors may find particular relevance in studies such as this, where the effects of injector and flameholder geometry have major impact on the viability of designs. Scramjets in particular suffer from short residence times of the oxidizer/fuel mixture within the combustion chamber itself as well as poor entrainment of the fuel/flame mixture into the freestream. Vorticity and recirculation, then, are central to such applications: given that these effects are dominant in the mixing layer, its enhancement, therefore, is of paramount importance.[8,9]

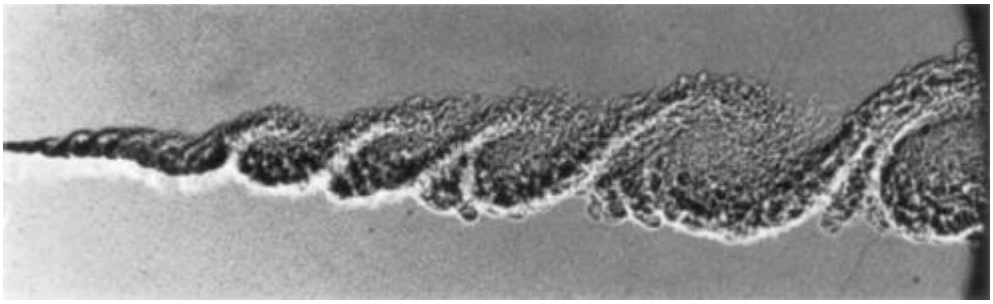

Figure 1. Shadowgraph from Brown and Roshko (1974) showing large-scale structures in a gaseous mixing layer[1]

Large-scale structures within the mixing layer, at lower convective Mach numbers, are the most easily understood features relating to the enhancement. However, as multiple studies have shown in schlieren visualizations[2,3,5,7], the large-scale structures as seen by Brown & Roshko[1] above in Figure 1 reduce in size and organization as the compressibility increases to become more like those as visualized by Rossman et al. (2002) in Figure 2 on the following page.[10] Smaller and less coherent structures, then, must be investigated for increasing the efficacy of the mixing layer at higher compressibility. Abraham and Magi (1997) performed DNS simulations of an incompressible mixing layer with differing density ratios. As the density ratio *s* increased in their

study, the spatial mixing layer growth rate slowed. This effect on the growth rate was inferred to be due to a faster effective mean velocity in the mixing layer; however, they posited its effects also may be highly influenced by instabilities at the interface between the mixing layer and freestreams[11]. For mixing enhancement into the freestreams, Zhang et al. (2015) studied the effects of oblique shocks on the mixing layer and moreover its Reynolds stresses. The oblique shocks for their LES of a weakly compressible (M_c = 0.3) planar shear layer were found to modulate the growth rate of the shear layer as well as locally incline the layer as it progressed downstream. They additionally found that there was local enhancement in the vorticity of the flowfield around the shocks, and intensification of the turbulent kinetic energy and transverse Reynolds normal stress.[12]

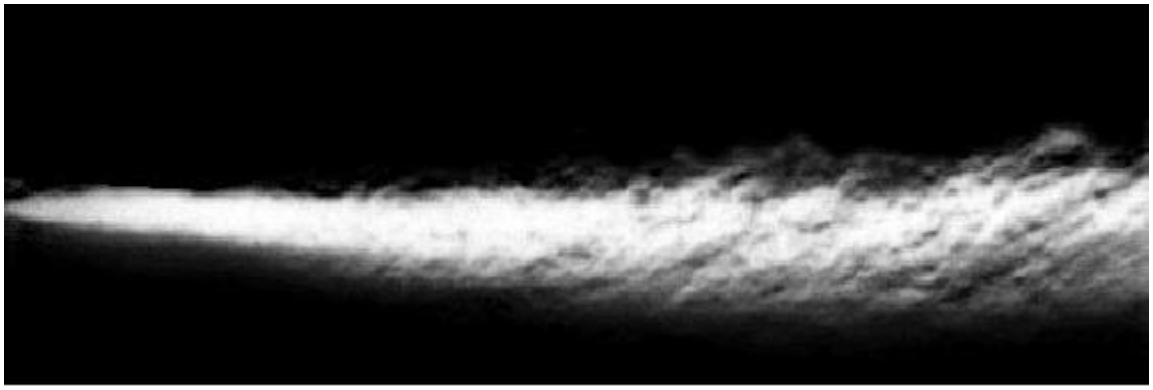

Figure 2. Schlieren of Rossman et al. (2002) for an M_c = 0.86 condition[10]

1.1.3 Recent Work at UIUC on the Compressible Mixing Layer

As noted in Section 1.1.1, the wind tunnel facility of the current investigation has already been used for previous planar mixing experiments. Kim et al. have performed a multitude of experiments and analyses on mixing layers with M_c ranging from 0.19 to 0.88, with all cases save one involving a supersonic primary stream. Large ensembles of stereo-PIV measurements were gathered, with an emphasis on confirmation of fully-developed, self-similar mean velocity and Reynolds stress conditions. Furthermore, this dataset was of high enough quality (and low enough uncertainty) that higher-order moment results (including third- and fourth-order moments) were

obtainable for all cases studied. The evolution of the large-scale structures was also of interest in the studies, particularly with respect to the growth of the mixing layer and trends in turbulence development.[7,13-15]

In short, this dataset was used to determine trends of the entire (three-dimensional) Reynolds stress tensor, production trend and length scales of the turbulence, and entrainment mechanisms. Fundamentally, one of the most important trends to come from Kim's work was the confirmation that the streamwise-normal Reynolds stress remains constant as M_c increases. This discovery, stemming from the study's ability to consistently and clearly obtain fully-developed, self-similar conditions in the fully-developed region, is crucial, laying to rest a debate spanning the better part of three decades on the behavior of the streamwise-normal Reynolds stress with compressibility. Furthermore, by taking high-quality data of the entire stress tensor, it was discovered that the spanwise-normal Reynolds stress decreases monotonically with M_c, relative to the incompressible mixing layer value. From overall consideration of the Reynolds stress trends, it was also found that the turbulence production definitively decreases with increasing M_c; confirming the earlier results of CFD studies by Freund et al. (2000) and Pantano and Sarkar (2002).[16,17] It was further shown that as the compressibility increases in the mixing layer, the streamwise and transverse fluctuations both increase in length scale, while the length scale of the transverse fluctuations decreases, giving a more "flattened" planar shear layer. The entrainment into the shear layer, investigated through analyses including proper orthogonal decomposition to determine the modes of the entire mixing layer, as well as local analyses of the normal velocity component along the interface, indicate that larger length-scale mechanisms such as engulfment are more common in lower compressibility cases, while smaller-scale mechanisms begin to dominate as the compressibility rises. Furthermore, the boundary along the lower-velocity

secondary freestream was shown to consistently have larger- and longer-scale mechanisms compared to the higher-speed primary stream boundary. These findings are in self-agreement with each other, especially with respect to the streamwise-normal Reynolds stress trend: by damping out the higher-amplitude larger structures as the compressibility rises, the fluctuations are only able to grow at the same relative rate as the difference in freestream velocities. This understanding also provides a compelling reason for the previously found inhibition of the mixing layer growth rate at higher M_c.[14]

It is from discussions related to the work of Kim et al. that this study was born, as a corollary to a specific case he studied with $M_c = 0.69$. For further discussion, much deeper than it is of benefit to delve into for the current work, the reader is directed to Kim's doctoral dissertation, which is the best current summary of his work studying the supersonic compressible mixing layer.[14] It should be noted that while all cases that Kim studied were of practically equivalent stagnation temperatures between the flows, the case of interest here rather calls for a major difference in the stagnation temperatures of the two streams.

1.2 The Filtered Rayleigh Scattering Technique

1.2.1 Filtered Rayleigh Scattering Theory

For the temperature measurements within the test section, an optical diagnostic technique known as filtered Rayleigh Scattering (FRS) was utilized. This technique, best described in the work of Forkey et al. (1996)[18] (coincidentally, published in the same year this author was born), utilizes the elastic Rayleigh scattering effect from molecules in the flow to determine the velocity, temperature, and pressure of the area of interest. Undesirable background and Mie scattering are filtered from the signal by an absorption cell that acts as a molecular notch filter, given a laser tuned to a specific frequency. The Rayleigh scattered light is broadened from the laser profile and

is able to transmit through the filter; it is then imaged on the camera. FRS, then, is a technique most commonly applied when in use in a particle-laden or otherwise dirty flow; the filter greatly reduces the noise that any particulates would otherwise cause.

$$S = C\left[\int_{-\infty}^{\infty} R_{gas} t(f) df + \int_{-\infty}^{\infty} R_{bg} t(f) df\right] \quad (3)$$

The signal *S* as imaged onto the sensor of the camera is the raw data of interest in an FRS experiment. Equation (3) above shows the formulation in full, where R_{gas} is the Rayleigh signal of the medium, R_{bg} is the background Rayleigh signal from stray scattering, $t(f)$ is the transmission function of the absorption filter at an arbitrary frequency, and *C* is a constant value for the imaging environment, including the camera sensor and lens system.

When a laser pulse with uniform spatial profile and frequency f_L interacts with the air, it scatters in the form of a Rayleigh signal that is a function of the composition of the gas. This Rayleigh signal is an integral sum of the signals individually scattered from each molecule present into the solid angle $d\Omega$, scaled by their mole fraction χ_i and Rayleigh cross-section σ_i[19], as shown in Equation (4).

$$R_{gas} = E_l \frac{PV}{kT} \frac{\mathrm{d}\sigma}{\mathrm{d}\Omega} \mathrm{d}\Omega \times \int_{-\infty}^{\infty} [l(f - [f_L + f_D] - f') \times g(Y, f')] \mathrm{d}f' \quad (4)$$

Each Rayleigh signal is the integral of the convolution of the laser lineshape *l* with an input amplitude E_l and the entire Rayleigh-Brillouin scattering profile $g(Y,f)$, and is well characterized by the *Y* parameter defined by Tenti et al.[20] and shown in Equation (5)

$$Y = \frac{nkT}{\sqrt{2} K v_0 \mu} \quad (5)$$

where *n* is the gas number density, μ the viscosity, v_0 the molecular thermal velocity, and *K* the magnitude of the scattering wave vector given in Equation (6).

$$K = \frac{4\pi}{\lambda} \sin\left(\frac{\theta}{2}\right) \quad (6)$$

The Tenti *Y* parameter is the measure of the ratio of the scattering wavelength to the molecular mean free path.[20] It is also important to note that the scattering profile is frequency shifted relative to the incoming laser profile due to the Doppler shift, given by Equation (7)

$$v_D = \frac{2v}{\lambda} \sin\left(\frac{\theta}{2}\right) \tag{7}$$

where v is the flow velocity along the line bisecting the laser propagation vector and the pointing vector of the camera, λ is the incoming vacuum wavelength of the laser sheet, and θ the scattering angle.[21] This in turn gives the shifted central frequency *f'* of the Rayleigh signal; by virtue of the Doppler shift the Rayleigh signal typically is less affected by the absorption filter and is therefore stronger with increasing velocity. Figure 3 shows computed Filtered Rayleigh signals for a simplified air (N_2 – O_2) model with different velocities and temperatures; note that the center of the Rayleigh signal changes with increased velocity, and that the width of the profile increases. This increased width, known as thermal Doppler broadening, comes from its higher energy state (that is, a higher temperature) having an increased-width Maxwell distribution of its velocity, causing the Doppler effect on the motion of the individual molecules to correspondingly broaden.

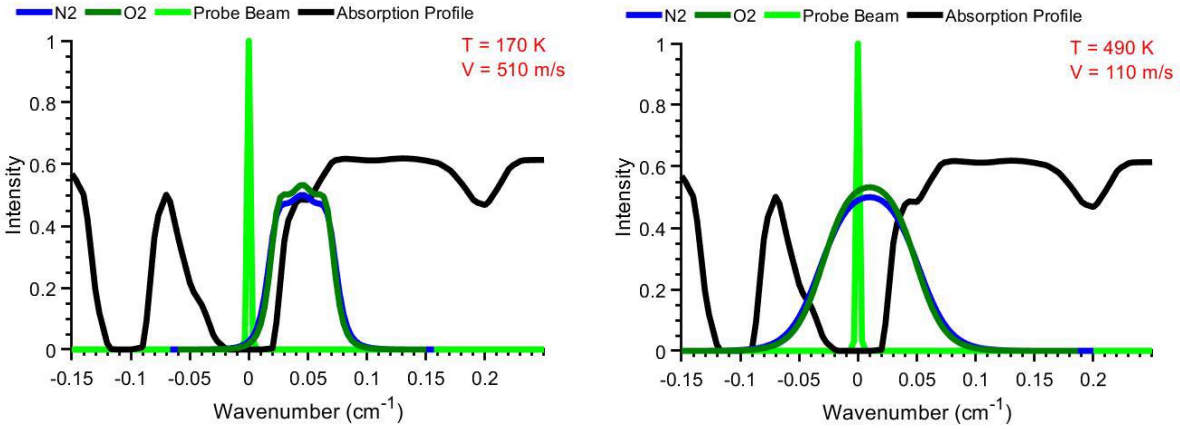

Figure 3. Computed FRS signal profiles for given temperature and velocity

The additional Rayleigh scattering from stationary objects in the imaged field of view from windows, walls, and other objects in the background may be calculated in the same way. Their

signals are of the same frequency as the laser, however, and as stated above, are almost entirely absorbed by the filter. Their contribution is therefore entirely dependent on the laser frequency and as a result the filter transmission function; for a consistent laser frequency, the background signal may be assumed to be the same between shots. For many approaches, including the current one, the filter is one of molecular iodine, which has multiple usable absorption lines around the central frequency of a frequency-doubled Nd:YAG laser. Given the transmission of the laser lineshape through a second reference filter, the location in frequency space may be found for each laser shot.

For this work, the technique is further simplified in that the velocity may be assumed to be known from another technique—that is, the particle image velocimetry (PIV) data. Furthermore, the pressure of the flow is assumed to be relatively constant and known from measurements made while monitoring the tunnel. The system of equations that affects the received signal may then be thought of as a system in which two values are known and constant throughout (f_L, P), one is known and varies based on location (V), and one is unknown and therefore may be solved for based on the received signal S: the temperature T. By normalizing by the reference signal value of the flatfield, taken at ambient conditions of temperature, pressure, and velocity, a simple relation may be obtained that yields directly the temperature based on the grayscale value of each pixel on the image sensor. This can be summarized in Equation (8)

$$\frac{S(f\prime)}{S_{ref}(f)} = \frac{T_{ref}}{T}\frac{P}{P_{ref}}C_1 + C_2 \tag{8}$$

where Equations (3 & 4) have been combined and simplified given the reference values. From this relation, it is trivial to determine the temperature at each pixel given its normalized signal, the reference temperature and pressure, and the flow-on pressure and velocity, especially in the current application, where calibration constants C_1 and C_2 are applied to fit the signal response of the camera to the known temperature values in the freestreams.

1.2.2 Application of Filtered Rayleigh Scattering

Filtered Rayleigh scattering work has been achieved previously for a wide variety of flows, including the compressible shear layer. Forkey et al. made planar velocity, pressure, and temperature measurement in a Mach 2 free jet for their work.[18] Other early works focused primarily on velocity measurements using the technique, such as in Elliott et al. (1992) where velocities in compressible mixing layers were measured with the technique[22], and Miles et al. (1992) which first demonstrated FRS with iodine filters with an Nd:YAG laser while investigating the boundary layer structure in Mach 3 and Mach 5 flows[23]. The latter work was later extended by Forkey et al. (1994) where supersonic boundary layers were further imaged.[24]

The work of Forkey et al. (1996) is best known, then, for being the initial paper describing the multiple-property measurement capability of the FRS technique. This work, it should be stated, was in a fairly ideal environment—with a well-defined, clean flow and a simple setup to apply calibrations to the background.[18] The use of the technique in its most effectual environment, a sooted combustion case, came with the work of Elliott et al. (1997), as temperature field measurements were obtained in two different premixed flames from multiple burners.[25]

Extension of the FRS technique has come in multiple forms. Work by Boguszko, Elliott, and Huffman in the first decade of the 2000s at UIUC obtained multiple property measurements through the use of angularly resolved FRS, which they called FARRS; this was intended to reduce the uncertainty of the measurement by curve-fitting the effect of off-angle imaging on the relative intensity.[26-29] At around the same time, Most and Leipertz (2001) used the molecular filter to great effect, allowing simultaneous PIV measurements while using FRS to determine the thermodynamic state of their premixed flame.[30] This approach has been utilized in multiple recent studies by McManus and Sutton, where they have used joint FRS and stereo-PIV measurements to

obtain single-shot temperature and velocity measurements in non-premixed flames.[31-33] Such an approach indicates a possible future of FRS, where it is used in conjunction with particle-based methods in order to take advantage of the latter's lessened uncertainty for velocity, while being able to determine the thermodynamic state of the molecules in environments unsuitable for other techniques.

1.3 Current Work

Given past and recent work on supersonic compressible mixing layers, especially that of Kim et al., it was necessary to investigate an area that had, until the beginning of this study, been neglected: a thermal difference in non-reacting mixing layers. It is not unreasonable that until this work it had not been studied: after all, it fits in a regime between supersonic mixing studies closest to reality (either two flows mixing and reacting, or a reacting flow mixing with a nonreacting flow), or simplest to model and study (no reaction, but at high speed). On the other hand, work has been done in studying thermally buoyant flows: ones whose speeds were very slow, albeit with strong thermal differentials, but where the dominant forces are not at all the same. Therefore, it is prudent to investigate such a case where the supersonic mixing layer is influenced by such a thermal difference.

From such an impetus, studies of velocity, density, and temperatures were taken with multiple different measurement methods in a compressible mixing layer with a primary stream of supersonic Mach number and ambient stagnation temperature and a secondary stream of subsonic yet weakly compressible Mach number and significantly elevated stagnation temperature. This case was studied using multiple different methods, including stereoscopic-particle image velocimetry (SPIV), stagnation temperature probe traversals, and Filtered Rayleigh Scattering (FRS), the first work of its kind for a heated mixing layer with a stagnation temperature differential.

While neither the methods used nor the experiment itself are groundbreaking or wholly encompassing by themselves, this work on the whole serves to provide a foundation for future research in identifying the challenges and initial effects of interest, giving the studies to come an initial point from which to build more holistic studies.

The remainder of this thesis is laid out in the following manner. Chapter 2 describes the facility used for the supersonic thermal mixing layer studies and outlines the utilized experimental measurement techniques. Chapter 3 discusses the results stemming from the classical measurement methods: schlieren visualizations, static-pressure measurements, and total air temperature probe traverses. Chapter 4 entails the stereo particle image velocimetry results, including the incoming boundary layers and mean velocity and turbulence analysis. Chapter 5 summarizes the Filtered Rayleigh Scattering thermometry work, to include the mean transverse temperature profiles as well as the temperature fields. The work is then summarized in Chapter 6, the conclusion.

CHAPTER 2: EXPERIMENTAL METHODOLOGIES

This chapter details the facility, experimental approaches and setups, and difficulties encountered therein while obtaining data to fully document (to the state-of-the-art) the flow phenomena of interest in the heated, compressible mixing layer. Project CAD files are available at the project website (https://wiki.illinois.edu/wiki/display/NCSLF) in PTC Creo format, including previous drawings of the wind tunnel facility; renderings are included for clarity.

2.1 Wind Tunnel Facility

The wind tunnel facility, located in the Gas Dynamics Lab within the Aerodynamics Research Laboratory at the University of Illinois at Urbana-Champaign, was designed to allow the investigation of different convective Mach number cases in compressible mixing layers. The facility is a blowdown wind tunnel, fed by a low-pressure line nominally charged to 150 psi, held in a tank farm of volume 4660 ft^3. The design, construction, and testing of the wind tunnel were performed by Gyu-Sub Lee as his Master's thesis; five convective Mach number cases were implemented in the facility during this time by utilizing a replaceable nozzle design. Details of the tunnel that exceed what is discussed in this section may be found in his thesis, to include the initial structural and safety analyses of the facility.[34] The discussion here will rather entail the *modifications* that were made to the preexisting facility in order to enable the heated mixing layer experiment.

Two air streams, both taken from the low-pressure-line, are mixed after traveling lengthwise along a "splitter plate" through respective nozzles. The first, "primary" stream, is of a higher inlet Mach number, meets with a "secondary" stream, which is at a lower Mach number and in this application a higher stagnation temperature. In this instance, the nozzles used are nominally Mach 2.0 and Mach 0.3 for the primary and secondary streams, respectively. The air

flow to the streams themselves is modulated by a main gate valve as seen in Figure 4 below. The flow then splits off of a tee and flows to the primary and secondary inlets of the tunnel separately. The primary stream has a pneumatic valve to act as a safety backup to the tunnel, but otherwise flows directly to the wind tunnel; when the tunnel is in operation, the pneumatic valve is set fully open. The secondary stream is modulated by a second gate valve that limits the flow through to the electric heater. The heater brings the stagnation temperature of the secondary air to the target stagnation temperature of 495 K as it flows through; it then enters the tunnel after this process. Successful operation of the mixing layer tunnel is predicated upon reliably matching the static pressures of the two streams downstream in the test section; this is achieved by measuring a differential static pressure between the two streams just prior to the splitter tip.

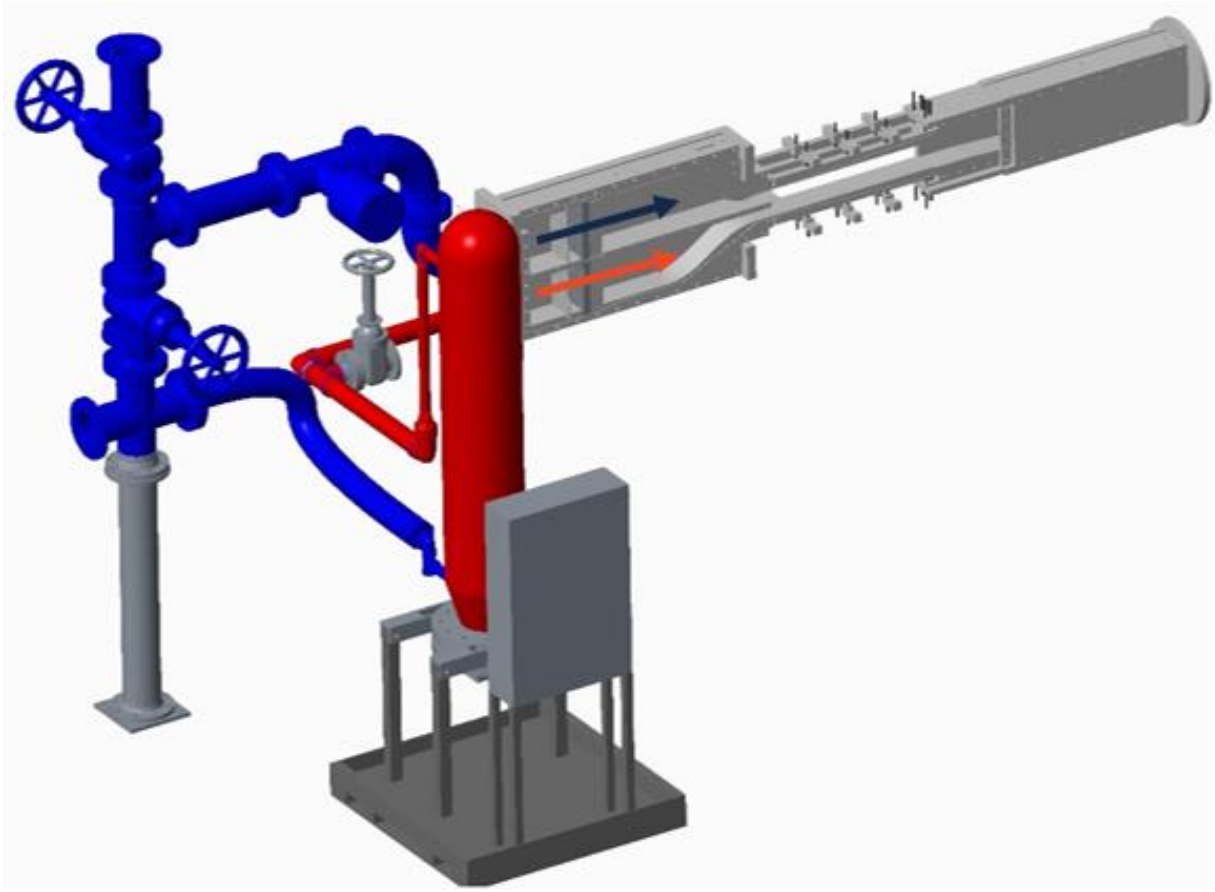

Figure 4. CAD rendering of wind tunnel facility (with ambient temperature stream in blue and heated stream in red)

Monitoring and overall operation of the tunnel are performed through a LabVIEW virtual instrument (VI) that pulls in pressure and temperature data pertinent to the facility. Further details on the pressure- and temperature-monitoring capability displayed on the front panel (which is seen in Figure 5) are given in Section 2.2.1. The VI controls the startup and shutdown of the tunnel through the pneumatic valve by virtue of a 20 mA signal via a National Instruments 9265 current output module. The VI also monitors the status of the laser system when it is in use.

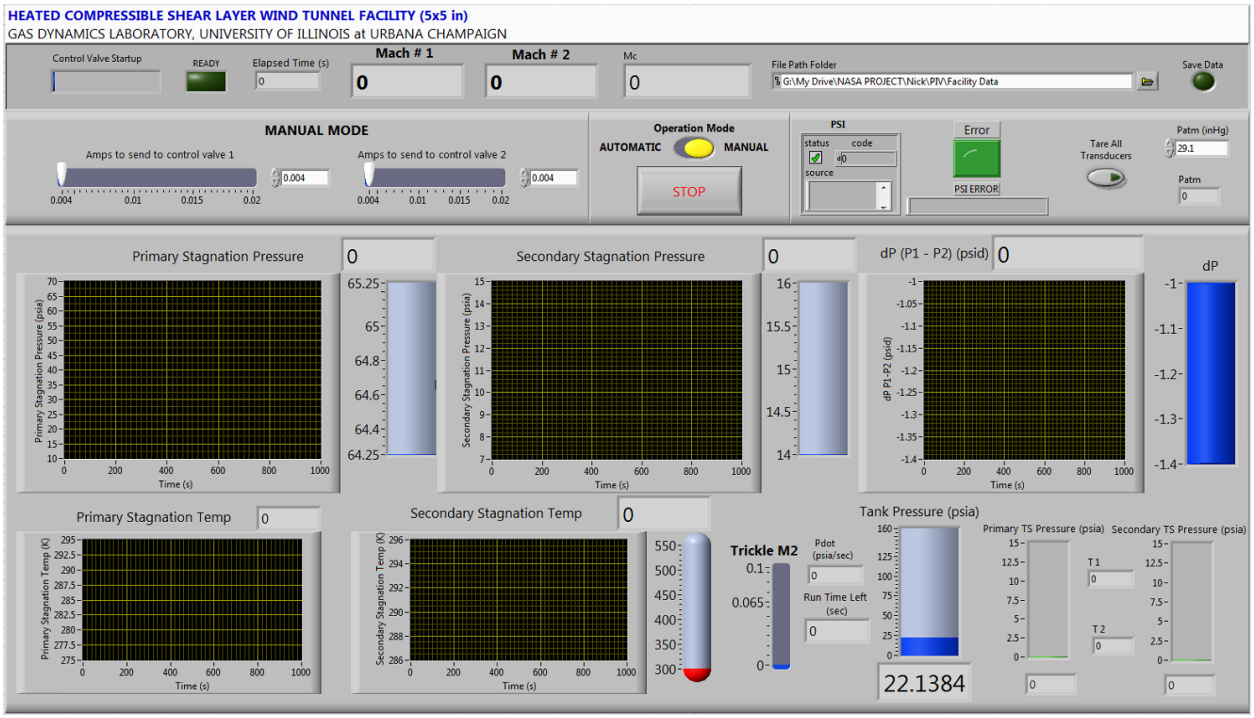

Figure 5. LabVIEW VI front panel

The facility was designed to support many methods of flow analysis, primarily that of optical, nonintrusive techniques: stereo particle image velocimetry (SPIV) and schlieren visualization were of particular interest at its conception, with later extension to filtered Rayleigh scattering (FRS). At the same time, it allows for traditional measurements as well: static pressure measurements along both freestreams and down the test section centerline, and pitot-static probe analysis at various streamwise station. Probe traces may also be made with the replacement of

either the top or bottom wall of the wind tunnel test section; this includes pitot-static and hot-wire anemometry, as well as total air temperature thermocouple measurements.

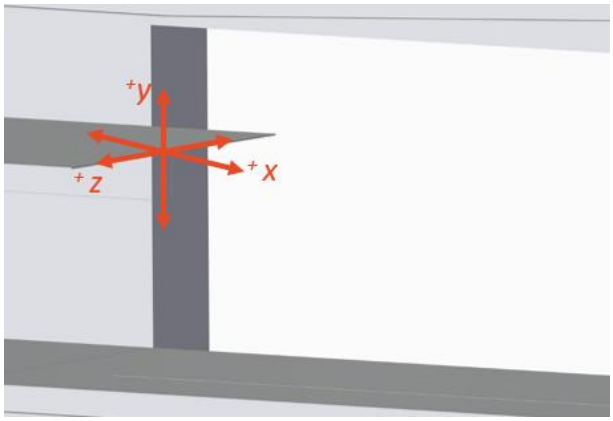

Figure 6. Laboratory reference frame

All measurements made within the test section are made with respect to the laboratory frame of reference. The origin of the coordinate system is at the center of the splitter plate tip and is shown in Figure 6. The *x*-axis goes with the overall flow direction, with the *y*-axis as transverse to the mixing layer and the *z*-axis spanwise to the flow. The test section itself has a range of 762 mm in the *x*-direction, from +50.8 mm to -76.2 mm in the *y*-direction and is 63.5 mm wide in the *z*-direction on either side (providing 127 mm in total width). Each side-view window is able to view the flow entirely in the *y*-direction and has a range of 254 mm streamwise, with the windows moveable—allowing for full optical access along the test section for side-views. The top and bottom walls of the tunnel, when configured for optical measurements, have a 25.4 mm-wide window at the spanwise center to provide optical access for the laser sheet along the entire test section length.

For measurements made with the moveable probe, the bottom wall of the tunnel with the window is replaced with an alternative bottom wall. This bottom wall has a narrow slot running streamwise along the center measuring 3.175 mm in width. Moveable blanking plates allow the probe to be placed at multiple streamwise positions, at x = 34.7, 85.5, 186.6, 287.7, and 338.5 mm. Probe traces (in the *y*-direction) can be made at all of these positions, allowing for measurements to be made along nearly the full length of the test section. More to the point, measurement traces

are possible near to the splitter plate, in the developing mixing layer, and in the fully developed region, allowing for verification of the non-intrusive results throughout.

2.1.1 Facility Modifications

Major modifications, however, were required in order to perform the experiment of interest, with a heated incoming secondary flow. The facility was not originally designed with such a thermal requirement in mind; therefore, it did not support heating the incoming air to the stagnation temperature required of the current experiments. In order to support these needs, a preexisting heater used in former heated work was taken out of long-term storage and rehabilitated. The heater, a HEAT model CHP-0824S-60-74Y-483, can be seen in Figure 7; its specifications are listed in Appendix A. Piping to and from the heater in order to mate it with the preexisting facility also required a great deal of early design work in order to guarantee safe operation of the modified wind tunnel.

Figure 7. Electric air heater in GDL

Installation of the heater was without major issue; it was taken out of storage and placed in the Gas Dynamics Lab in short order. Final adjustments to its location and orientation were made shortly thereafter in order to align it with the wind tunnel inlet. Once the power supply had been replaced by new cabling able to be safely routed to the lab's 480VAC circuit breaker, electrical checkouts were performed and the heater was turned on for the first time. The internal PID control

system tuning was then examined to verify that its settings were as documented—that is, at the factory-set points. The heater's internal thermoprobes were removed and checked for measurement accuracy, as well as the sealing of their mountings. No issues were found, nor deviations with the prior documentation; the heater has since been operated without event or issue, to the relief of all involved.

In tandem with the addition of the heater itself was the supporting piping running to and from the heater, supplying the heated air to the wind tunnel. All design work was performed in PTC Creo Parametric 3.0, with an emphasis on using a minimum (if any) of custom parts and not requiring the work of an external party in order to reduce costs. Standard parts were sourced from McMaster-Carr, and a bill of materials (seen in Appendix B) was created. All new parts that were under pressure or thermal load were threaded; in doing so, the second goal was attained. The CAD rendering is shown alongside a photo of the actual implementation in Figure 8 and Figure 9 on the next page. The most notable part of the new plumbing was the decision to utilize a steel-reinforced flexible hose for the incoming air to the heater, coming off the facility air supply. This allowed for the only system constraint to be mating the exit of the heater with the wind tunnel inlet; as this was the heated air flow, it was of course the priority during design. Along this heated air flow, a tee was placed before the bend in the piping, intended to allow for seeding of the flow during the PIV measurements. More discussion on the seeding may be found in Sections 2.3.5, 4.1.1, and 4.1.2.

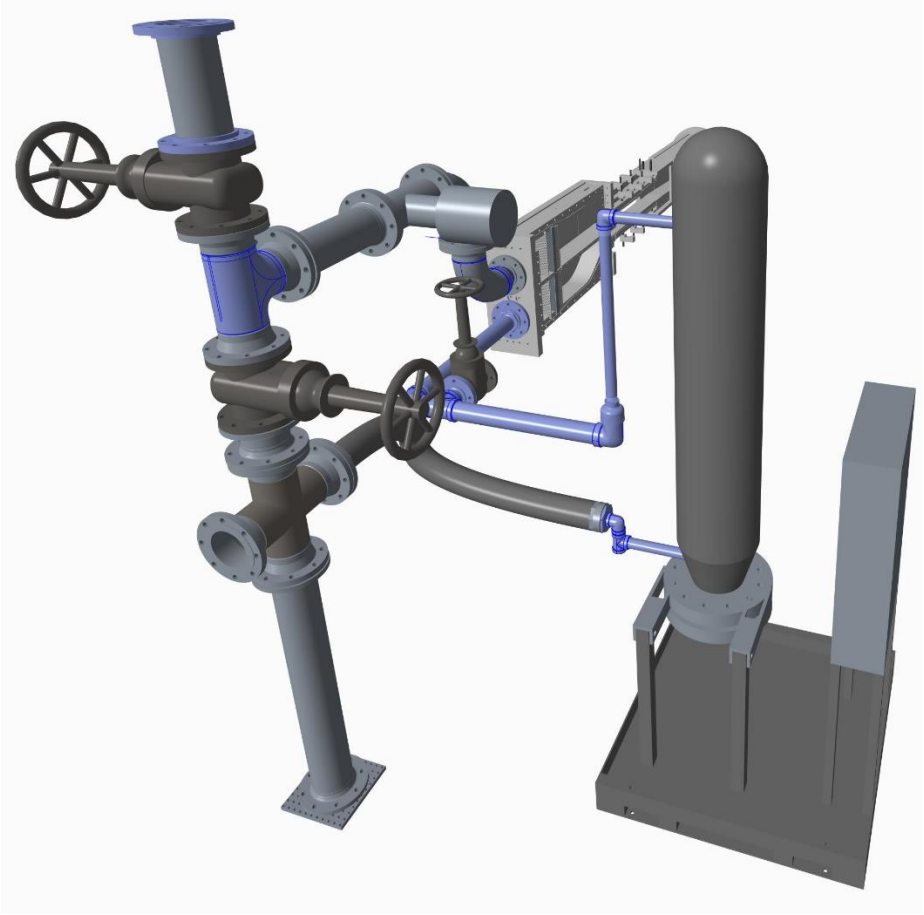

Figure 8. CAD rendering of wind tunnel with heater addition

Figure 9. Facility with installed heater in Gas Dynamics Lab

2.1.2 Modification Analyses

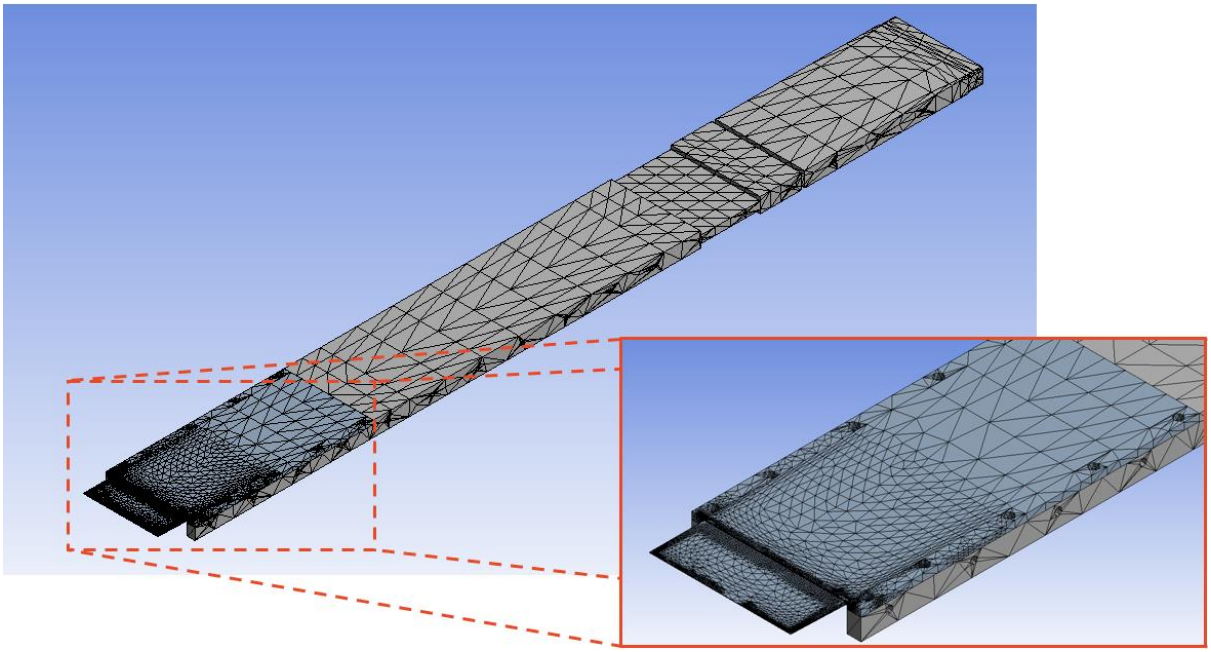

Figure 10. FEA mesh of splitter plate with tip feature

The goal of this work was to compare the behavior of the splitter plate during simulation and in actual operation, with the intention to glean insight into whether fatigue (especially cracking) near the root and/or tip may occur over time. Comparisons to the work done by Lee[34] in his static-state analysis of the original tunnel operation were also made, although they are not presented here for brevity. The only major differentiation between the two static analyses was the increased quality of the mesh capable via ANSYS, reducing the von Mises stress value at the splitter plate root corners by an order of magnitude.

Table 1. Typical Transient Simulation Operating Conditions

	P1 [kPa]	P2 [kPa]	T01 [K]	T02 [K]	M1	M2	h_1 [W/m^{2}K]	h_2 [W/m^{2}K]
Warm-up	98.4	98.5	288	400	0.076	0.065	3400	2900
Full Flow	53.046	60.515	285	495	2.06	0.328	74200	6300

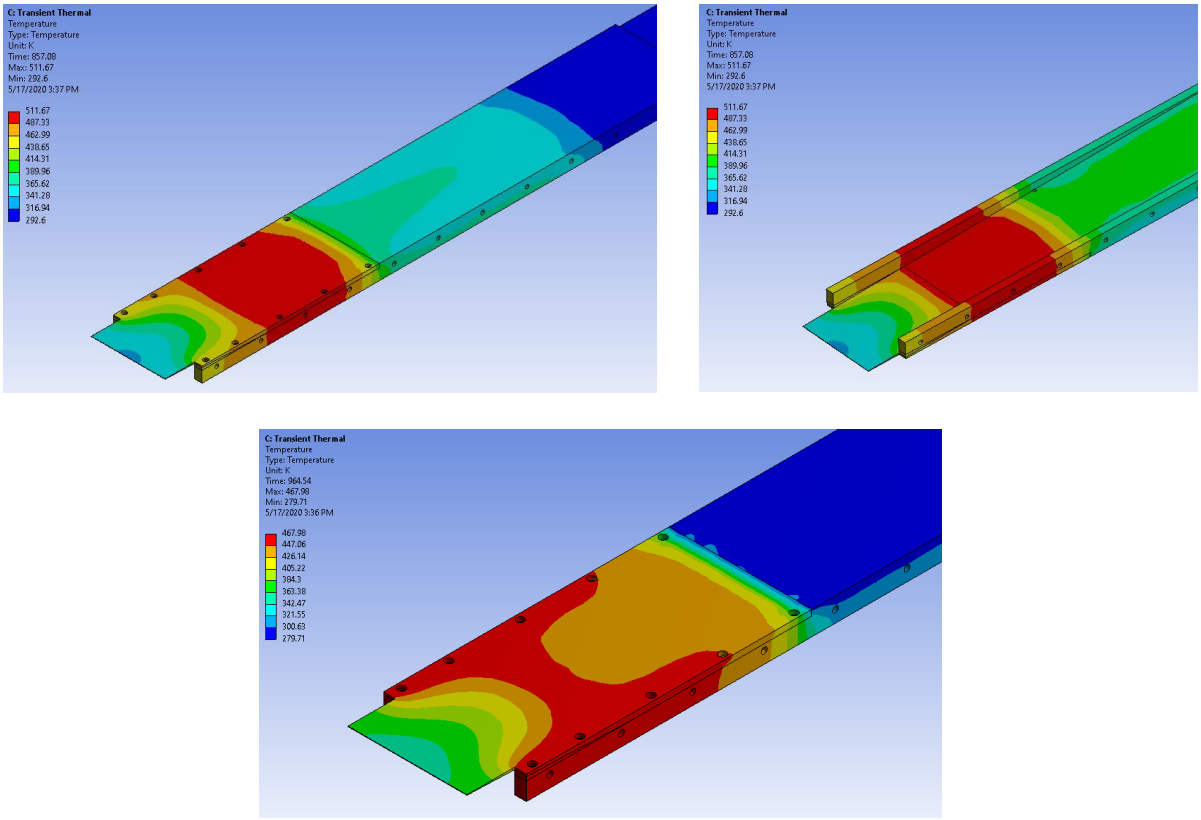

Figure 11. Temperature distribution on splitter plate at end of warmup (top L and R) and end of run (bottom)

For the FEM analysis itself, early facility run conditions, taken from the data recorded in LabVIEW, were provided as inputs to the transient thermal and then the transient structural simulation blocks in ANSYS. These conditions of interest gave both static and stagnation temperatures and pressures for both streams, which were then used to calculate all required inputs including the enthalpies of the respective streams. Both operating conditions are summarized in Table 1 above. The temperature distribution at the top and bottom of the splitter plate at its peak during operation is all shown in Figure 11. This calculated temperature distribution then was applied as an additional load to the transient structural analysis. This notably produced a deformation that changed in direction from the "warm-up" phase of the run where the secondary stream heats to its desired stagnation temperature, to the "full-flow" phase, where the experiment of interest takes place. While the deformation appeared to be reasonable, the stress calculation

seemed to be off by at least an order of magnitude; it was predicted by ANSYS to be on the order of 3 GPa.

Mesh refinement along the splitter plate titanium insert, especially along the sides and filleted edge were the main point of further improvement to the analysis. Figure 10 highlights the density of the mesh, especially at and around the splitter plate's stress concentrations. Using these improvements, as well as minor adjustments to the application of the operating conditions, new transient simulations were run on the system; Figure 12 shows these results. It is evident from the stress contours that the refinements and minor improvements in the applied boundary conditions (BCs) alleviated the issues in overpredicting the stress concentration at the corners of the splitter root. The newly computed safety factor, at minimal points 1.05 and largely above 3, was acceptable for the wind tunnel's operation, especially as the current thermal experiment is now concluded.

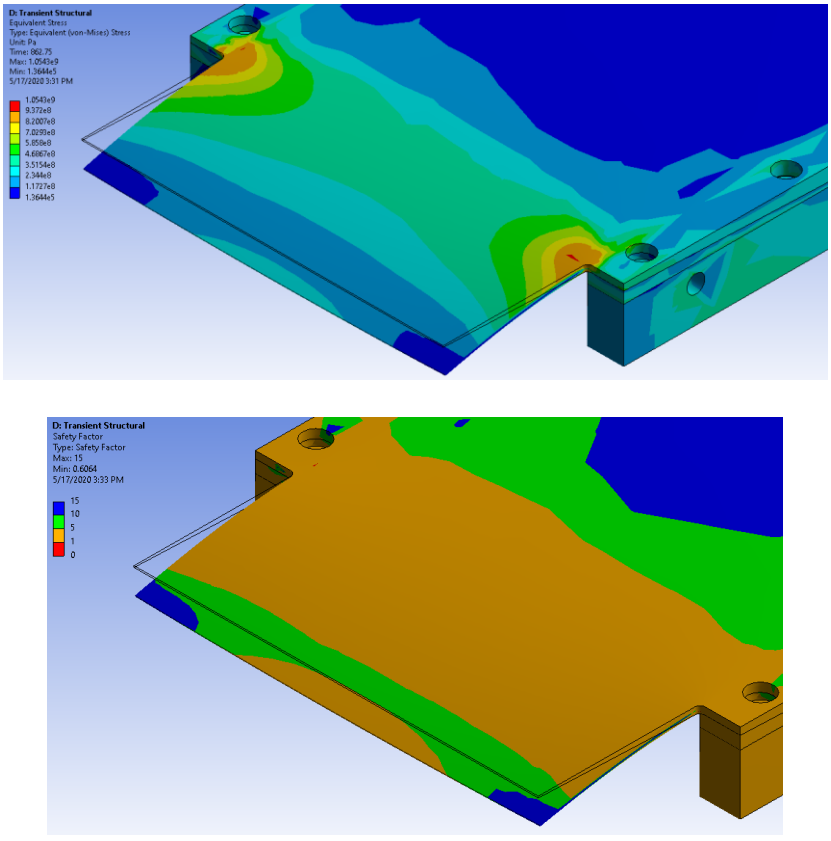

Figure 12. Maximum von Mises stress (top) and safety factor (bottom) on deformed model

2.2 Experimental Operation

Operation of the tunnel itself is performed manually to maintain the necessary operating condition. This operating condition is defined by matched static pressures at the splitter plate tip. Pressure taps are located near to the splitter plate tip in both streams, after the nozzle; however, physical constraints dictated that these taps are approximately 4” upstream of the splitter tip. As such, an alternative method of pressure matching based on a differential pressure between the two pressure taps is utilized. This operating condition is determined through the use of schlieren visualizations to view the behavior of the shear layer and subsequent sidewall pressure tap measurements to verify the differential pressure.

2.2.1 Experimental Operating Procedure

Manual operation of the tunnel is primarily performed by controlling a gate valve that is positioned before the piping split into the primary and secondary streams. Normal operation of the tunnel may be thought of in three phases: warm-up, primary operation, and cool-down. Warm-up and cool-down are lengthy, necessary portions due to the slow heating time of the heating coil and latent thermal mass of the facility, respectively. Initial preparation of the tunnel requires purging of the tunnel (discussed briefly in Section 4.1.1) and manual cleaning of oil buildup (from PIV seed particles) in the tunnel. The tunnel walls are scrubbed to remove as much of the accumulated oil as possible, particularly in the nozzle sections. The windows are then cleaned, especially the bottom windows, which occasionally accrue oil tracks across them, preventing the laser sheet from properly illuminating the test section. Once the windows have been fully secured back onto the tunnel, the pressure transducers are zeroed to ambient pressure prior to the warm-up phase.

The warm-up phase typically takes on the order of fifteen minutes to complete. To begin, the primary pneumatic valve is cracked open a small amount. The main gate valve is then opened

to a position allowing a “trickle flow”, about M = 0.065, to run in the secondary stream. This was found over time to be the most effective approach for heating up the combined thermal mass of the heater, tunnel, and flow most quickly. During the warm-up phase, the data acquisition systems are checked out, especially when camera systems are in use. Previous lab experience has shown that some camera systems, especially PCO cameras, suffer from data transfer issues and even crashes while recording data. It has been found that recording checks just prior to actually taking data are the most consistent way to prevent any configuration issues. No matter the method being used for data collection, by using the low flow conditions of the warm-up phase as a “dry run” to verify that the acquisition method is in order and all components are working in sync has prevented “dead runs” where no data are able to be acquired.

Once the secondary stagnation temperature has reached the desired point, about 495 K, the primary operation phase may begin. A check is made to verify that no oil or condensate has accumulated on the windows during warm-up as can be seen in Figure 13; in the case that there is oil on the windows, the heater and flow are temporarily stopped, and the windows removed carefully to be cleaned. It should be noted that prior to running the tunnel at the intended run conditions, the walls and windows only warm up a small, tolerable amount to the touch. Once the windows are verified to be clean, the primary pneumatic valve is opened to its full open position and the primary seeder (if in use) is started early to allow it to come up to full pressure prior to full-flow. After a set time elapses after the primary seeder is turned on,

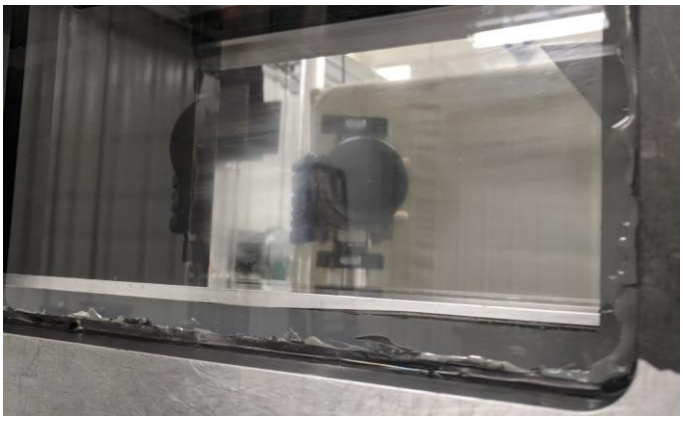

Figure 13. Minor oil accumulation on window from warm-up

the manual gate valve is opened until the desired operating conditions are reached. The gate valve position must be manually varied throughout the duration of the run to maintain the operating conditions while the data acquisition takes place. At the end of the data acquisition, the primary seeder is turned off, and the tunnel is continued to run at full until the gate valve to the secondary seeder (see Section 4.1.1 for more detail on the seeding configuration) is closed.

For cool-down, the heater is turned off, the pneumatic valve is closed to once again only allow a small amount of flow through, and the main gate valve closed back to the "trickle flow" point. This is maintained while the heater and tunnel cool down to safer temperatures, a process that typically takes about twenty to thirty minutes. Typically, near the end of the cool-down process, a purge run is made, further cooling the wind tunnel. During the lengthy cool-down period, all data are saved and backed up, and data acquisition equipment is turned off. At the end of the cool-down period, the tunnel is still warm, typically between 315-320 K; all flow is shut off through the tunnel and it is left to cool down naturally until it returns to near-ambient temperatures. In total, the entire process of running the tunnel to acquire data requires about 40 minutes, and the cool-down period afterward takes about three hours depending on how many purge runs take place. As a result of these limitations, runs of the facility were intermittent, and a premium was placed on acquiring as much high-quality data as possible in each run. It was paramount that for maximum efficiency in taking this large amount of data that as few "dead runs" without data as possible would occur, especially when considering the large time investment that each run requires. Of additional consideration was the stress loading from both the thermal condition as well as the action of running the tunnel itself; as Section 2.1.2 and Lee[34] discuss, the possible fatigue of the splitter plate was a constant consideration during tunnel operation. Minimization of the number of runs would therefore behoove both the safety and expediency of the experiment.

2.2.2 Experimental Operating Condition

Schlieren still images and high-speed video provide a real-time, qualitative analysis of the mixing layer while determining the proper operating conditions. In doing so, the operating condition is found where (1) there is a weakly switching compression / expansion wave in the primary stream off the splitter tip along with (2) a straight mixing layer, not bending into either stream. These operating conditions are then utilized as sidewall pressure tap measurements are obtained, verifying that in the fully developed region, static pressures become stable and constant, and no vortices or other dynamic processes are present. Table 2 below shows the nominal operating conditions for this experiment.

Table 2. Experiment Operating Conditions

P_1 (kPa)	P_2 (kPa)	P_{01} (kPa)	P_{02} (kPa)	T_1 (K)	T_2 (K)	T_{01} (K)	T_{02} (K)	U_1 ($^m/_s$)	U_2 ($^m/_s$)	M_1	M_2
58.58 ± 0.11	61.97 ± 0.11	443.89 ± 2.83	64.573 ± 0.67	177.98 ± 3.06	467.80 ± 12.5	297.01 ± 0.08	473.71 ± 0.31	488.87 ± 8.40	108.95 ± 2.92	1.83 ± 0.05	0.251 ± 0.01

s ρ_2 / ρ_1	**θ** T_{02} / T_{01}	**r** U_2 / U_1	**M_c**
0.402 ± 0.01	**1.59 ± 0.01**	**0.2229 ± 0.007**	**0.541 ± 0.02**

It must be noted that while the tunnel is running, however, the operating conditions are more of a targeted optimum rather than a true steady-state value. The most varying condition is the temperature; unfortunately, it is not feasible for the heater to perfectly maintain a constant temperature at the flowrates required. Therefore, the secondary stagnation temperature is brought above the desired point and allowed to fall below as data are obtained. Both the schlieren and sidewall pressure analysis showed no major difference in flow structures as long as the temperature stayed reasonably close to its target point of 495 K. The maximum range was between 515 and 455 K, with more typical range between 505 and 470 K. Furthermore, as outside weather conditions changed, the incoming air temperature would respond in kind, leading to a variance in

stagnation temperature throughout the experiments in the *primary* stream as well. However, this variance in stagnation temperatures is largely negligible to the data obtained, which was taken at seasonally similar times (winter-spring for velocity data, summer-fall for temperature data).

2.3 Flow Diagnostic Techniques

A multitude of flow diagnostic techniques were utilized over the course of the project, including both intrusive and non-intrusive methods. Classical methods of observation (in order of measurement taken) were: Z-type schlieren imaging and video recording, sidewall static pressure tap measurements, and thermocouple probe measurements. Constant-voltage hot wire anemometry was attempted, but ultimately proved too costly in time and expense to complete. Modern methods of observation were stereo and planar particle image velocimetry (PIV) and filtered Rayleigh scattering (FRS).

2.3.1 Schlieren Measurements

Table 3. Schlieren Equipment Summary

Component	Description	Parameters Used
Photron SA-5 Camera	CMOS camera with max resolution of 1024x1024 pixels and max framerate of 1,000,000 fps	Full-resolution: 7000 fps High-speed: 120,000 fps at 900x320 resolution
Nikon AF Nikkor telephoto zoom lens	70-210 mm focal length with f/4.0~5.6 maximum aperture	Zoomed to fill image upon camera sensor
2 Parabolic Mirrors	12-inch diameter 96-inch focal length	Placed to fully collimate incoming light beam
LED (Thorlabs MWWHLP1)	LED light source: warm white color (3000 K, 400-700 nm range)	Full brightness 700 mA current applied
Knife-edge	Blade tip blocks bent rays of light	Placed at focal point, horizontally mounted

Schlieren visualizations were the first obtained in this configuration: this method was initially used to simultaneously determine the operating condition for the case while also monitoring the safety of initial test runs. A classical Z-type setup was utilized, with mirrors large enough to illuminate the entire test section during measurement. Table 3 above shows the

equipment used for the schlieren images and videos, while Figure 14 shows the conceptual setup schematic. The schlieren technique is line-of-sight averaged, where a collimated beam of light passes through the test section. These collimated rays are bent slightly due to density changes within the test section (notably, due to shocks and expansions). At the knife-edge, light rays bent towards the knife-edge are cut off while those bent away are passed through, allowing for the density gradients to become visible. Physical flow features, especially in a mixing layer, therefore become much more apparent as a result.

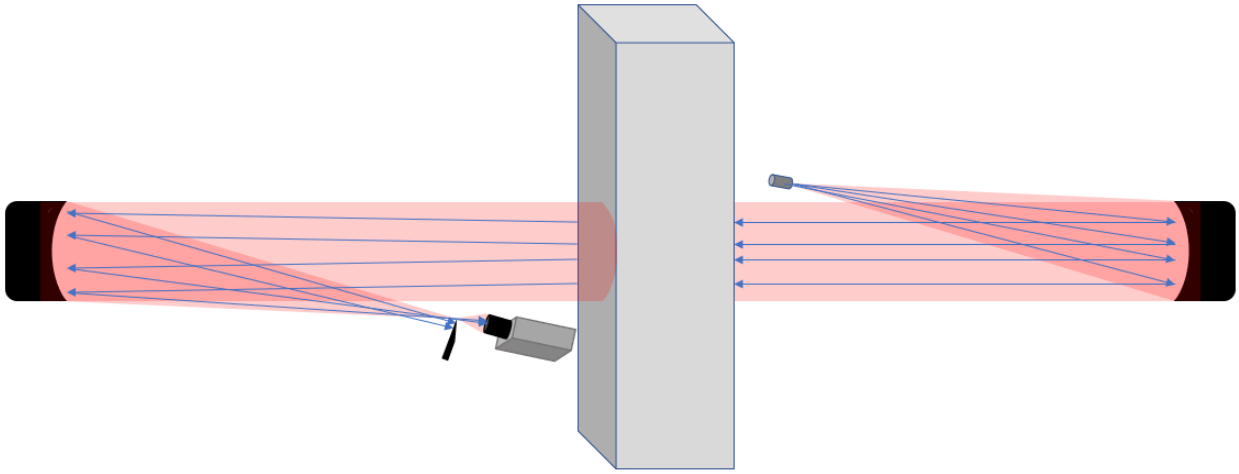

Figure 14. Z-Type schlieren schematic

After initial setup and determination of the run conditions, full-field high-speed videos were obtained using the Photron camera capturing at a framerate of 120,000 frames/second. It should be noted, however, that the higher framerate comes at a cost of resolution as the SA-5 camera is only capable of 900x320 pixel resolution at this recording speed. These high-speed images allowed for an early qualitative analysis of the entire flowfield, from splitter tip to its fully-developed region. Furthermore, at such a high framerate, features that were not possible to be noticed at lower framerates (and would have been smeared out) are visible during playback. A selection of frames from the high-speed video may be seen later, in Section 3.1.1.

Full-resolution (1024x1024 pixel) images were also obtained at the maximum framerate possible, 7000 frames/sec, for instantaneous schlieren images of the whole flowfield. From the full-resolution images, the shock structure comes into full relief, showing the multitude of smaller shocks that result from minor imperfections in the primary stream nozzle. Discussion of the schlieren results, both high-speed movies and full-resolution images, is undertaken in Section 3.1.

2.3.2 Sidewall Static Pressure Measurements

Further verification of the tunnel operating condition was performed by interchanging the typical tunnel sidewall, with its windows for optical access, with an alternate sidewall replete with pressure taps. Three rows of taps are installed on this sidewall, which can be seen schematically in Figure 15. Taps are placed in the middle of the primary and secondary freestreams, at *y*-locations of +25.4 and -38.1 mm, respectively, and along the centerline at y = 0 mm. The taps are spaced out along the x-axis; each line has a tap at x = 3.175 and 739.775 mm, with the secondary and primary lines having a tap every 101.6 mm in between, and the centerline every 25.4 mm in between. Pressures were monitored using a custom LabVIEW program capable of capturing all the pressure tap data, as well as the facility temperatures and pressures necessary for operation.

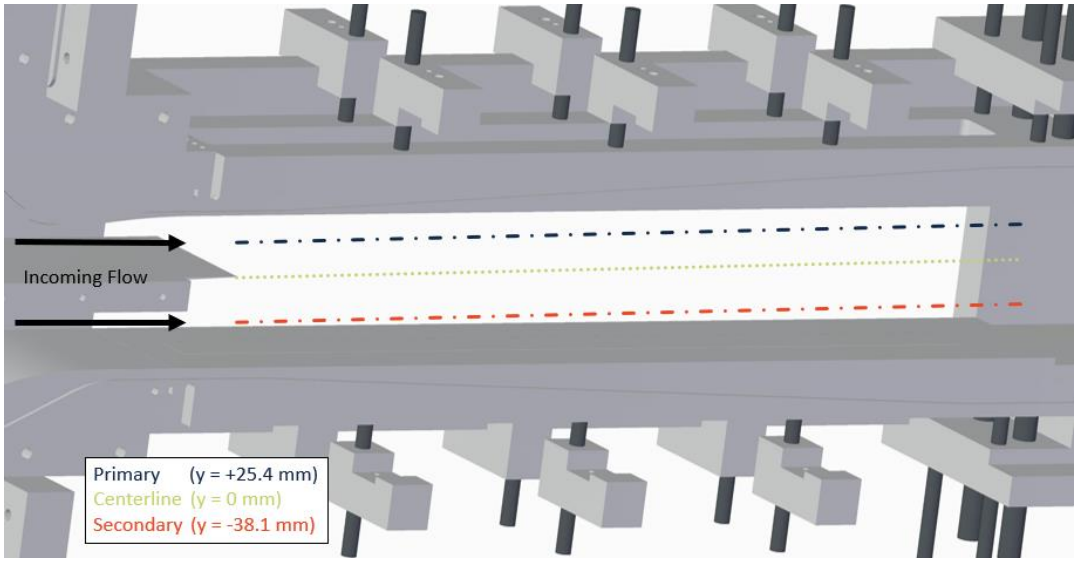

Figure 15. Schematic of static tap layout

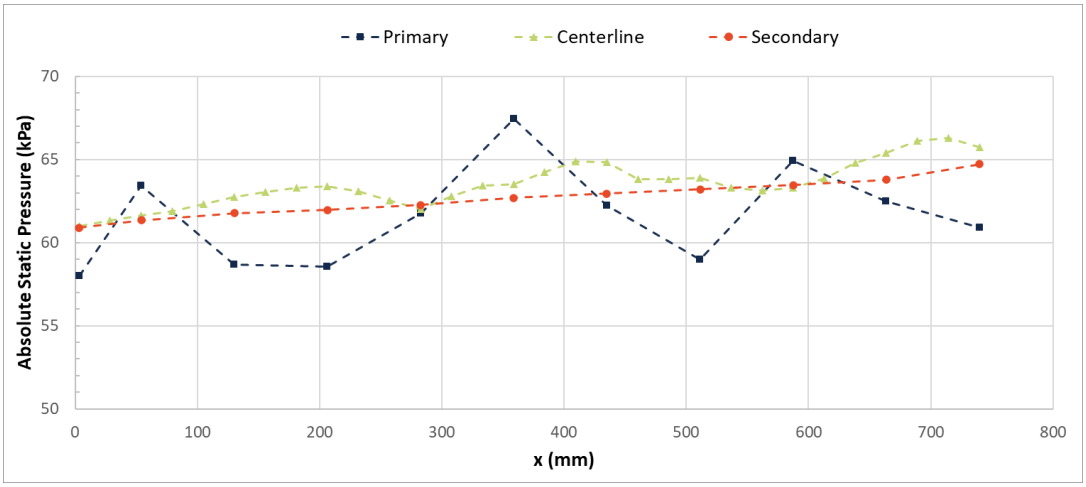

Figure 16. Static pressure tap results at tunnel operating condition

The primary aim of the static pressure tap measurements is to verify the assumed operating condition found with the schlieren measurements. This is done by checking that the operating condition is achieved by having no strong adverse or favorable pressure gradients along the length of the mixing layer. Looking at the typical results in Figure 16 above, a slight adverse pressure gradient is noted along the length of the test section, but it is less than 5 kPa over the course of the 750 mm-long mixing layer. Larger fluctuations are noted in the primary stream and are due to the inevitable weak compression/expansion waves present there; these are discussed in detail in the schlieren analysis (Section 3.1) and the stereo-PIV analysis (Chapter 4). In all, these are minor effects that demonstrate that the desired operating condition is achieved, confirming that it is usable for the later analyses and not requiring further tuning.

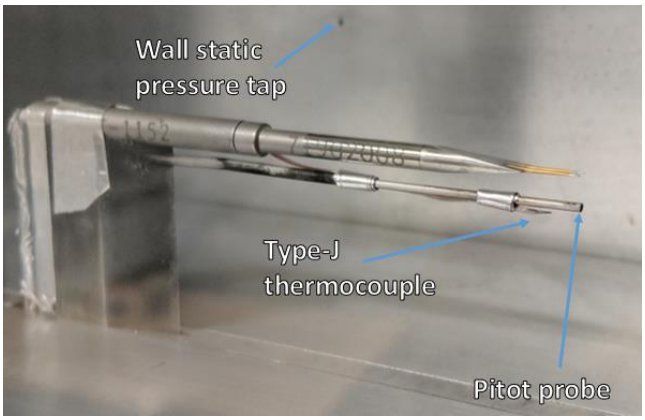

Figure 17. Pitot probe in tunnel with Type-J thermocouple mounted. Static pressure tap wall installed in background

2.3.3 Temperature Probe Measurements

Early temperature measurements were performed using a pitot probe in the wind tunnel with a thermocouple affixed to the probe, as can be seen in Figure 17. This probe,

based on the same design as a set on loan from NASA Glenn Research Center, only measures the total pressure—there is not a static pressure ring or tap on the probe. It is operated as part of a linear traverse system able to take traces through the *y*-direction at specific points along the *x*-axis: at 34.7, 85.5, 186.6, 287.7, and 338.5 mm from the splitter tip. This system is actuated by a Zaber stage, and is controlled by a combined LabVIEW VI capable of controlling the probe traverses in addition to the typical task of operating and monitoring the wind tunnel; the traverse system is shown in Figure 18. The Zaber stage, chosen for its high resolution, had a positional uncertainty of less than 100 μm. The probe traverses are best operated by a second user that defines the probe trace requirements (*y*-limits and step size), and then both begins the traverse once the operating condition is achieved as well as monitors the probe during the traverse itself.

Figure 18. Zaber stage traverse system

2.3.3.1 Initial Thermocouple Measurements

Initial temperature traverses were primarily intended to provide an early study of the temperatures in the mixing layer. The field measurements provided by the filtered Rayleigh Scattering (discussed later in Section 2.3.6) were scheduled to be performed late in the project. The traverses also had the secondary role of verifying the accuracy of the FRS measurements, albeit with some increased uncertainty as a result of the probe intruding into the flow.

Initially, attempts were made to measure the total temperature of the flow by simply adhering a bare-wire thermocouple to the pitot probe. However, the increased temperature in the secondary stream caused a multitude of issues. The adhesive on the aluminum mounting tape failed; alternative mounting tapes were explored that utilized a silicone-based adhesive instead.

Double-sided tape intended for electrical mounting was attempted, but the adhesive was not strong enough to hold up to the combination of the secondary's thermal condition and the drag forces in the supersonic primary stream. Eventually, a solution using high-temperature heat-shrink plastic was utilized; this had the disadvantage, however, of requiring a heat source imposed on the thermocouple itself during installation on the probe. Burn-through of several thermocouples occurred as a result, primarily due to the high temperature required to shrink the wrap and the tight confines of the test section (the thermocouple had to be mounted *in-situ*). Further issues came during operation, as the heat-shrink would intermittently move or bunch up on the probe, leading to the thermocouple moving in the flow and sometimes even breaking off as can be seen in Figure 19. While these issues were able to be largely overcome, the overall lack of trust in the data necessitated a second stagnation temperature method.

Figure 19. Broken thermocouple on pitot probe

2.3.3.2 TAT Probe Measurements

Figure 20. TAT probe mounted in tunnel

To alleviate the issues with using the bare-wire thermocouple above, as well as to remove the worry of inaccuracy with the measurements, a total air temperature probe was sourced from United Sensor Corp. This probe, a TD-10-J-36-C-1-F, a 1/8" diameter, 10" long probe with a type-J thermocouple, is typically used in flows with a temperature below 550 K and a velocity below 615 m/s. As such, the probe design selected was optimal for the expected test conditions. The probe can be seen in Figure

20, mounted in its adapter such that it can be used with the same traverse hardware as the other probes. Appendix C has an engineering drawing of the TAT probe, furnished by the manufacturer.

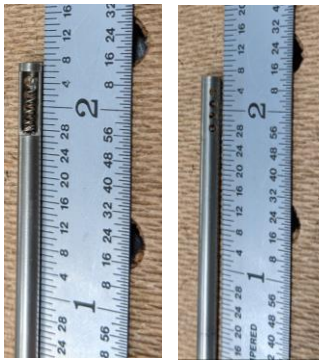

Figure 21. TAT probe front and back showing holes for airflow (with inch ruler for reference)

The total air temperature probe is designed to allow pass-through of flows through cut-outs on the back of its housing seen in Figure 21. In doing so, it has a greatly decreased response time between temperature readings. This response time was found to be less than 4 seconds for a flow with a stagnation temperature rise of 200 K at near-zero velocity; when in the tunnel at its operating condition, this response time was even shorter—typically on the order of a second to overcome the maximum thermal difference. Such performance allowed for quick traverses through the thermal mixing layer at high recording rates.

All temperature profiles took a minimum of 30 samples per measurement point, with multiple temperature profiles at each *x*-location, no less than four and typically six. These temperature profiles had a typical measurement uncertainty of 0.1 K in the freestreams and 0.25 K in the mixing layer, based on the Student t-distribution using a 95% confidence interval.

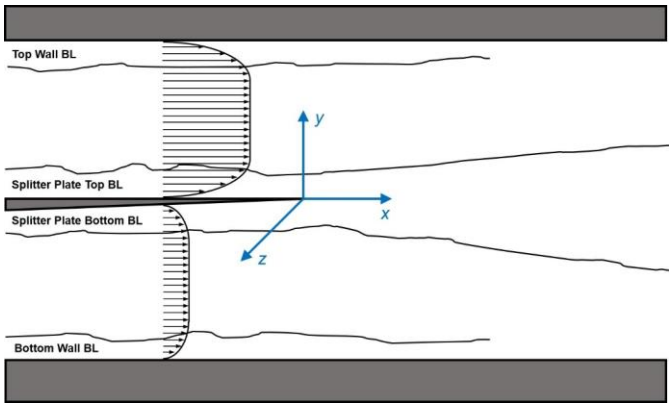

Figure 22. Incoming boundary layers

2.3.4 Boundary Layer PIV

As the primary purpose of this study is to provide benchmark-level measurements for CFD validation, especially with respect to turbulence in compressible mixing layers, the incoming boundary layers were

measured to provide a holistic definition of the incoming flow boundary conditions. Figure 22 shows the four boundary layers of interest, along the wind tunnel top wall, both the top and bottom walls of the splitter plate, and the bottom wall of the wind tunnel. Three of the boundary layers, the bottom wind tunnel wall and splitter plate top and bottom walls, were studied herein. It was assumed that the characteristics of the top wall boundary layer were the same as for the $M_c = 0.690$ case of Kim[13,14], as the heating of the secondary stream would presumably not affect the incoming primary freestream nor the top wall itself to any measurable degree.

Table 4. Boundary Layer PIV Configuration

Component	Description	Parameters Used
PCO 2000 Camera	CCD camera, 2048x2048 resolution	Double-frame mode
Nikon Micro-Nikkor Camera Lenses	60 mm focal length f/2.8D min aperture	Empirically focused with aperture set to f/2.8D
LaVision DaVis 8.4	Computer program for and computation of PIV vectors	See Table 7 for computation settings
LaVision Type 058-5 Calibration Plate	Double-sided, dual-level marker plate	--
Quantum Composers 9518 Pulse Generator	Delay and pulse generator to sync cameras and laser	Laser $\Delta t = 1$ μs
New Wave Gemini Laser	Double-Pulsed Nd:YAG laser Frequency doubled to 532 nm	Laser power empirically tuned based on timing
Laser Sheet Optics	Plano-concave cylindrical lens (f = -50 mm), plano-convex spherical lens (f = 1000 mm), dichroic turning mirrors (coated for 532 nm)	Empirically located for desired sheet thickness (>1 mm) and streamwise length (30-40 mm)

Boundary-layer PIV was performed to characterize these boundary layers in a planar configuration using the settings as listed above in Table 4. Data were obtained into the freestream and as close to the wall as possible: velocity vectors in the *x-y* planes were recorded, along with normal and shear Reynolds stresses in this plane. These measurements proved, as has been typical for this lab in other experiments, to be difficult to obtain due to the large amount of laser light reflections near the surface. These reflections were exacerbated by the slight (but at this scale non

negligible) movement of the splitter tip during tunnel operation. These challenges were eventually overcome by careful adjustment of the laser sheet's incoming angle as well as by cutting off the laser sheet edges by an aperture, to minimize laser light impinging on the splitter plate.

2.3.5 Stereo-PIV

Table 5. Overview of SPIV Components

Component	Description	Parameters Used
2x LaVision Imager sCMOS Cameras	CMOS camera with 2560x2160 pixel resolution	Double-frame mode
Nikon Micro-Nikkor Camera Lenses	60 mm focal length f/2.8D max aperture	Empirically focused with aperture set to f/2.8D
2x LaVision Scheimpflug Adapters	Adjusts lateral focal range of cameras by tilting lens away from image sensor	Empirically tilted, between 30-45°
LaVision DaVis 8.4	Computer program for both capture of particle images and computation of SPIV vectors	See Table 7 for computation settings
LaVision Type 11 Calibration Plate	Double-sided, dual level marker plate	--
LaVision PTU	Timing pulse generator to sync cameras and laser from computer settings	Laser Δt = 1 μs Camera delay = -0.3μs
New Wave Gemini Laser	Double-pulsed Nd:YAG laser Frequency doubled to 532 nm	Laser power empirically tuned based on timing
Laser Sheet Optics	Plano-concave cylindrical lens (f = -50 mm), plano-convex spherical lens (f = 1000 mm), dichroic turning mirrors (coated for 532 nm)	Empirically located for desired sheet thickness (1-2 mm) and streamwise length (70-80 mm)

The data obtained via stereo-PIV are one of the two primary advances of this work. SPIV data were obtained along the spanwise center of the test section, in the streamwise direction, until the flow is fully turbulently developed. At a minimum, data were obtained from y-values between ±20 mm, well into the freestream on both sides of the mixing layer. The maximum spacing between points was 0.263 mm, with over 100,000 points per measurement field of view. Each point in the data field had a three-component velocity vector calculated for over 3000 instantaneous images,

which allowed for a multitude of statistical measurements to be performed upon the dataset. Table 5 lists the hardware used for the stereo-PIV; Figure 23 and Figure 24, showing the notional setup and a photo of the physical setup, respectively, are presented below.

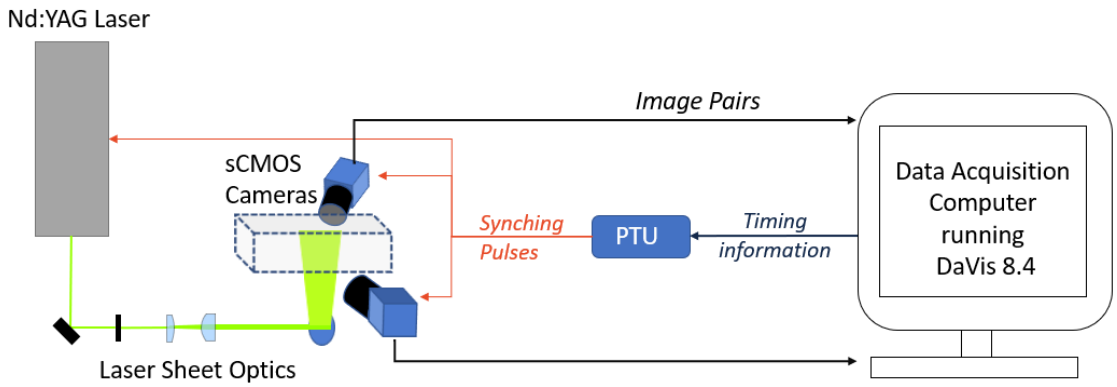

Figure 23. SPIV notional equipment schematic

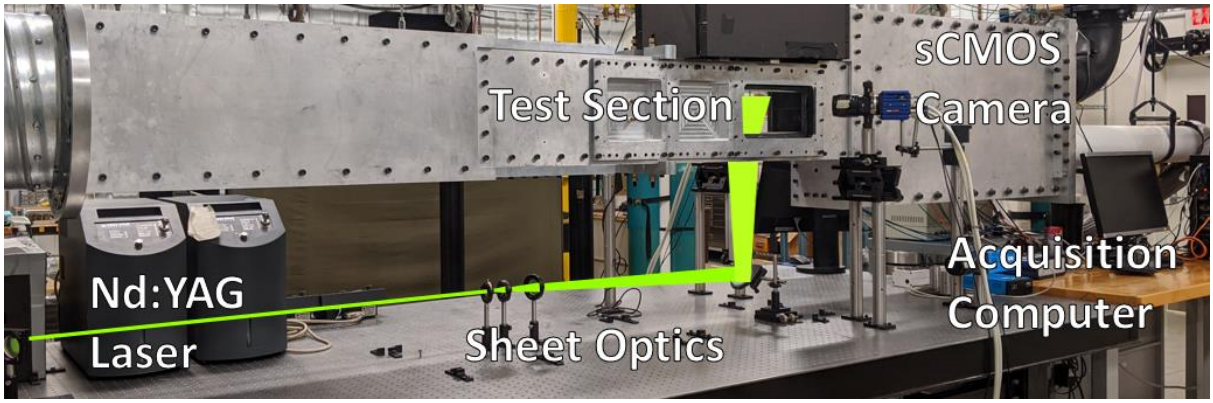

Figure 24. Photo of wind tunnel & SPIV physical lab setup

As with any PIV study, determining the optimal seeding density was paramount in recording the most accurate data possible. Numerous runs were made, starting with seeding settings used in previous work performed in the same lab group with similar flow conditions. From there, seed pressure was adjusted over time empirically until a window of operating conditions was established. With respect to the secondary flow, this was adjusted numerous times as its method of seeding changed until a viable final method was determined (discussed in much greater detail in the following section). Given time, the seeding settings for both the ViCount and the

Laskin nozzle were determined, and are listed in Table 6 below. Further discussion of the seeding is given in Section 4.1.2.

Table 6. Summary of Seeding Settings

Seeder	Seeding Oil	Flow Seeded	Seeding Method	Input Pressure	Seed Size
ViCount 1300	White Mineral Oil	Primary	Combustion-Condensation	68 psig	0.2-0.3 micron
TSI Model 9307	Avocado Oil	Secondary	Droplet Bursting	15 psig	0.5-1.0 micron

The entire SPIV process, from data acquisition to processing, was performed using the DaVis 8.4 software package developed by LaVision. DaVis controls the data acquisition phase through a physical timing unit (PTU) that interprets the desired execution of the physical system as prescribed in the software. This PTU connects to the laser system as well as the cameras; it modulates the power of the lasers by varying the Q-switch time delay of each pulse. On the data acquisition side, the cameras are connected via a proprietary bus to the computer, allowing data transfer during live capture. Furthermore, this capability means that not only is the camera's RAM supplemented by the RAM of the acquisition computer, but also that data may be saved to the hard drive during recording. Through the combination of these advantages, a larger ensemble of images may be captured during each run compared to previous work without binning or other methods of cutting down on image size. When this is considered in tandem with the much higher downtime required for the heating and cooling of the facility (see Section 2.2.1), it becomes clear that the capabilities made possible by the LaVision software and cameras were central to the success of this study.

A camera-dependent calibration is applied to each frame captured, based upon the use of a double-sided, dual-height calibration marker plate seen in Figure 25. Using the calibration plate, the DaVis software is able to make a mapping for each camera in three dimensions; this mapping drives the calibration that converts the raw images into the lab reference frame. A further calibration is necessary for stereo PIV, where the initially calibrated images are used to create a second disparity map and calibration in the software's self-calibration procedure. A further discussion of the stereo-self calibration is found in Section 4.1.3.

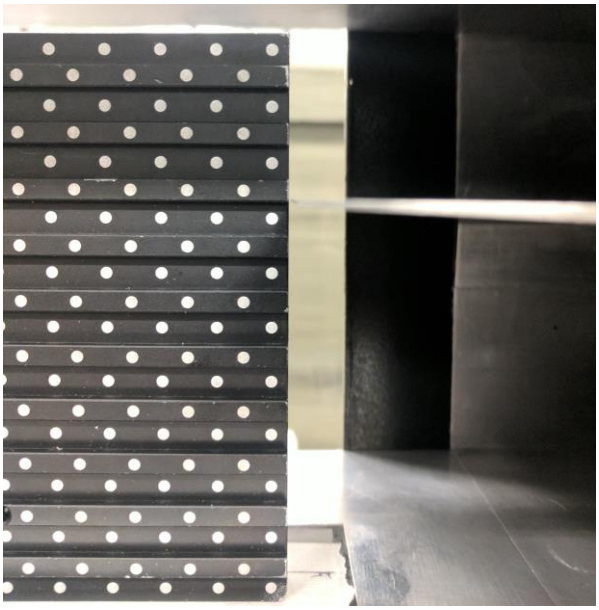

Figure 25. Type 11 calibration plate in wind tunnel

Table 7. SPIV Processing Parameters

Operation	Description	Parameters Used
Add default attribute	Apply calibration and physical recording parameters	See Table 5
Subtract Sliding Average (Gaussian Profile)	Apply Gaussian intensity distribution to illuminated particles to reduce noise and oil blur	Filter length: 9-11 pixels
Subtract Constant	Reduce noise floor	60 counts
Min-Max filter for Intensity Normalization	Local normalization to increase SNR of particles	5-7 pixels
PIV particle image processing	Calculate *u*, *v*, & *w* velocity components along with uncertainty for each image pair	Multi-pass Stereo cross-correlation: 64x64 with 50% overlap @ 2 passes 32x32 with 75% overlap @ 4 passes Adaptive PIV weighting function High Accuracy mode for final pass

Table 7 (cont.). SPIV Processing Parameters

Operation	Description	Parameters Used
Vector Postprocessing	Reduce errant vectors calculated from PIV step based on expected velocity range and Q peak ratio	*U*: 305 ±300 m/s *V*: 0 ± 200 m/s *W*: 0 ± 250 m/s Delete vector if Q peak ratio < 3 Median filter: strongly remove & iteratively replace with removal if diff to avg. > 3x stdev reinsert if diff to avg. < 4x stdev Remove groups with < 10 vectors Reapply allowable vector range
Append Data Set	Reorganize computed vector fields	Append to all other runs for same field of view
Vector Statistics: Vector Field Result	Compute statistics for all runs of each field of view	Compute means, standard deviation, processing uncertainty

Once calibrated, the double-frame image groups are processed using the settings given above in Table 7. These settings are optimized to minimize noise in the images as well as boost gain in the mixing layer. The settings are based upon a common base that this lab uses for similar Mach number flows. It should be noted that in the vector-calculation step, for SPIV at least two cameras are required in order to have differing views of the same particles; these differing views are used to compute the out-of-plane (*w*-axis) component of the vector. Furthermore, these cameras have viewing angles offset from the normal in order to better capture the intensity change. In doing so, only a fractional portion of the image would necessarily be in focus; to alleviate this, a Scheimpflug adapter is used, offsetting the angle of the lens from that of the image sensor. A tilt angle may be found for moderate (30-45°) offset that puts the entire image plane in focus albeit at non-uniform magnification, known as the Scheimpflug condition. Post-processing of the vector images was performed to filter poorly correlated vectors, as presented in Table 7.

2.3.6 Filtered Rayleigh Scattering

The data obtained through Filtered Rayleigh Scattering (FRS) is the second of the two primary advances of this work. FRS temperatures results were obtained along the spanwise center of the test section, streamwise through where the flow is thermally fully developed. Data were obtained from *y*-values between ±20 mm, just as for the SPIV, allowing for analysis well into the thermal freestreams of both the primary and secondary flows. Figure 26 below shows the notional FRS equipment schematic with arrows indicating the flow of information for each image taken.

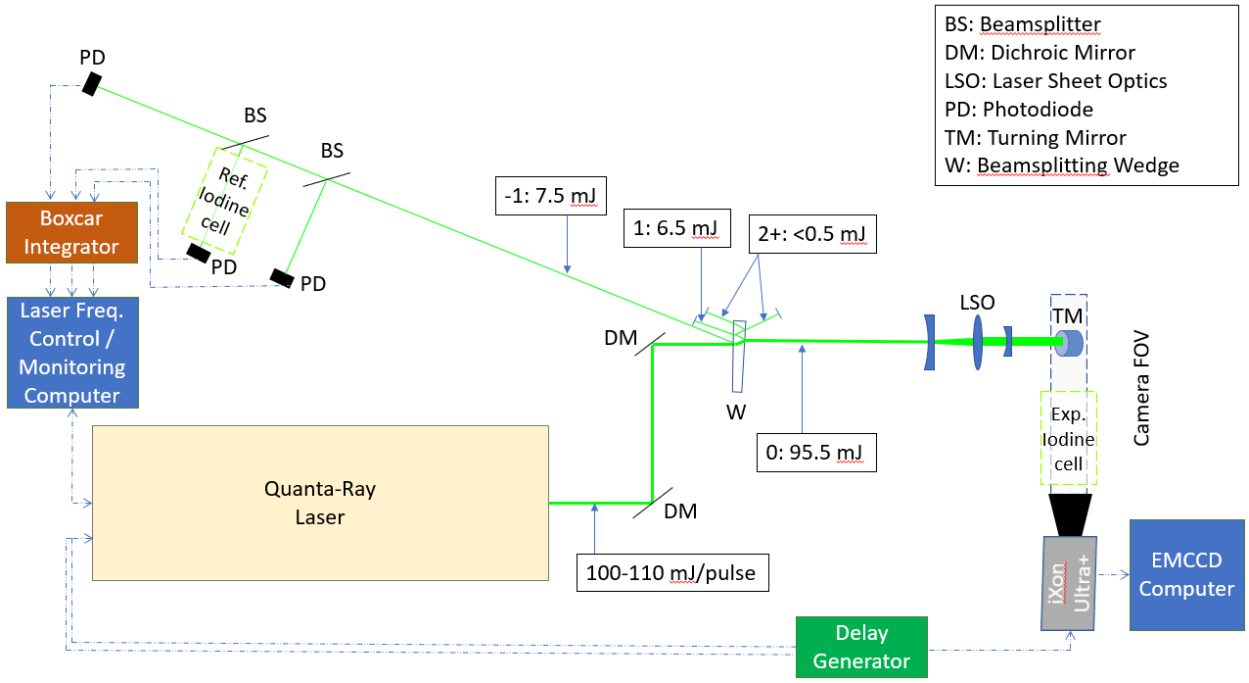

Figure 26. Notional FRS equipment schematic

Table 8. Overview of FRS Components

Component	Description	Parameters Used
Andor iXon Ultra+ Camera	EMCCD camera with 512x512 pixel resolution	Pre-amplifier gain of 5.0x E-M gain of 12x
Nikon Nikkor 85mm f/1.4 AI-s camera lens	85 mm focal length f/1.4D max aperture	Empirically focused with aperture set at f/1.4
LaVision Type 11 Calibration Plate	Double-sided, dual level marker plate	--

Table 8 (cont.). Overview of FRS Components

Component	Description	Parameters Used
Quantum Composers 9514 Delay Generator	Timing pulse generator to sync camera and laser	Q-switch delay = 164 ns
Spectra-Physics Quanta-Ray GCR 230 Laser	Nd:YAG laser Frequency doubled to 532 nm Nominal power of 110 mJ/pulse	Full oscillator power with no amplifier Fine frequency control via LabVIEW computer
2x Iodine Cells	Provides molecular absorption filter to provide measurement basis	Ref: Sidearm temp = 25 C Exp: Sidearm temp = 100 C
3x Thorlabs DET10A photodiodes	Si-based photodetector 1 ns rise time	--
Laser Sheet Optics	Plano-concave cylindrical lenses (f = -50 mm and f = -20 mm), plano-convex spherical lens (f = 200 mm), dichroic turning mirrors (coated for 532 nm)	Empirically located for desired sheet thickness (>1 mm) and streamwise length (20-25 mm)

Table 8, on the previous page and above, gives an overview of the components used for the FRS measurements. Two computers running LabVIEW are also utilized, one for frequency control of the laser and recording of the photodiode outputs, and one for the normal tunnel operation. Initial frequency scans of the laser, including the linear fit of the input voltage to output frequency, were accomplished. These initial frequency scans had the dual purpose of detailing the

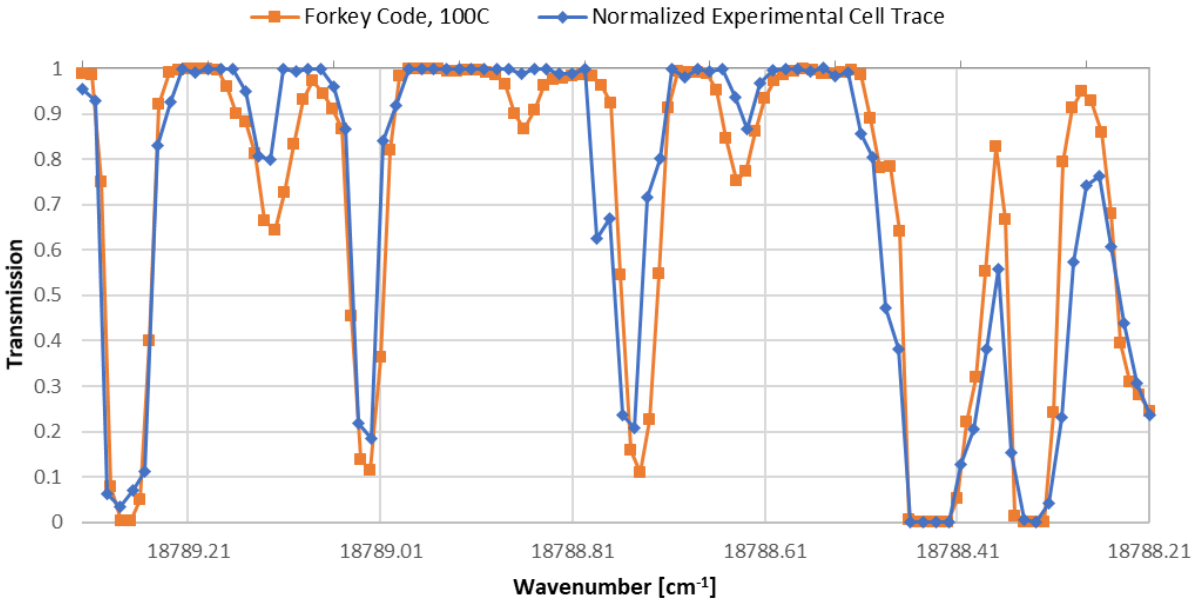

Figure 27. Absorption line comparison of Forkey code and experimental cell

absorption profiles of the reference and experimental iodine absorption cells. The absorption lines of the experimental cell are shown with comparison to the predictive code written by Forkey et al. in Figure 27, with good overlap throughout the operating range of the laser. [35] In particular, the strong absorption line at 18789.27 cm^{-1} and the twin absorption lines around 18788.37 cm^{-1} are rendered well by the cell. The former line was chosen as the nominal operating point of the experiment, with the input frequency at the center of the absorption line.

Given this absorption line setting, initial background and reference flatfield images were obtained for intensity normalization of the flow-on FRS images. A major benefit of the iodine cell is its ability to inhibit the transmission of strong reflections due to Mie scattering in the field of view. Therefore, stray oil particles or other laser reflections from the tunnel walls are negligible; this is crucial as Rayleigh scattering, being an elastic effect, gives off a fairly weak signal. Figure 28 shows the utility of the absorption cell, with the laser frequency set to the center of the absorption line in one image and outside of the line in the other. Without such filtering, the particles would at best wash out the information from the Rayleigh scattering if not damage the sensor due to the high gain setting needed to resolve the signal in the first place.

(a) 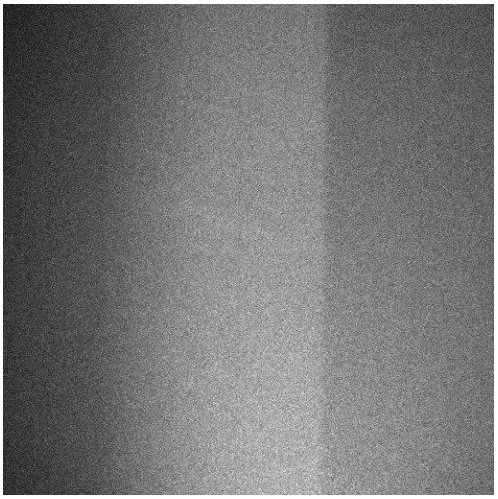 (b) 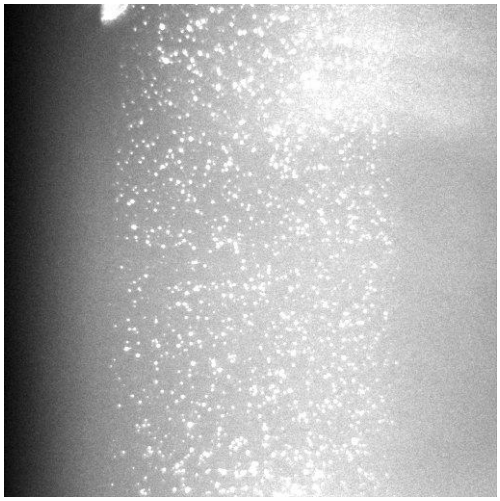

Figure 28. Comparison of Filtered Rayleigh Scattering signal (a) with filter and (b) without

During the FRS data collection, the outputs from the photodiodes were captured as well as the recorded laser frequency and its build-up reduction time (BURT) value. The BURT, a measure of the main laser pulse build-up, is a crucial component in monitoring the spectral output of the laser, of paramount interest during FRS. When the BURT exceeds a set limit, this indicates that the seed laser has "unlocked" from the desired frequency. This in turn means that the output laser beam from the laser head will be spectrally broadened—in turn meaning that the iodine cell will not absorb the reflected light as it is not all at the correct frequency. Each shot with a BURT above the cutoff, or with particle intensities above a given threshold, was discarded prior to image processing. The processed temperature field results, as well as a greater discussion of the processing method, are detailed in Chapter 5.

Uncertainty of the Filtered Rayleigh Scattering technique was evaluated using a procedure developed by Forkey et al (1998).[36] While time limitations in the project have precluded such an analysis at the time of the publication of this work, it will be completed prior to the conclusion of the project. This uncertainty analysis may be found at the project website; a discussion will be included with the results.

CHAPTER 3: SCHLIEREN, PRESSURE, AND TEMPERATURE PROBE MEASUREMENTS IN A COMPRESSIBLE MIXING LAYER WITH A THERMAL GRADIENT

3.1 Schlieren Visualizations

3.1.1 High-speed Schlieren Videos

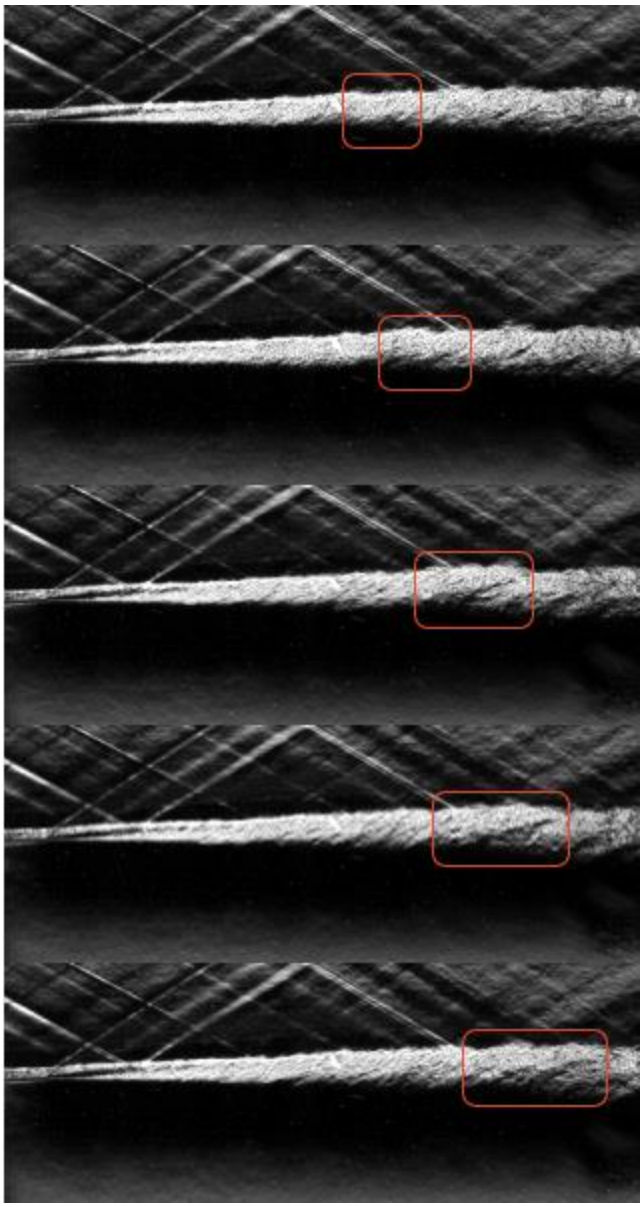

Figure 29. Sequence of high-speed schlieren frames showing growth of a braid structure

On the right in Figure 29 is a sequence of stills from the high-speed (120,000 frame/second) schlieren movies. This sequence in particular highlights the utility of the movies, in that the formation and movement of structures within the mixing layer may be visualized individually and used for later analysis and correlation with the other measurements. From this sequence, taken over five frames spanning slightly less than 200 milliseconds in time, two main features stand out. The first feature, valuable more for its validation of the operating condition, is the changing shock/expansion wave coming off the splitter tip. This switching between the two features is highly indicative that the static pressures in the two freestreams match closely at the splitter plate and therefore is a useful mixing layer condition. The second feature, however, is one lending insight into the shear layer itself: the growth of a braid structure in the shear layer. This structure, which begins in the first frame as a small

rippling band in the mixing layer, grows over the next two frames into a clearly visible feature in the flow. As it continues to pass down the test section, the braid elongates; the upper portion of the braid stretches out as the velocity differential across the shear layer takes effect. Furthermore, this sequence of images serves to illustrate the insight of Kim with respect to the relative size of the structures on the two sides of the mixing layer[14]: as the high-speed side of the braid moves in time, it stretches out and remains small in amplitude, whereas the low-speed edge of the braid is able to remain larger and extend further downward as it moves along the shear layer.

3.1.2 Full-resolution Schlieren Visualization

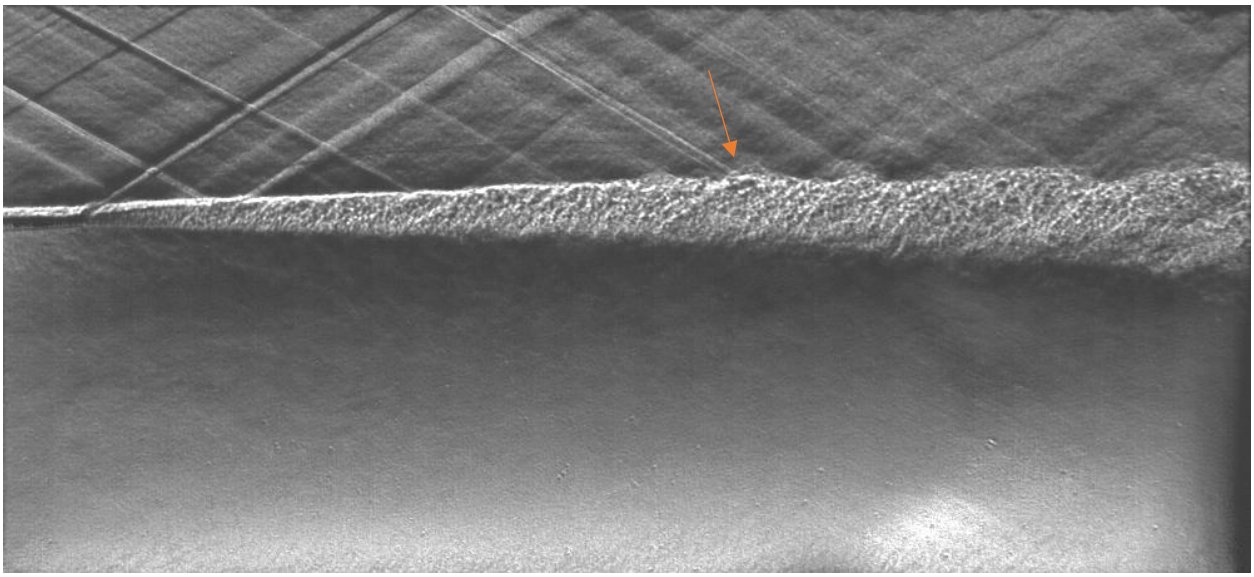

Figure 30. Instantaneous full-resolution schlieren visualization with arrow marking impingement of reflected wave

The full-resolution, slower frame-rate schlieren images, an example of which is shown above in Figure 30, show much more of the shock structure and better visualize the braids along the mixing layer. The interaction of the mixing layer with the waves becomes much more evident at higher resolution; note the increase of the braid height at the point where the reflection of the splitter tip wave impinges back on the shear layer. This, in addition to the shear layer's post-shock increases in the number of fluctuating structures (braids and rollers), aligns with the findings of Zhang that would expect such behavior after the impingement of the wave into the shear layer.[12]

Minor waves are noted to come off of the braids in the mixing layer and into the primary stream, reminiscent of the canonical wavy wall supersonic flowfield, as discussed by Rossman et al.[10]

The mixing layer qualitatively appears to be possibly fully developed about 4/5^{ths} of the way across the field of view: the two final braid structures are nearly identical to one another, and the visual growth rate of the shear layer is nearly linear. This will be investigated and verified by the PIV measurements in Section 4.3. The flattened structure is expected for such a convective Mach number; the trend Kim noted of larger structures on the secondary side of the mixing layer appears to be corroborated here, as the instabilities clearly begin from the bottom half of the shear layer and stretch to the top.

As a minor remark, there is of course the matter of the reflected shock/expansion wave off of the top wall of the test section and possibly interacting with the shear layer itself before reflecting back up again. Given that this would certainly affect the velocity measurements, and likely all the other measurements as well, it must be given some discussion. There are two main ways to check whether the impinging wave affects the shear layer: whether it bends either away from or nearer to the shock, which can be easily seen in the schlieren, or by examining whether the pressures along the shear layer remain relatively constant throughout. The first requirement for a stable testing condition is met by checking the schlieren visualizations and may also be used in the PIV field results in the streamwise *U* velocity trends. The second requirement is investigated through analyzing the static pressure along the length of the shear layer—this confirmation of a stable operating condition being the primary goal of the static pressure measurements.

3.2 Static Pressure Tap Measurements

While meeting the primary goal of the static tap measurements is clearly key to the work, the secondary goal is no less important: checking the strength of the shocks in the primary stream.

Figure 31 below shows a comparison between the present case of interest, and the work of Kim et al. on the same tunnel, for the most similar case, Case 4 (M_c = 0.690).[13]

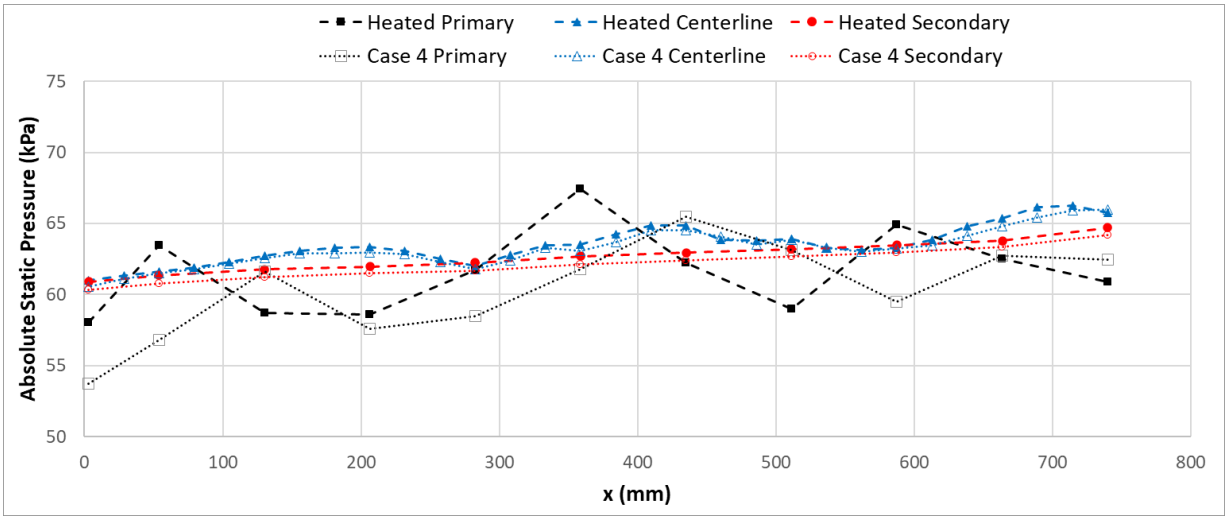

Figure 31. Comparison of sidewall static pressures for current work (Heated) and M_c = 0.690 (Case 4) of Kim et al.

Two remarks are immediately clear from the comparison: first, that the static pressure along the centerlines, as well as the secondary flows, is almost exactly the same between the cases. This, while it may be surprising at first glance, makes sense with thought: the static pressure in the secondary is what is being adjusted in order to match to the pressure of the supersonic primary stream. The second remark is much more interesting: that the primary stream has marginally stronger shocks, therefore at higher angle and occurring earlier, in the heated case when compared to Case 4 of Kim. These shocks are represented in the visualizations by the static pressure peaks in the primary stream; for the heated work, the shock peaks (and expansion troughs) occur a tap before that of the non-heated case. The slightly stronger shock that the heated case experiences is inferred to be due to the increased density difference between the primary and secondary streams: while the primary stream has largely the same incoming characteristics as what Kim et al. found, the secondary, with its nearly doubled static temperature, has a correspondingly nearly halved density. Therefore, in order to match the post-shock characteristics, the shock must be stronger

than in the case of Kim et al. Furthermore, this stronger shock (and its corresponding reflected second shock) also has implications for the operating condition. Due to the increased strength of the shock, it is likely that the window for the operating condition would be much tighter than what would be seen for a non-heated case. The stronger reflected shock has the ability to "bend" the mixing layer downwards, affecting the accuracy of the data; this would be most visibly seen in the schlieren visualizations and velocity measurements, although all data would of course be affected. Also of interest when the velocity and turbulence statistics are measured is whether the region where turbulence would be fully developed will come sooner than in the work of Kim et al.[13] If so, some consideration may be due as to whether the reflected shock off of the top wall has any effect on the turbulence statistics.

3.3 Temperature Probe Measurements

3.3.1 Total Temperature Traverses

Total temperature traverses were obtained using the TAT probe with the approach outlined in Section 2.3.3.2. These traverses were made at four streamwise positions, at x = 24.7, 125.8, 204.9, and 284 mm, and encompassed the entirety of the thermal mixing layer, extending well into the thermal freestreams on both sides of the mixing layer. A minimum of four traverses per position were performed, with the values at each position within the traverse averaged and then normalized between the stagnation temperatures of each freestream. It should be noted that this normalization was performed given

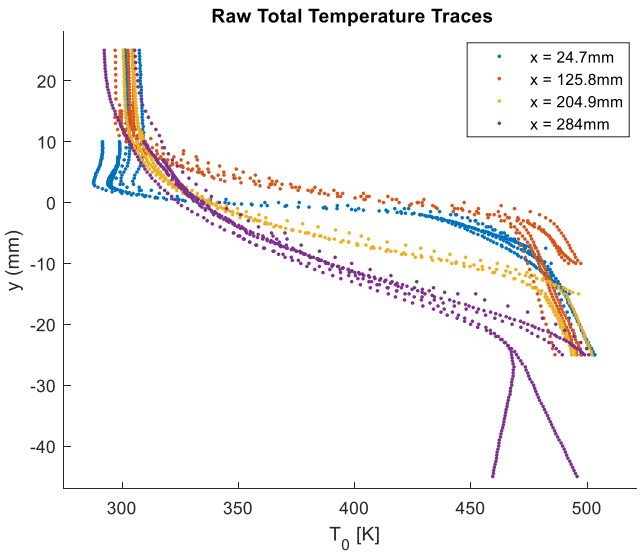

Figure 32. All raw total temperature traces

the simultaneous values *in time*, as the freestream stagnation temperatures varied somewhat as the tunnel was run and therefore must be synchronized with the correct probe temperature value. This behavior may be seen in Figure 32 with the non-normalized total temperature values (particularly in the secondary freestream where the value does come to a constant value); it should also be noted that an additional comparison run was made at x = 284 mm to verify that there was no difference traversing the probe from the secondary to the primary or vice versa. Once verified, all later traverses were made from the secondary to the primary stream; this was done to protect the probe from experiencing the shocks produced during tunnel startup.

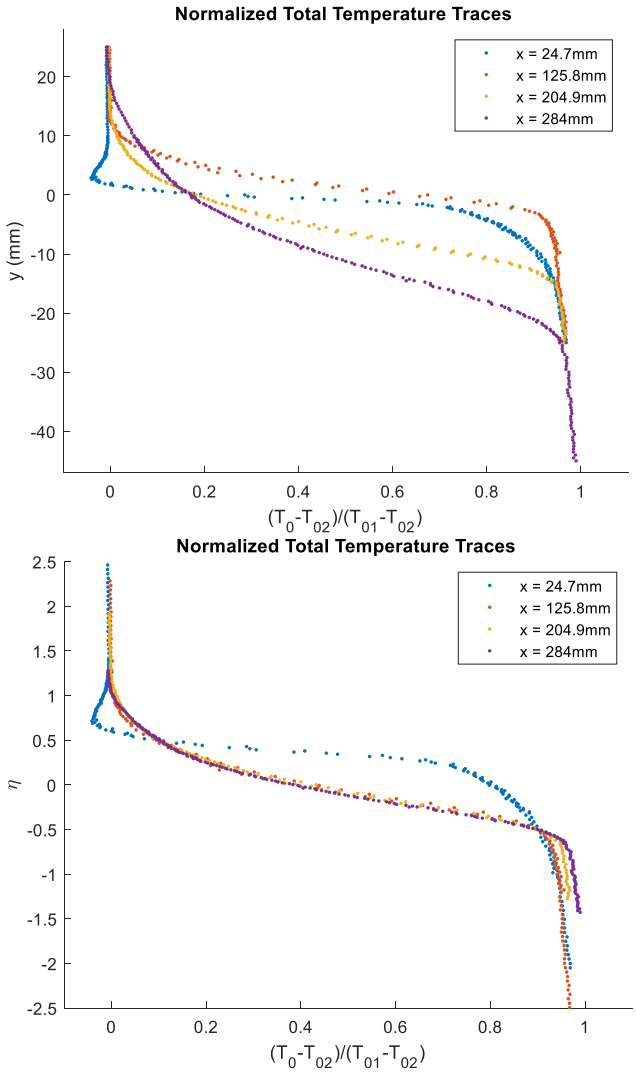

Figure 33. Normalized total temperature traverses plotted on raw and normalized transverse position

The normalized total temperature traverses were then used to determine the thicknesses of the thermal freestreams using a 10% ΔT_0 definition in the same vein as the 10% ΔU definition for velocity thickness. Equation (13) gives the normalized y-parameter η, where y_0 is defined as the average position between the edges of the thermal layer y_1 and y_2, and b as the distance between the two—the thickness of the thermal mixing layer at that point.

$$\eta = \frac{y - y_0}{b} \tag{13}$$

The η parameter was then used to create traces normalized by the thickness of the thermal layer, along the transverse direction to the flow. These normalized traces may be seen in Figure 33 on the previous page. It is immediately clear from the normalized traces that the thermal mixing layer is fully developed at or before x = 125.8 mm; this is because the normalized traces essentially collapse completely upon each other after this location. The normalization procedure also increases the resolution of certain effects that are difficult to discern from the raw traverse data, best highlighted from the x = 24.7 mm traverse. There appears to be a deficit occurring in the total temperature, to values much less than that of the primary freestream value, an effect not anticipated prior to data collection. This indicates a thermodynamic effect taking place within the near field of the splitter plate, possibly due to residual cooling effects of the plate itself. This deficit is an effect that bears greater investigation, indicating a possible effect on in the mixing that had not been highlighted by the schlieren or velocity results. From the normalized traces there is also a slight effect that is most noticeable in the normalized temperature-η plot in the secondary thermal freestream but is seen in both plots. This effect, where the stagnation temperature as measured by the TAT probe does not quite reach the level found in the secondary stream stagnation temperature, is attributed to both slight time difference in the measurements (keeping in mind that the tunnel temperature is constantly falling as it is run) as well as entropy effects that are more pronounced further downstream and nearer to the shear layer. However, this is a minor issue that does not affect the quality of the normalized data, particularly once the static temperatures are considered.

3.3.2 Static Temperature Traverses

Static temperatures were calculated from the total temperature traverses using PIV velocity data to inform the adiabatic relation for each point of the traverse; see Figure 34. This determination was not able to be performed for the x = 284 mm traverse, because there did not

exist any PIV data for that streamwise location. These static temperatures show the same general spatial trend as the total temperatures; they normalize similarly, using the same method utilized for the total temperature traverses, and the profiles have approximately the same shape across the mixing layer. What is notable is their highly linear change in static temperature across the thermal mixing layer, especially in comparison to the stagnation temperatures, at the fully developed positions. While the first position appears to indicate something near to this linear behavior, it is less pronounced than at the other two positions. This linearity in the static traces may be partially attributable to the thermocouple's response time, but this is *extremely* unlikely due to the high responsivity of the probe as well as the extremely low variation across the ensemble for each position; it will be fully investigated with the Filtered Rayleigh Scattering temperature results in Chapter 5.

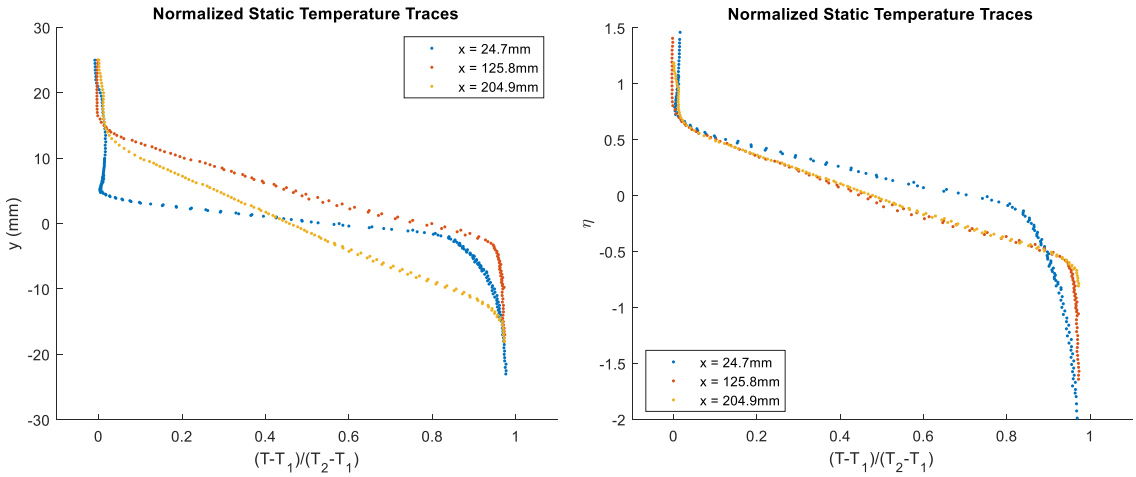

Figure 34. Normalized static temperature traverses plotted on raw and normalized transverse position

The two downstream temperature profiles, once normalized and plotted against η, collapse to nearly the same profile, indicating that the static temperature distribution remains self similar. This lends further evidence that the thermal mixing layer is fully developed, even as the static temperature calculation has a dependence on velocity with the total temperature profiles. Given this behavior, the thermal layer growth rate was calculated from *b* thickness data at these two

locations. The $^{db}/_{dx}$ value from this analysis was found to be 0.0946. Additionally, when the conversion to the static temperature occurs, the temperature deficit effect noted in the total temperature traverses is substantially reduced; indeed, in the normalized-T vs η plot, it would be easy to miss the slight deficit if it was not noticed from the earlier stagnation temperature plots. However, even with the less pronounced deficit, the static temperature does have a sharply defined interface between the freestream and mixing layer at this early position. Again, this is an effect that bears further investigation with the Filtered Rayleigh Scattering results, as well as in future works.

CHAPTER 4: VELOCITY FIELD MEASUREMENTS IN A COMPRESSIBLE MIXING LAYER WITH A THERMAL GRADIENT

4.1 Challenges

A variety of issues slowed and delayed the PIV data collection process for this heated, compressible mixing layer; these were due to initial inexperience with the technique on behalf of the author, as well as due to the unique thermal environment that the experiment required. Ultimately, high-quality data were recorded that achieved the project's requirements. These challenges and their solutions are detailed in the following section primarily to assist future experimental work of a similar type.

4.1.1 Seeding Injection and Density

For high-quality particle image velocimetry measurements, the particulate seed must be evenly distributed throughout the field of view that is to be measured, allowing the processing algorithm to track the seed particles across image pairs. The required particle density is primarily dependent on the speed of the flows and seeding method, but is also affected by features in the flow, especially shocks and vortices. In the complex heated mixing layer that is of interest here, an additional difficulty is that both streams must be seeded evenly. Each stream will have its own seeding requirements, particularly with their different flow rates, pressures, and temperatures. Two methods of seeding were eventually used in this experiment, one for each stream: a commercial smoke generator for the high-speed primary and a Laskin-type nozzle seeder for the low-speed secondary, both of whose capabilities are briefly described in Table 6 of Section 2.3.6.

Seeding the streams evenly can be described to be as much of an art as a skill, where minor adjustments to the seeder or even the flow itself can have outsized effects on the quality of the images obtained. Furthermore, for the liquid seeders that were used in this study, oil droplets

accumulate along the top, bottom, and sidewalls of the tunnel over the course of the tunnel runs. This in turn leads to buildup of oil streaks across the viewing windows, blurring or even outright obscuring the views of the imaging cameras. As should be then clear, overseeding the flow can

Figure 35. Examples of seeding quality (left-right): Overseeded primary stream, Acceptable, Good

be just as detrimental as underseeding, particularly in that it may cause the aforementioned negative effects over the course of a run. It should be noted that while purging runs (runs that do not have any seeding and are rather used to clear accumulated oil from the tunnel) do take place, they cannot fully clean the inside of the tunnel. Rather, over time, a pseudo-steady-state is reached with respect to the amount of accumulated oil in both streams of the tunnel, but it must again be emphasized that individual runs are improved by meeting an optimum seeding condition. Above, Figure 35 shows different levels of seeding quality.

4.1.2 Secondary Seed Persistence

The largest challenge in the experiment to be overcome was the lack of seed persistence in the secondary stream due to its high temperature. During initial PIV setup, a two-component planar configuration was used to obtain early flow images, with the goal to understand the setup process and workflow with fewer variables. It was during this setup period that an intermittent phenomenon was noticed in the images that may be seen on the next page in Figure 36: a clouding effect taking place in the secondary stream and extending into the mixing layer.

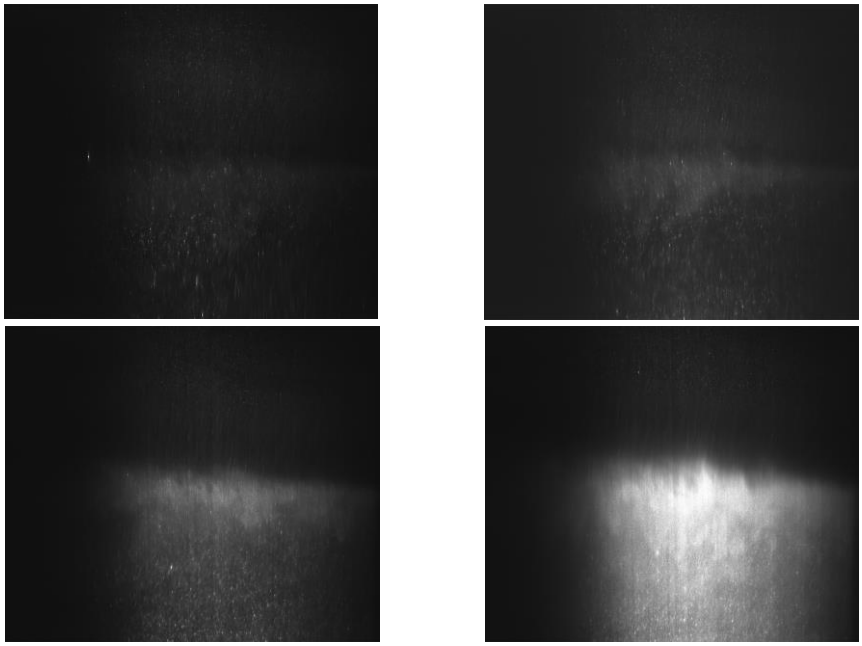

Figure 36. Development of oil clouding in test section (Time progression: left-right, top-bottom)

Initially, it was thought that this clouding effect was due to water vapor in the secondary flow that was condensing upon meeting the much colder primary flow. Condensation had been seen previously in the same lab and even in the same wind tunnel when ambient humidity was high, especially if the facility dryer desiccant material was nearing end-of-life. With the initial seeding method being an ambient air entrainment method where a commercial seeder would exhaust into an open pipe, the entrainment valve was adjusted along with other checks. The phenomenon was initially judged to not occur if the temperature of the secondary stream was reduced slightly, generally below 470 K. While this was not ideal, particularly as the thermal differential between the streams was the crux of the experiment, it was close enough to the original proposed operating conditions to be within reason.

However, after the changeover to the eventual stereo-PIV setup had been completed and data runs recommenced, the clouding returned even at the lower temperatures. Two items were added to concerns at this point: the facility dewpoints had been verified to be below even that of the primary stream's static temperature, and the clouding intensified over time. While still

operating under the assumption that the clouding was water vapor condensation, efforts shifted to remove all sources of water vapor. A series of changes occurred to the secondary seeding setup as a result, with the eventual configuration using a blanking plate over the main entrainment valve, with an NPT fitting tapped into the plate. A Swagelok adapter was threaded onto the fitting, with ¼" tubing connected into a 3D-printed part to fully capture the smoke particles with minimal ambient air. When further testing of this configuration continued to show the clouding effect, consideration was given to whether the smoke oil itself had agglomerated water molecules from the air. Saturation of the oil with water could, in the higher-temperature environment of the secondary stream, possibly cause water vapor to form in high enough quantities to create condensation in the mixing layer when coming into contact with the cold primary stream. However, after a full replacement of the smoke oil with new, previously sealed oil, the clouding still occurred. It was at this point that attention turned to the smoke oil and generator itself.

Contact was made with the manufacturer of the smoke machine and smoke oil, requesting information on properties of the oil itself, as well as the method used within the generator to create the smoke particulates. According to the manufacturer, the ViCount machines burn the oil in the heat exchanger of the device, where the pressurized stream of nitrogen moves the combustion products out of the nozzle. The gaseous vapors from the combustion process then condense in the cooler outer air that the particles are exhausted into and create the smoke cloud. However, the smoke generation process is interrupted if exhausted into flows at temperatures higher than 450-470 K, when the heated flow is at or higher than the temperature in the ViCount machine. The high temperature sustains the occurring reactions; the products of these reactions then rapidly condense in the cold air of the primary stream and cause the clouding effect. Further discussions

were made with the manufacturer as to whether a higher-temperature product existed; a retrofit was offered, but at too steep a cost both in terms of time and money to be viable for this project.

Table 9. Comparison of Different Liquid Seed Properties

	180 Smoke Oil	DEHS	Avocado Oil	Olive Oil
Flash Point	112-160+ C	200+ C	330+ C	320 C
Smoke Point	140 C	190 C	250-270 C	160-205 C
Boiling Point	218-330 C	232-249 C	300+ C	570 C
Surface tension @ 23 C (180 C)	N/A	32 mN/m	--	31.9 mN/m (23.1 mN/m)
Refractive index @ 20 C, 589 nm	1.472	1.449	1.46-1.47	1.44-1.47

An investigation into finding an alternative method for seeding the hot secondary stream then began. Solid particulate methods, such as using titanium dioxide, were not strongly considered due to safety concerns; the facility was not designed to be seeded in such a way, and was without a method for safely collecting the material without exhausting the material either into the lab or outside. Therefore, liquid seed was still the primary focus of the investigation for an alternative. After a suggestion from a NASA collaborator who had tangential experience with a high-temperature experiment, avocado oil was cross-compared with other high-temperature organic oils as a possible seed material, as well as other nonorganic compounds that had been previously used by the lab in the past. Table 9 above summarizes the comparisons made.

Figure 37. Secondary seeding configuration with Laskin Nozzle seeder

After further investigation, avocado oil used in a TSI Model 9307 Laskin nozzle was chosen as the new seeding method; it has the highest smoke point of the oils investigated while still having fairly similar properties to these better known oils. As a side benefit of previous modifications to the seeding setup, the Laskin nozzle

exhaust could directly connect to the NPT port on the previously described blanking plate with minimal extra requirements. This approach is shown on the previous page in Figure 37; note the ball valve, used to prevent backflow of hot air to the seeder during tunnel warmup and cooldown. This ball valve is only opened while the tunnel is operated at full flow: the secondary flow pressure is sub-atmospheric and therefore will only entrain the seeding flow.

4.1.3 SPIV Camera Alignment and Calibration

The third challenge faced in obtaining the SPIV data came as a part of the physical setup, as haste to obtain data quickly after the avocado oil solution was found, combined with inexperience in setting up stereo-PIV, led to slight misalignments in the cameras along the streamwise-, or *x*-axis, for some of the data collected. As a result of the misalignment, the spanwise *w*-component of the velocity vector was biased depending on the angle of the cameras (positively for the first two fields of view in the streamwise direction, negatively for the third).

Typically, for slight misalignment of the cameras, especially in cases where the angles of the two cameras are not exactly equal with respect to the laser sheet, the stereo self-calibration routine in DaVis can correct the image mapping. This routine uses a common reference point in images from each camera to create an initial disparity mapping before using a set of images to create a correction mapping to match the images to each other. For cases in which the self-calibration is unable to correct the image mapping, continued realignment of the cameras must take place. However, because this self-calibration is a built-in feature of the PIV processing, it was not immediately evident to the author to verify the image alignment using the self-calibration until processing had begun and all images obtained. As a result, images obtained in the first and third fields of view both had to be discarded; the third field of view was retaken to verify the Reynolds stresses throughout the fully developed region. In order to prevent this issue from occurring again

when data were retaken, a 3D printed plate was created to assist with the alignment process. This plate, measuring 140x115x3 mm, has equidistant holes that go through its entire depth to serve as dual-sided markers, as can be seen in Figure 38.

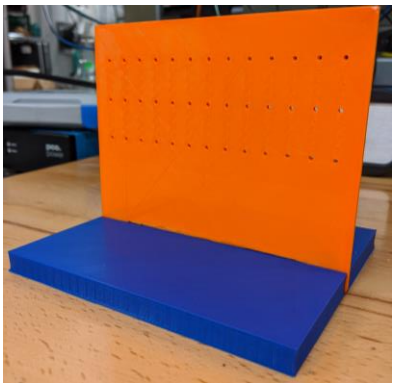

Figure 38. 3D-Printed alignment plate

By aligning these holes, the translation as well as rotation of the cameras may be easily matched. Furthermore, because the plate was designed to be approximately as wide as the laser sheet, the illuminated field of view during operation requires minimal final adjustment in the camera's focus using the laser-sheet illuminated particles themselves after being focused on the alignment plate. The second field of view, given the increased experience with how to conduct the stereo self-calibration in DaVis, was able to be retained for use without re-recording. While initially there was miscalculation of the *w*-component of the velocity vectors, after correction with the self-calibration, the results became accurate, with a high degree of confidence.

4.2 Boundary Layer PIV Results

Boundary layer PIV results were obtained for three of the four incoming boundary layers; the reasoning for this decision as well as the method of acquisition is discussed in Section 2.3.4. For the three boundary layers of interest, a mean two-component velocity profile as well as the Reynolds stresses were determined for a slice of the velocity field very near to $x = 0$ mm (i.e., the splitter tip). While optical access limitations precluded measurements at exactly $x = 0$, the boundary layer is shown to be fully developed prior to this point, such that all profiles are assumed to be applicable. For the boundary layers along the splitter plate, while the plate does technically move slightly under full-flow conditions, these effects were assumed to be negligible on the

boundary layer. Ensemble sizes for each boundary layer dataset ranged between 900 and 1200. These profiles were obtained in the boundary layer at locations as near to the wall as possible.

In order to determine the parameters used to define each boundary layer, the procedure outlined by Sun & Childs (1973) was utilized. Their procedure prioritizes elimination of the artificial non-zero velocity gradient at the edge of the wall-wake profile used in the Matthews' formulation. A departure in the Sun & Childs method that should be noted is their choice of U/U_∞ to be 0.995 at the boundary layer edge, as opposed to the conventional 99% definition.[37,38] A method of least-squares fits a curve to the experimental data, which then is used in the modified wall-wake formulation with initial guesses as to the boundary layer thickness, δ, and skin friction coefficient, C_f. Plots showing the velocity profiles in both outer- and inner-wall normal coordinates of the three boundary layers of interest may be seen on the next page in Figure 39; the Reynolds stresses are plotted on the following page in Figure 40.

The best-fit mean velocity profile as calculated from the Sun & Childs procedure is then utilized to determine the incompressible displacement thickness, δ^*, incompressible momentum thickness, Θ, shape factor, $H = \delta^*/\Theta$, and the wake strength parameter, Π, through numerical integration. These integral parameters are listed for all four boundary layers of the experiment in Table 10 with comparison to Case 4 of Kim[13,14]. From the comparison of boundary layer results, it becomes clear that the thermal boundary layers are much thicker than the corresponding ones of Kim, with correspondingly higher coefficients of friction except for the splitter plate bottom wall, which has nearly the same C_f between the cases. Of major note is the splitter plate top boundary layers: the 99.5% thickness extends further into the freestream by a factor of about 4/3—a major departure considering that the flow itself is the same. Given the hot splitter plate causing a thermal gradient into the cold primary stream, the boundary layer thickness correspondingly increases.

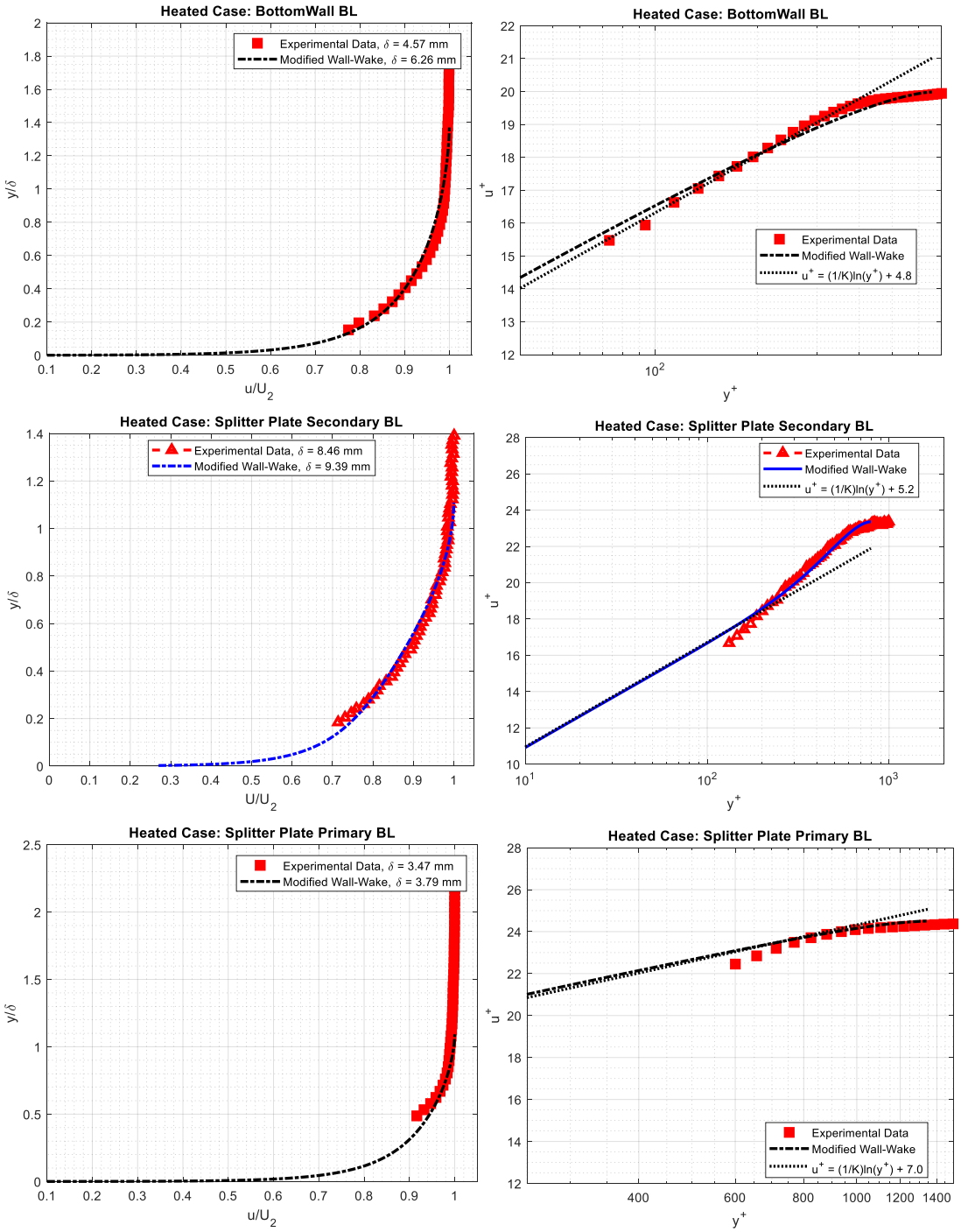

Figure 39. Boundary layers in outer-and inner-wall normal coordinates

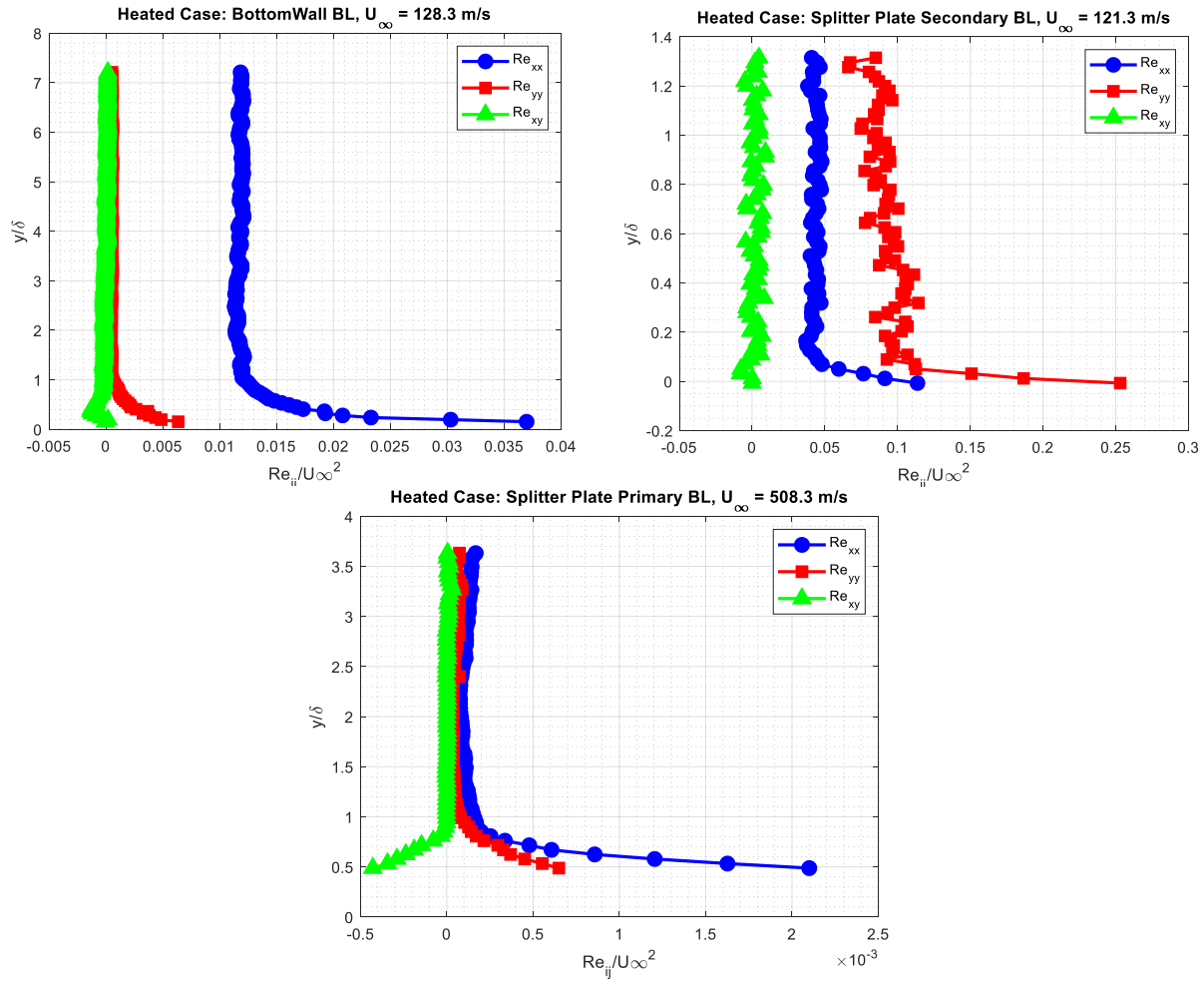

Figure 40. Reynolds stresses in boundary layers

Table 10. Comparison of Incoming Boundary Layers

Case	Location	δ_{99} (mm)	δ^* (mm)	Θ (mm)	H	C_f	Π
Heated ($M_c = 0.541$)	Top Wall*	3.599	0.574	0.429	1.338	0.001561	1.162
	Splitter Top	3.79	0.309	0.246	1.254	0.003332	0.108
	Splitter Bottom	9.38	1.271	0.940	1.353	0.003665	0.597
	Bottom Wall	6.26	0.537	0.417	1.289	0.005007	0.188
Kim Case 4 ($M_c = 0.690$)[13,14]	Top Wall	3.599	0.574	0.429	1.338	0.001561	1.1620
	Splitter Top	2.847	0.514	0.372	1.381	0.001526	1.3996
	Splitter Bottom	4.271	0.617	0.464	1.330	0.003711	0.4884
	Bottom Wall	4.212	0.646	0.474	1.364	0.003547	0.6700

4.3 SPIV Results

Stereo-PIV results were obtained with a minimum ensemble size of $N \geq 3000$ for each field of view. Moments of the instantaneous variations from the mean were obtained up to and including the fourth moment, and Reynolds stresses for the entire stress tensor were computed using the second moment. Uncertainty was calculated for all results, as a compilation of particle, processing, equipment, and sample size effects to the total uncertainty.

4.3.1 Velocity Vector Results

Mean velocity components were computed for all three coordinate directions from the instantaneous measurement ensembles. These results range from 8 to 217 mm in the streamwise (x) direction; they are centered in the transverse y-direction of the test section. As the end-view results from Kim[13,14] showed, there is little variation along the spanwise (z) direction in the mixing layer, as expected. Therefore, these results can be considered to be valid throughout the spanwise width of the mixing layer.

Mean velocity fields may be found plotted in Figure 41. From these mean velocity fields, the most notable feature is the expected slow growth of the mixing layer in the streamwise direction. The effect of the splitter tip shock on the V component of the velocity is also noticeable, although it should be noted that the magnitude of this component is almost entirely less than ±25 $^{m}/_{s}$. This shock, which reflects off the top wall of the test section, impinges on the mixing layer at about x = 120 mm and then reflects back upwards. The modestly positive V component preceding the impinging wave, and negative component after the impingement highlights the feature well. Looking at the U component around the same point, there is a slight upward tilt to the shear layer that then tilts slightly downward after the shock. Eventually, the shear layer straightens off to a flat layer, as seen in the region of x = 150 mm and beyond. The W component, meanwhile, stays

consistently near zero in the freestreams throughout the test section, which is effectively within the uncertainty of the measurements. There appears to be a slight positive bias, about 10 m/s, in the secondary stream, with greater effect near to the shear layer. From the schlieren visualizations, the braid structures indicated a small degree of transverse velocity in the shear layer, which is also seen in the PIV results. Non-physical effects are seen at the interfaces between the fields of view for all components, where the mean fields were stitched together; these, however, are expected in the fields and have little to no negative effect on the results. More worrisome were the laser light reflections, seen most strongly in the W-component after about x = 200 mm. These reflections have effects on the mean velocities as well as all other statistical results; as such, they preclude the use of measurements after this point. Fortunately, the Reynolds stress analyses in the following section indicate that the fully developed region occurs well prior to the region of laser reflections, and thus are of no major consequence.

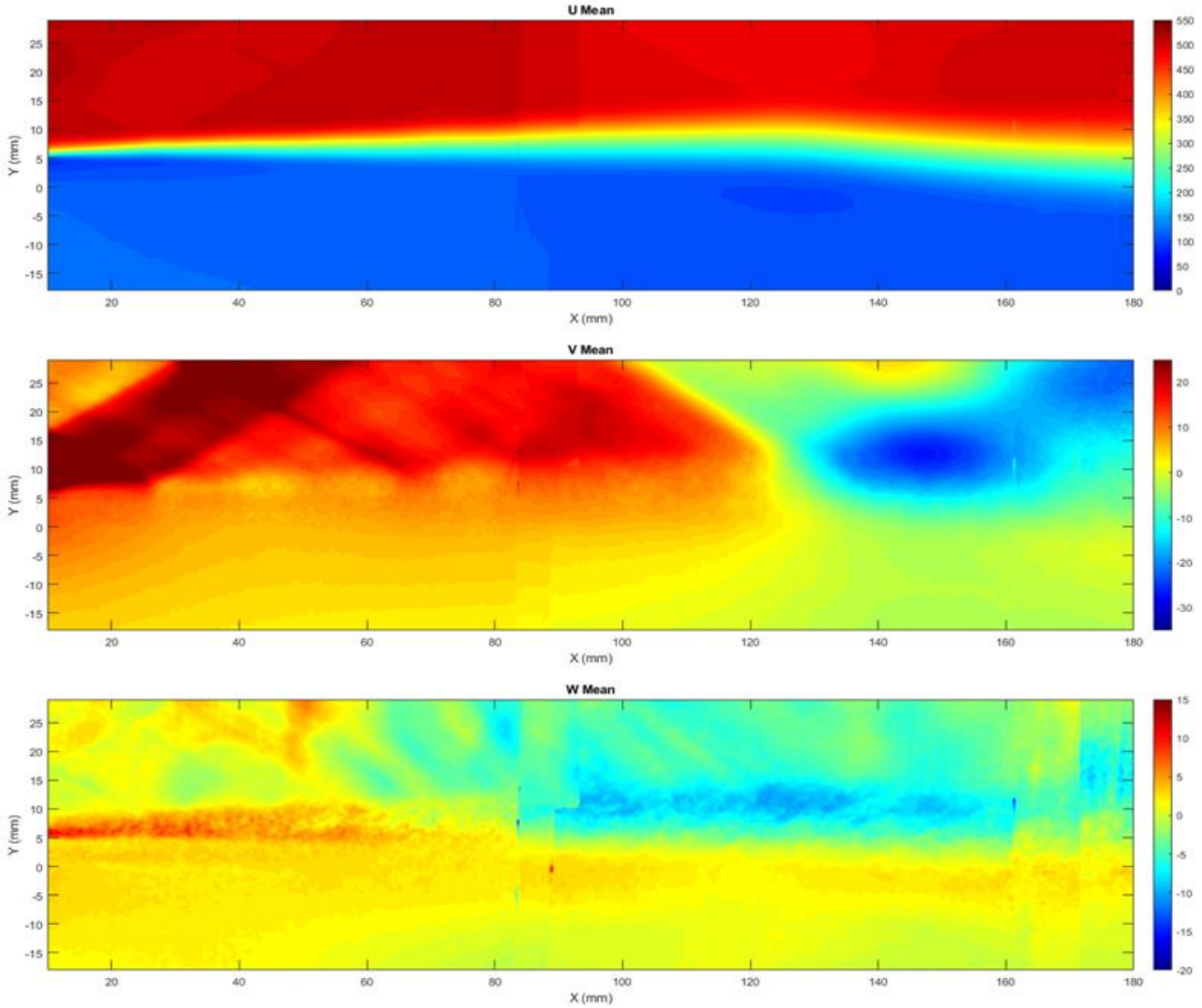

Figure 41. Mean velocity fields for U, V, and W

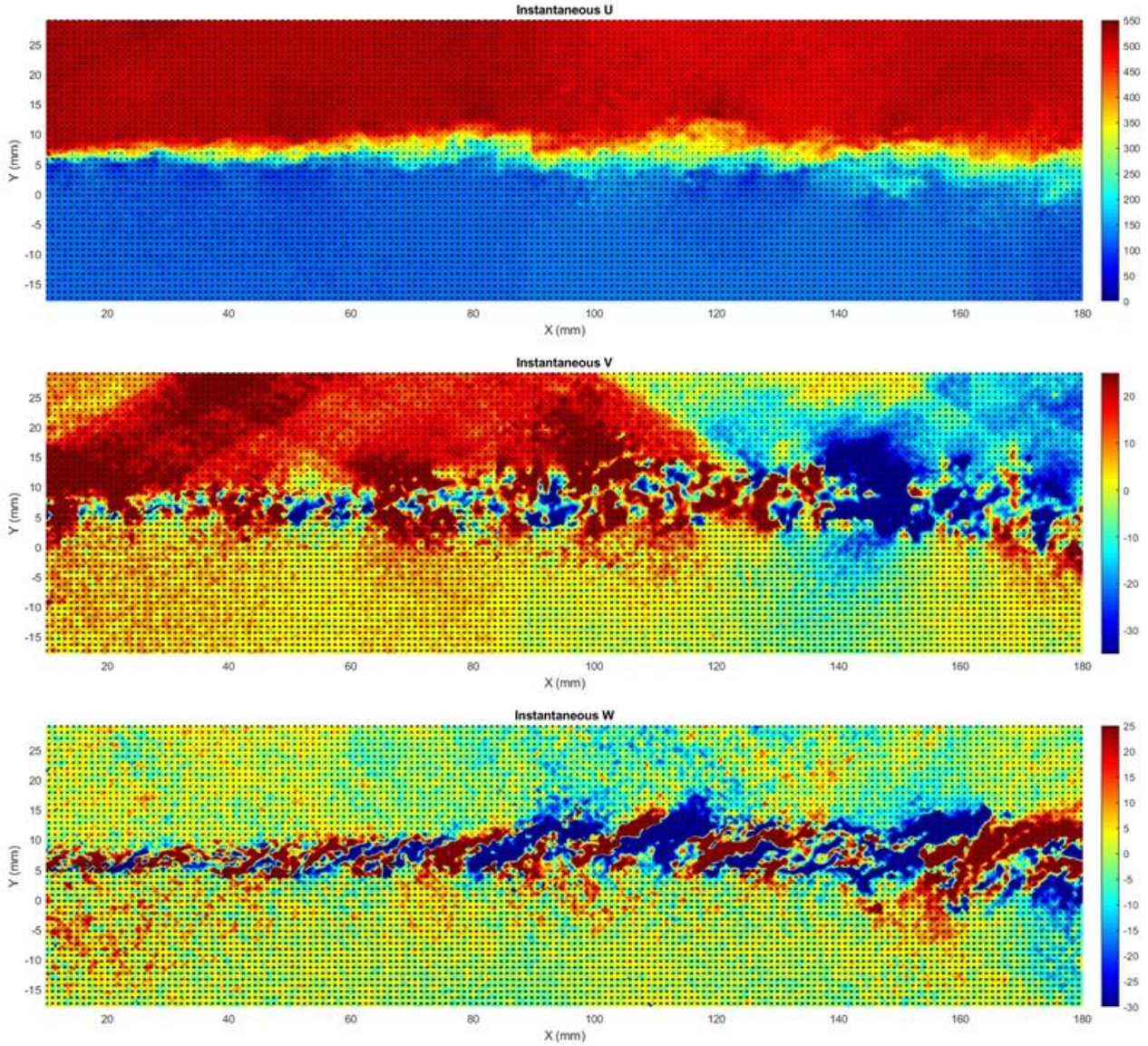

Figure 42. Selected instantaneous vector fields with overlaid instantaneous velocity component contours

Further and arguably deeper insights can be gleaned from the instantaneous results, shown in Figure 42 on the previous page. Here, the resemblance in the instantaneous *u*-component to the schlieren results can be seen. Flow features along the upper edge of the mixing layer show a slight change due to the impinging shock, although more clear is the slight downward bend in the mixing layer, resulting from the shock reflecting from the top wall of the test section and impinging on the shear layer. Additionally, the instantaneous *v*-component clearly shows the shock structure, but more interesting is the flipping in the mixing layer of the instantaneous *v*-component magnitude. A consistent up/down movement of the flow, switching from -30 to +30 m/s occurs as the small-scale mixing structures noted in Kim[14] occur. When considered together with the spanwise switching in the instantaneous *w*-component, it appears that these structures largely line up together, and possibly indicate the existence of roller structures oriented along the streamwise direction.

Additional details may be noticed when the schlieren measurements are considered in tandem with the velocity measurements, as seen in on the next page in Figure 43. With this new lens, it can clearly be seen that the braid structures line up with the velocity fluctuations. Furthermore, the shocks stand out even more strongly in the primary freestream shifts in the instantaneous *v*-component. All fluctuations, in fact, overlay neatly onto the mixing layer as visualized by the schlieren results. When the instantaneous *u*-component is considered with the schlieren, the edges of the mixing layer become even more distinct. In all, the combined schlieren/PIV results stand to show that the instantaneous density gradients line up exceedingly well with the instantaneous gradients in velocity as measured by stereo-PIV.

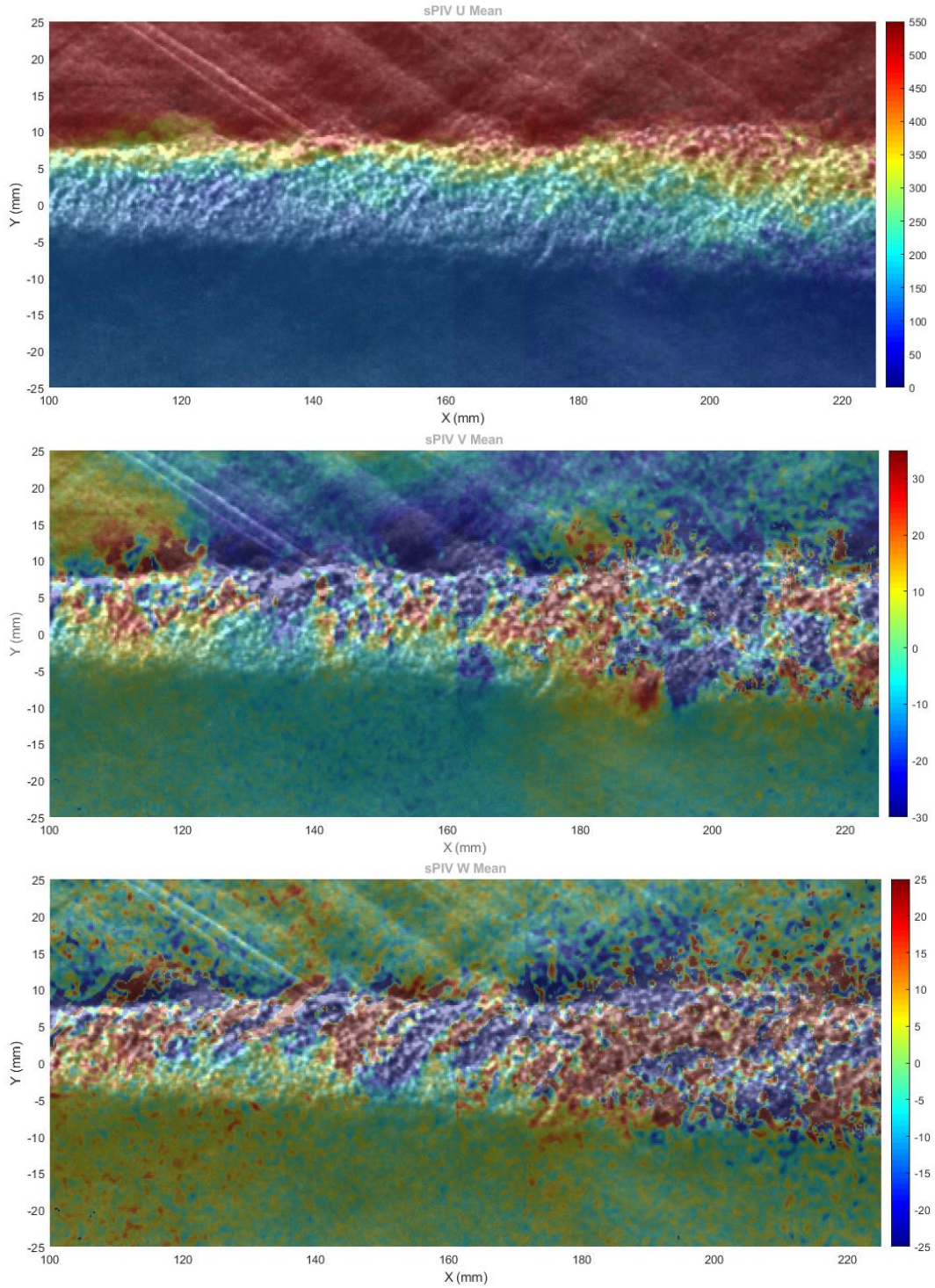

Figure 43. Instantaneous *u*-, *v*-, and *w*-component vector fields overlaid on schlieren stills in the Fully Developed Region

The mixing layer growth itself was examined and its characteristics measured from the mean velocity results. The ΔU shear layer thickness b and its centerline location y_0, were determined at each streamwise location along the shear layer, and from the thickness data, the shear layer growth rate $^{db}/_{dx}$ was calculated. The growth rate itself was determined using a least-squares fit curve and is plotted in Figure 44. From these results the normalized growth rate $^{db}/_{dx^*}$ was found by normalizing by the incompressible growth rate at the same velocity and density ratios of Papamoschou and Roshko described in Equation 2.[3] This normalized value is plotted against the convective Mach number in Figure 45; its value fits well within the values found by previously published work. With this said, however, the normalized growth rate is seen to be noticeably higher (about 22%) than the value found by Kim for the nearest similar M_c while using the same wind tunnel facility.

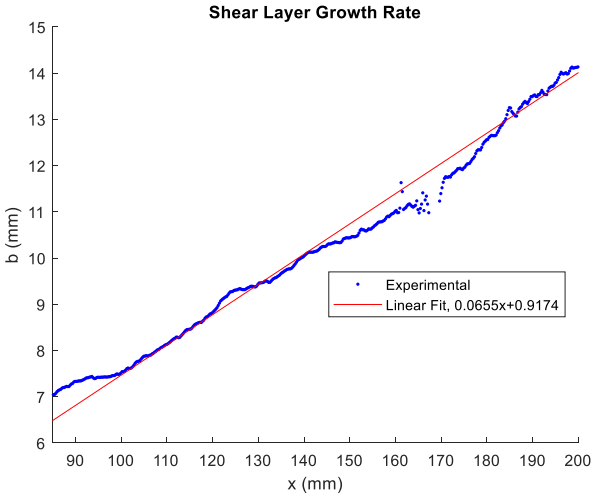

Figure 44. Shear layer growth rate

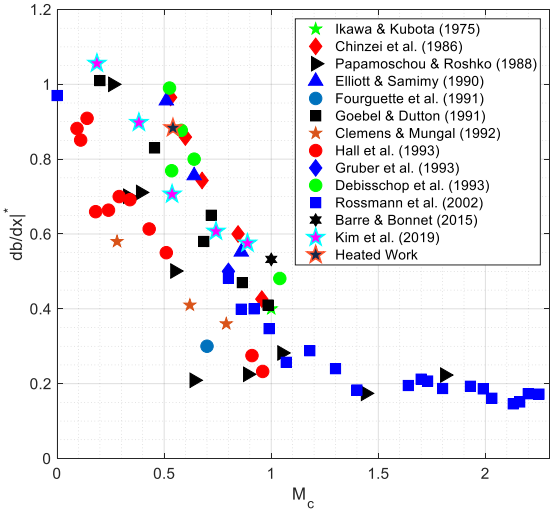

Figure 45. Normalized mixing layer growth rate versus M_c[39,40,3,41-46,10,6,13]

Analysis of self-similarity of the mean velocity profiles was also performed through the normalized velocity difference, $(U-U_2)/\Delta U$. Profiles of this quantity were made by plotting it against the normalized transverse coordinate η, which uses the local shear layer thickness and transverse centerline location y_0 in relation to the local mixing layer thickness b, and $\eta = (y-y_0)/b$. Plots showing these velocity profiles in the fully developed region of the flow are shown in Figure 46. A further plot showing the normalized velocity contours of $(U-U_2)/\Delta U$ is shown in Figure 47 plotted upon normalized η coordinates. Note that for the entire fully developed region, it remains flat and consistent throughout.

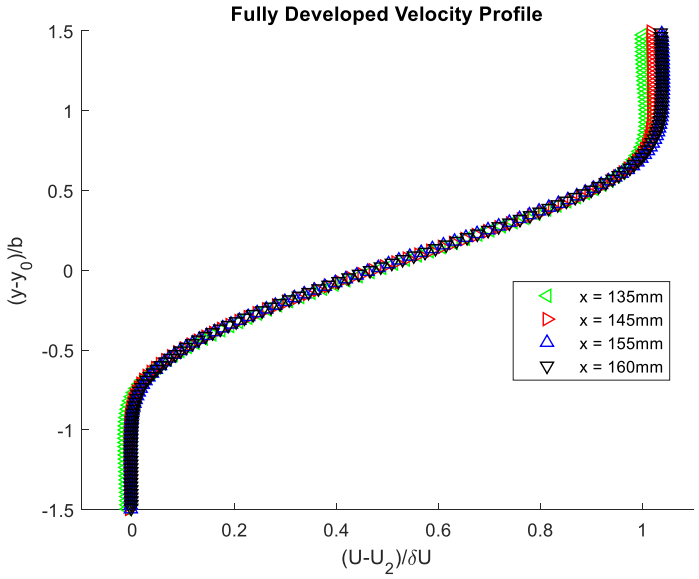

Figure 46. Fully Developed normalized mean velocity profiles

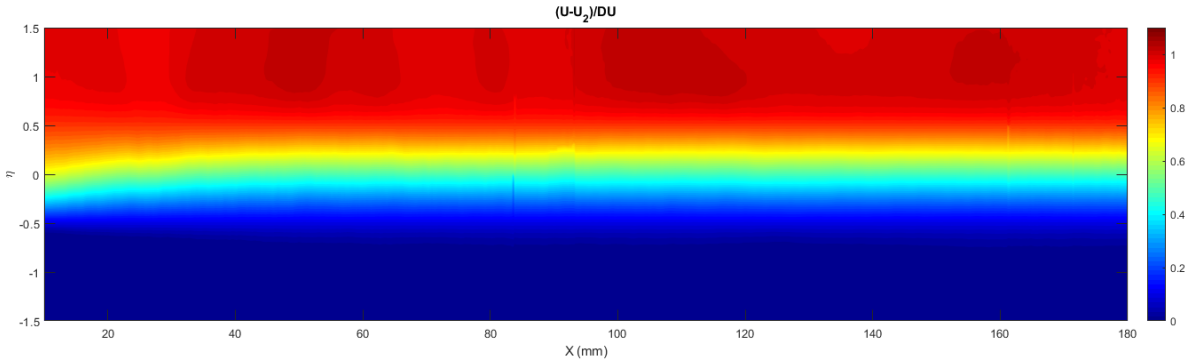

Figure 47. Normalized *U* contours in normalized transverse coordinates

Figure 46 in particular highlights how the mean velocity profiles collapse to the self-similar shape shown in the fully developed region; this is consistent with the findings of others for the shape of the self-similar mean velocity profile in the fully developed region of unheated mixing

layers, indicating that the stagnation temperature differential between the two streams does not have any major effect on the mean velocity profiles, normalized or non-normalized.

Fully developed turbulence within the mixing layer is critical; all statistical analyses will be drawn from this region. The self-similarity and linear growth of the mixing layer are two of the three criteria needed for the flow to be conventionally considered fully developed as per Mehta and Westphal's definition;[47] the third is self-similar Reynolds stress profiles, as will be discussed in the next section.

4.3.2 Statistical Results: Reynolds Stresses and Higher Moments

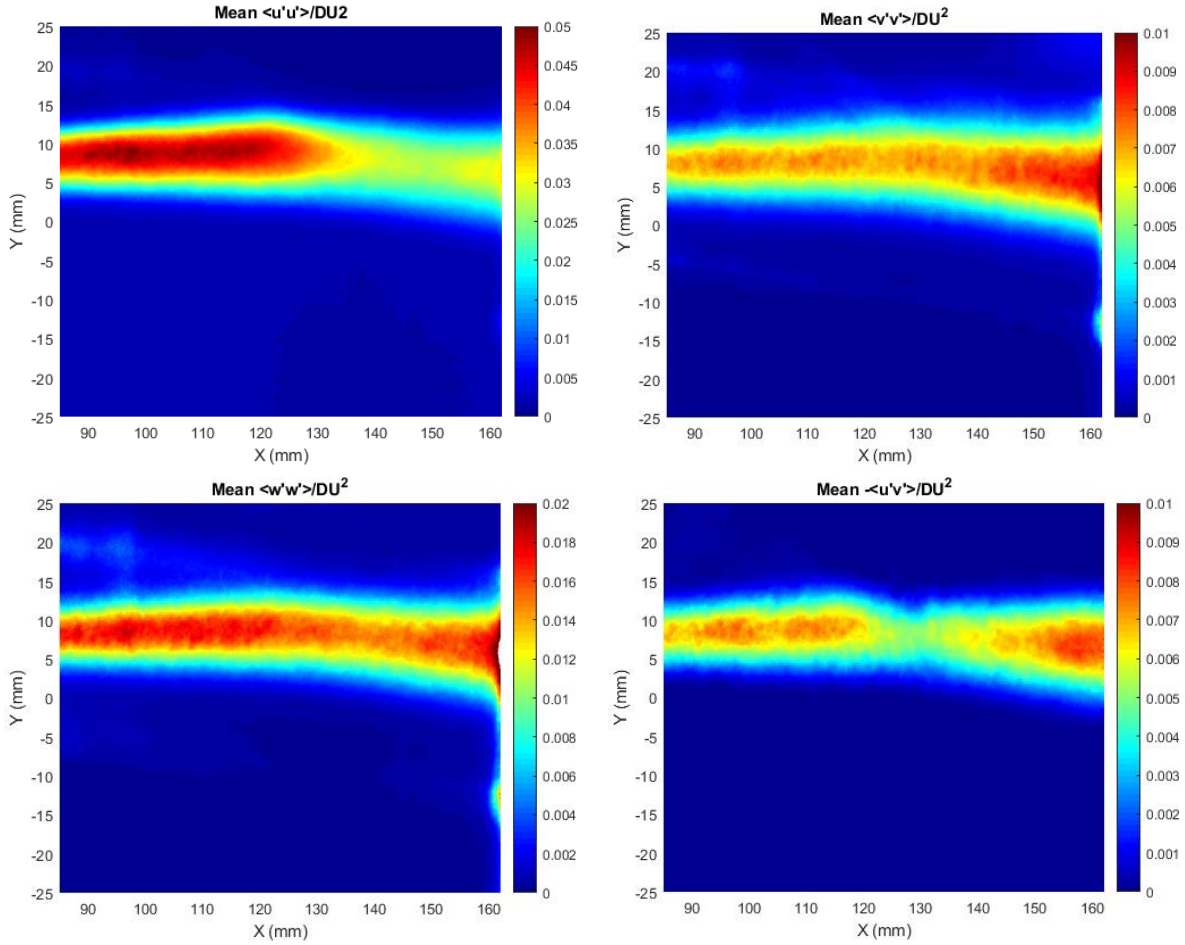

Figure 48. Contours of Reynolds stresses from the Fully Developed Region

Higher-order moments were also calculated using the complete ensembles of instantaneous velocity for each field of view. From these values, contours were plotted showing the Reynolds

stresses (i.e., second-order moments) for the region of interest; this is shown in Figure 48. From the contours, it appears that the stresses become self-similar around x = 145 mm. To confirm this, profiles were plotted at this point, and at nearby points prior to and after as well in order to show their convergence to self-similarity. These profiles, shown in Figure 49, confirm this finding.

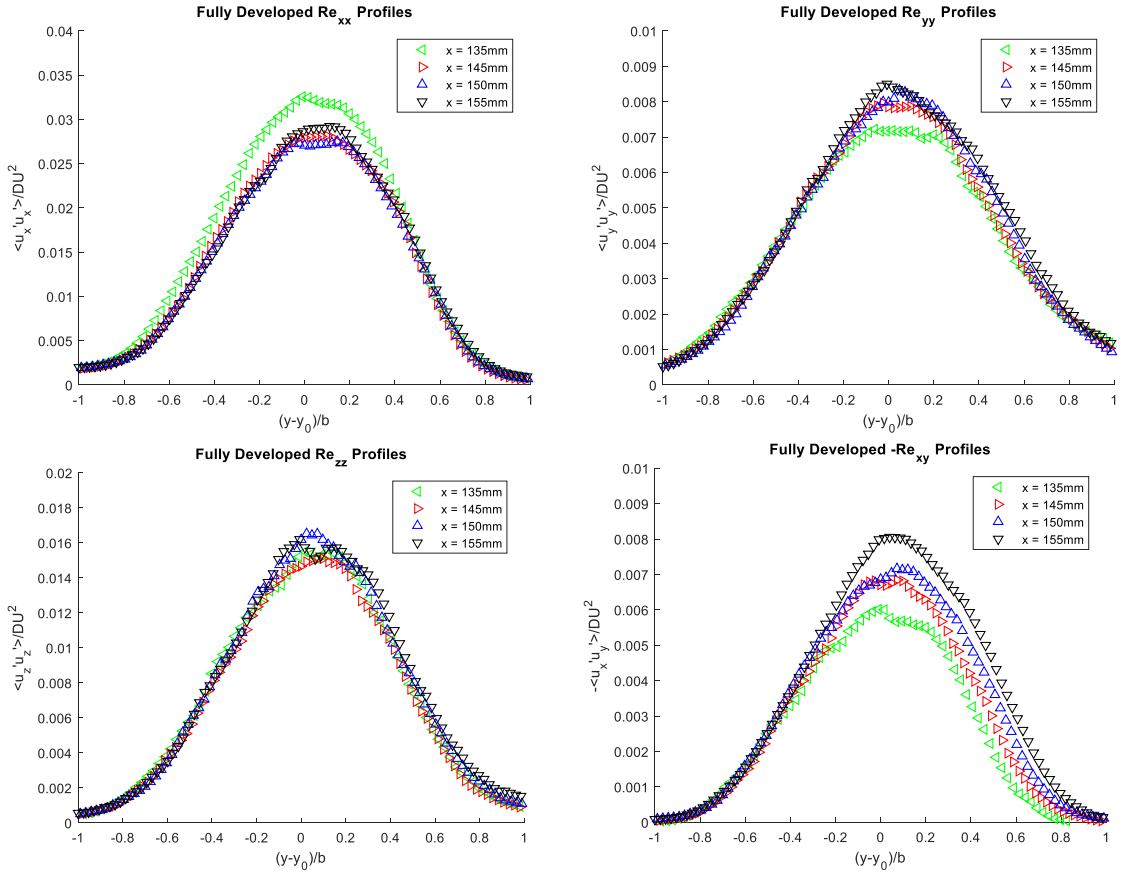

Figure 49. Reynolds stress profiles prior to and within the Fully Developed Region

Comparative profiles were also plotted showing the fully developed Reynolds stresses against those found by Kim for his similar operating conditions of Cases 3 and 4.[13,14] These profiles, shown in Figure 50, indicate a clear similarity between the three experiments in terms of the Reynolds stresses. The largest deviation found is in the Re_{yy} profiles, where the peak for the current heated mixing layer drops off below either of the peaks Kim found. The other deviation of note is in the Re_{zz} profile; the current work sees its peak level off in between the two Kim cases.

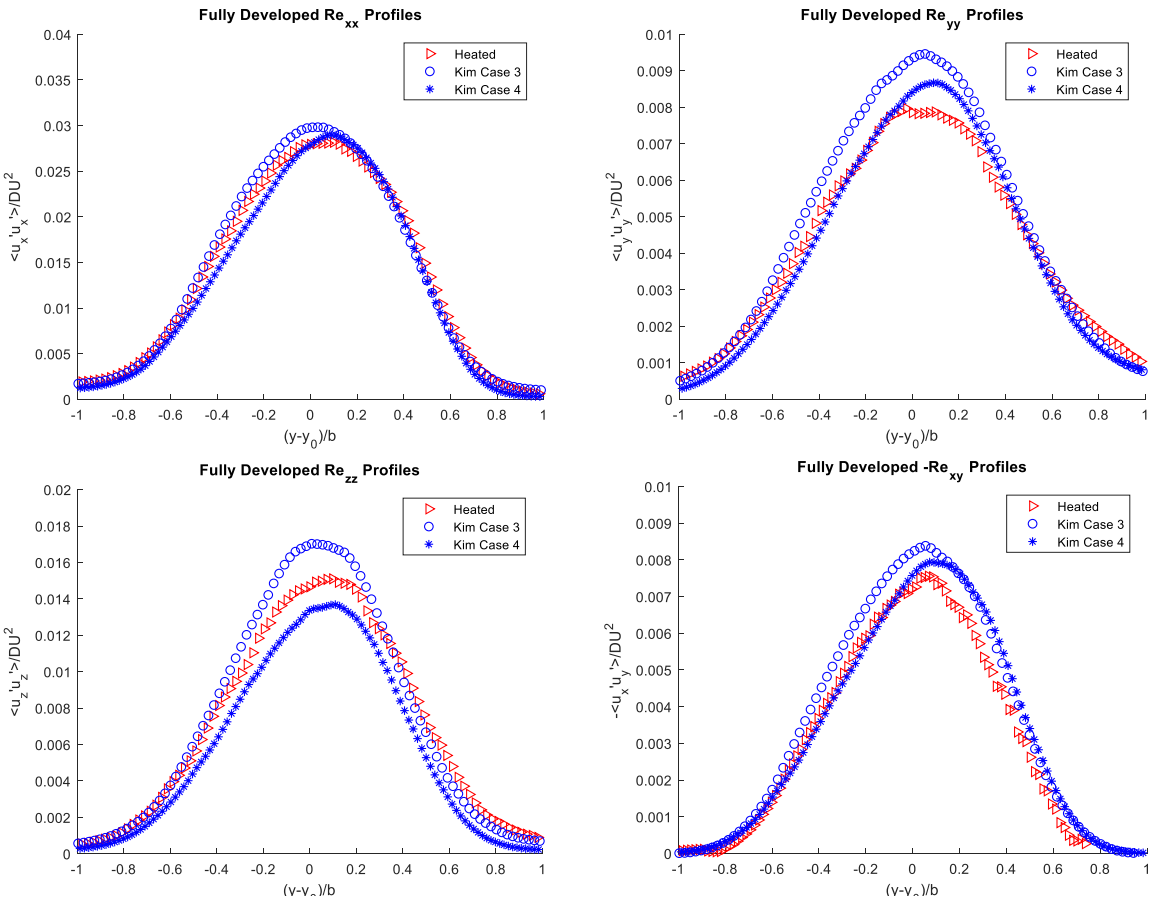

Figure 50. Comparison of Reynolds stresses in FDR with that of Cases 3 and 4 of Kim[13,14]

These findings indicate that there may be weak effects from the thermal gradient on the turbulent mixing characteristics, which is not unexpected. When considering the schlieren results, the strong braid structures indicative of three-dimensional mixing (and therefore instantaneous deviations from the mean) were more strongly present in this case than Kim's Case 4 but less so than visually observed in Kim's Case 3.[14] Likewise, the flatter mixing layer of the current case would indicate that variations would not have the same transverse distribution as the lower-M_c cases.

Further comparison of the peak Reynolds stresses in the fully developed region with respect to M_c is shown with data from the majority of previous, unheated, compressible mixing layer studies in Figure 51 on the next page. The peak values consistently match with previous trends

noted in the plots and are in particularly close agreement with the peak values from the previous unheated Case 3 mixing layer work of Kim at a very similar convective Mach number.

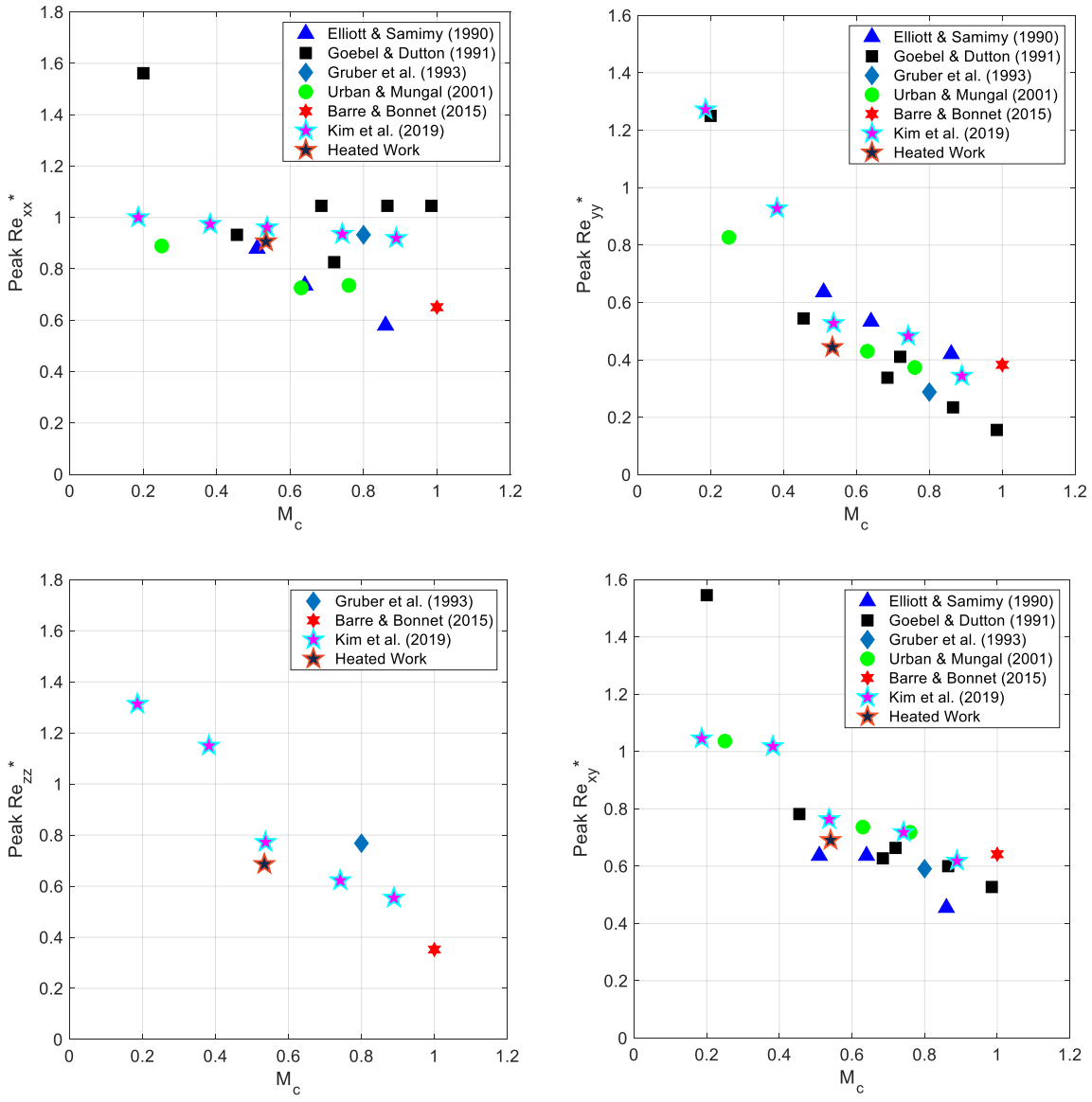

Figure 51. Peak Reynolds stress trends[41,5,45,48,6,13]

In addition to the Reynolds stresses, it is typical in the computational studies that this experiment is intended to support to report the anisotropy tensor and turbulent kinetic energy (TKE). The anisotropy tensor gives indications as to how much the fluctuations of each velocity component contribute to the turbulence energy budget; it is used in certain studies to close the

averaged turbulence equations. Below, Equation (5) gives the equation for the Reynolds stress anisotropy tensor

$$c_{ij} = \frac{\overline{u_i' u_j'}}{2k} - \frac{\delta_{ij}}{3} \tag{5}$$

where c_{ij} is the anisotropy tensor, k is the turbulent kinetic energy, and δ_{ij} the Kronecker delta. Profiles of both anisotropy and the TKE within the fully developed region are plotted in Figure 52. The anisotropy tensor, plotted in normalized coordinates in the center of the mixing layer, -0.5 < η < 0.5, shows fairly constant values for each component through the fully developed region of the shear layer. In the same vein, the TKE profiles show self-similarity in the fully developed region as well as smooth Gaussian-like intensity distributions across the mixing layer. Both results are additional and sensitive indications that the flow has become fully developed at this point.

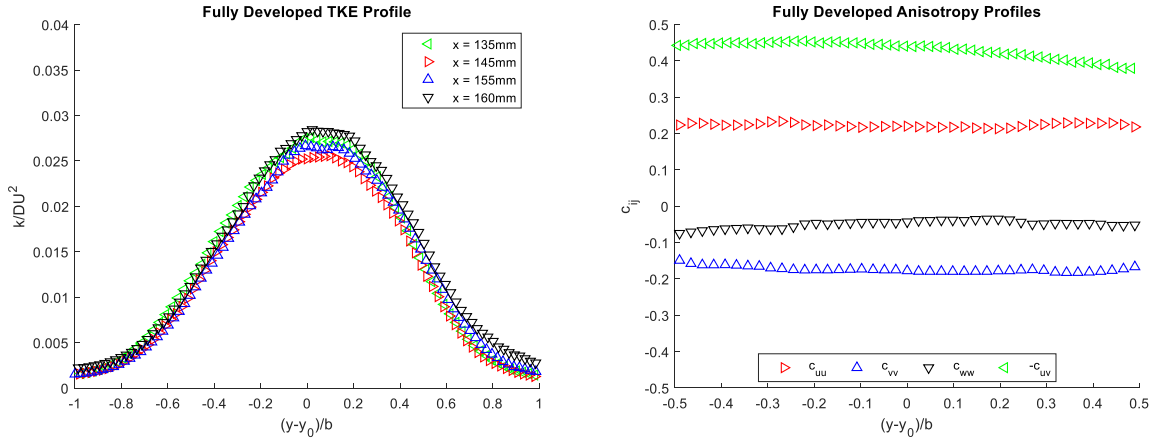

Figure 52. Fully Developed Region TKE and anisotropy profiles

With the large ensemble sizes available, it was also possible to compute triple products and fourth-order moments from the datasets. These higher-order statistical analyses give supporting insight into the fully developed region of the flow. Triple products are useful especially in computational studies that aim to study and model the Reynolds stress transport within the mixing layer. Normalized triple product similarity profiles in the fully developed region are plotted for the

u', *v'*, and *w'* components in Figure 53 and Figure 54 on the following page. These all are essentially identical to those found by Kim in his comparable cases.[14]

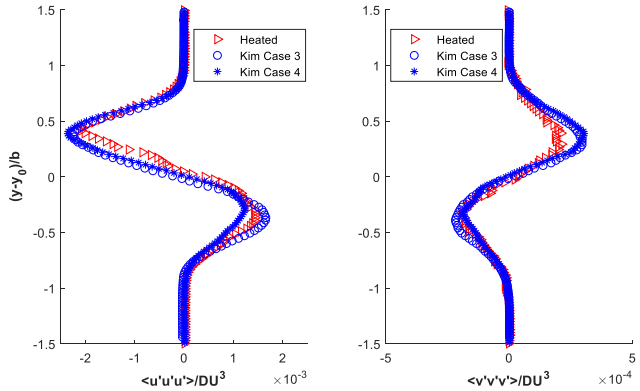

Figure 53. Normalized triple products compared with those of Kim[13,14]

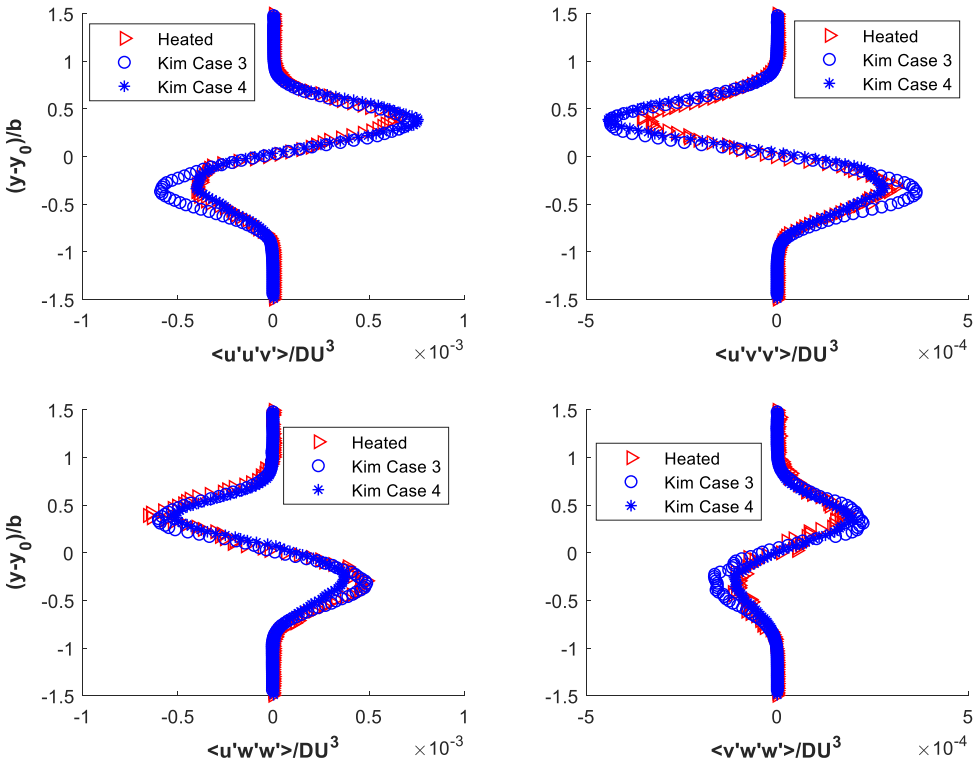

Figure 54. Comparison of normalized triple cross-products with Those of Kim[13,14]

When the trends of the Reynolds stress tensor, particularly the dominance of the Re_{xx} component and its anisotropy are considered in tandem with the distribution of the triple products

against those found by Kim, the conclusion can be drawn that the thermal gradient of the present case has only minor effects on the turbulence within the mixing layer. This, however, stands in contrast with the moderately increased normalized growth rate; this could be attributed to the heating of the mixing layer but requires further research to make such a determination.

4.3.3 SPIV Uncertainty

The uncertainty in the stereo-PIV measurements was determined for the entire ensemble of all instantaneous images at each location. This uncertainty represents the linchpin in the dataset. For it to be used in its intended purpose as a CFD validation-quality dataset, the uncertainty must be quantified. A 95% confidence interval of the measurements is given for all data. Each instantaneous uncertainty field was first calculated for all three velocity components from what have been previously identified as the primary uncertainty sources: equipment, particle lag, and processing. Mean velocity and Reynolds stress uncertainties are then determined from the instantaneous uncertainties with respect to the statistical sampling error. The approach used here is based upon a standard procedure used in the UIUC Gas Dynamics Lab group, which itself is based upon the work by Lazar et al. and later extended by Hortensius.[49,50]

The equipment error is primarily associated with the quality of the image scaling calibration in addition to the timing of the laser pulses. A pixel to real-space calibration, as discussed in Section 2.3.5, is determined using a dual-level calibration plate placed at a known location within the test section. This calibration plate, whose dimensions as well as marker size and spacing are known to the calibration routine in DaVis, has small uncertainty in its geometry. More important in the calibration is the image distortion due to this calibration, especially due to imperfect focusing of the camera lenses; minor effects are assumed due to aberrations of the calibration images themselves. Laser pulse timing error is due to the hardware limitations of the

delay pulse generator as well as accuracy of the laser system itself. Equipment error sources are all combined in a root-sum-square manner. Inputs to the equipment error terms are measured directly where possible, and all others are taken from the manufacturers' specifications.

The particle lag error, the difference in the measured particle velocity from the true fluid velocity, is inherent to any particle-based measurement method due to the myriad of forces acting on the individual particles (e.g. shocks, drag, gravity, buoyancy effects, etc.). For this case, all effects may be neglected with the exception of the Stokesian drag on the particles. A slip velocity due to the drag force that differs from the fluid velocity occurs, and may be calculated using a standard aerodynamic drag relation. Further assumptions are applied for the calculation of the drag force, as the lack of time-resolved data means that the particle acceleration is only able to be calculated from the spatial velocity field. To determine the drag coefficient C_d, Stokes' assumption $C_d = 24/Re_p$ is used as the initial value in an iterative scheme to find a value that is more accurate for Re_p that are not small. Details about this process can be found in Hortensius.[46]

The third, and final, instantaneous error source considered is the processing error. This processing error is directly calculated in the DaVis software as it processes the instantaneous velocity fields. The method that DaVis uses to determine each field's processing uncertainty is a correlation-statistics approach described in Weineke (2015)[51]; it is the major difference in the present UIUC GDL approach from that of Lazar et al.[49]

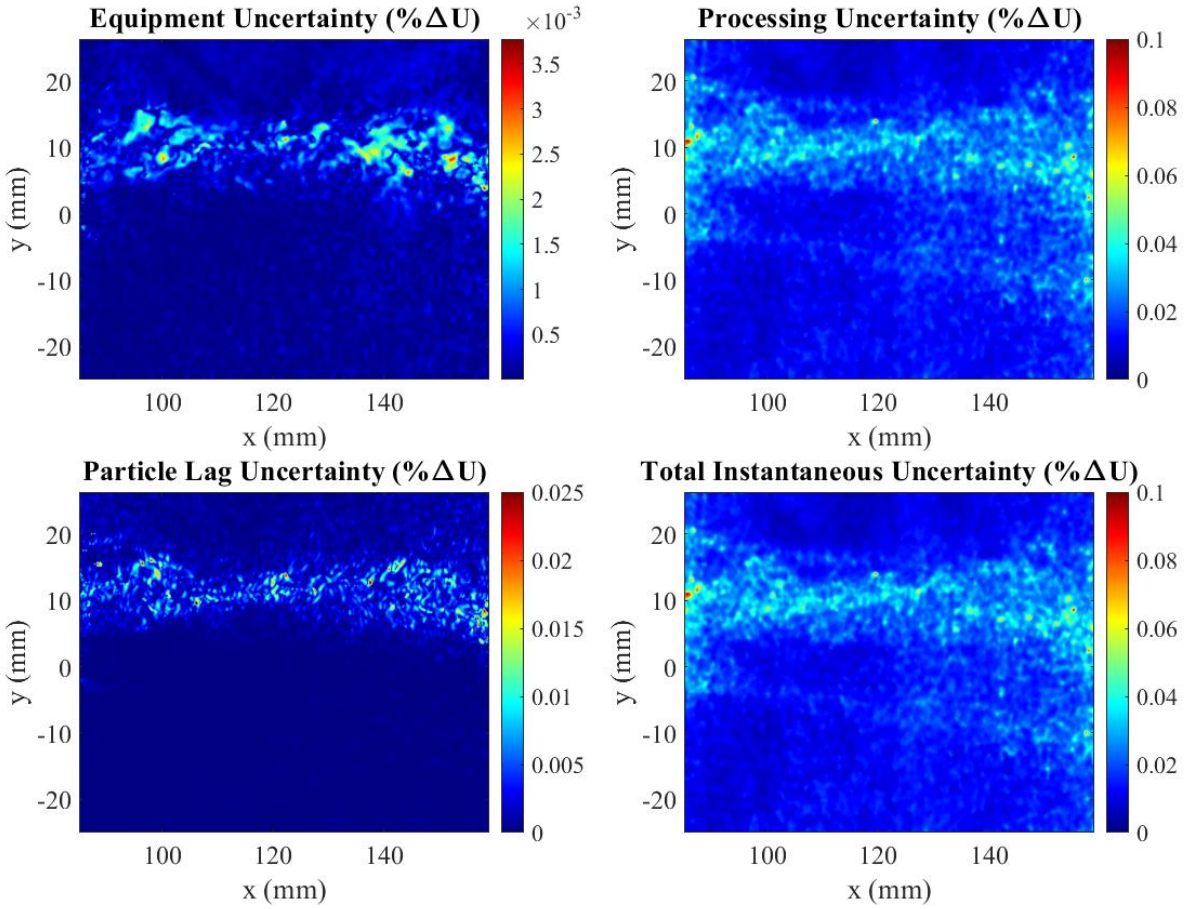

Figure 55. Instantaneous uncertainty for the *w*-component

Combination of the three instantaneous error sources is done in a root-sum-square sense to obtain the total instantaneous uncertainty for each velocity component at each measurement location. Examples of the instantaneous error for each source, as well as the combined error, are shown in Figure 55 for a typical *w*-component field. For this example, as well as for all the instantaneous fields, the processing error is the major contributor to the uncertainty and is found to be maximal in the mixing layer and at the edges of the field of view (due to laser sheet edge effects as well as camera lens distortion). This relative dominance is attributed to high-quality equipment and meticulous setup of the cameras, particles selected to have minimal slip with respect to the fluid, and oil/laser sheet effects on the image quality that are quantified in the processing error term.

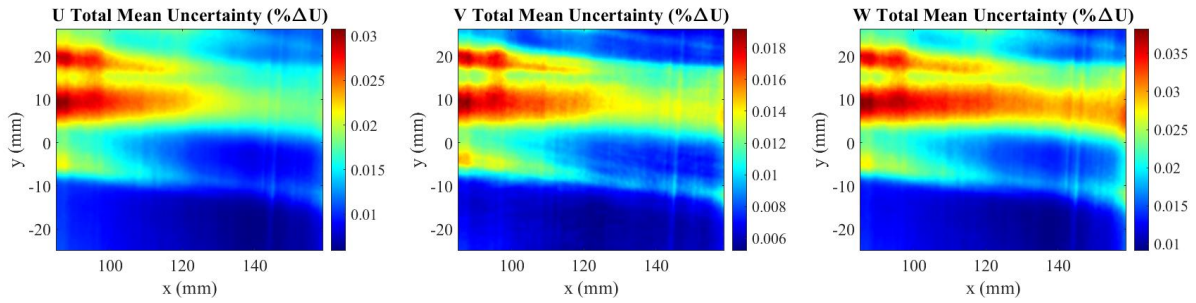

Figure 56. Mean uncertainty contours in FDR

Mean velocity uncertainty is calculated in a root-mean-square sense for the entire ensemble of each field of view. A statistical confidence term is added to this mean value, taken from the Student's t-test at 95% confidence where the finite ensemble size is used. These total mean velocity uncertainty fields normalized by ΔU are shown for each velocity component from the fully developed region in Figure 56.

From these, the *W*-component is seen to have the highest uncertainty value, although all three components have low uncertainty values for the measured fields of view, as they do not exceed more than 4% ΔU anywhere in the field of view. Here, it remains clear that the mixing layer is the locale of highest uncertainty in the measurements, although it stays well within acceptable bounds of uncertainty for the data's intended use for CFD validation.

CHAPTER 5: TEMPERATURE FIELD MEASUREMENTS IN A COMPRESSIBLE MIXING LAYER WITH A THERMAL GRADIENT

5.1 Filtered Rayleigh Scattering Implementation

5.1.1 Initial Parameters

This study utilizes Filtered Rayleigh Scattering (FRS) in order to measure the mean static temperature profiles in the heated shear layer. FRS was chosen as the primary thermometry method out of other possible approaches largely due to its ability to resolve temperature fields even in a dirty, particulate-laden environment. As a result of the PIV studies previously performed in the tunnel, as well as in this work, it was necessary to utilize a method that would not require a clean environment for measurement. The power of FRS, particularly its particle-filtering ability, is best illustrated in Figure 28 of Section 2.3.6. In this work, FRS was used to determine the static temperature, using previous mean measurements of pressure and velocity to assist processing.

These measurements of static temperature, as Section 1.2.1 discusses, are based on Rayleigh scattering from air molecules in the flow; to determine these quantitative measurements from the FRS signal, several parameters were separately experimentally determined. These preliminary parameters are intrinsic to the equation that determines the thermodynamic state of the molecule from the signal on each pixel in the camera sensor. The equations relating the behavior of the normalized filtered signal to the pressure and temperature of the air are defined in Section 1.2.1; they are summarized by Equations (3) and (8), which are restated below for clarity.

$$S = C\left[\int_{-\infty}^{\infty} R_{gas} t(f) df + \int_{-\infty}^{\infty} R_{bg} t(f) df\right] \tag{3}$$

$$\frac{S(f\prime)}{S_{ref}(f)} = \frac{T_{ref}}{T}\frac{P}{P_{ref}} \tag{8}$$

From these equations, there are four major values of interest: the combined scattered signal from the background R_{bg} which is assumed an individual constant for each field of view, the

transmission function of the iodine cell *t(f)*, the filtered reference flatfield signal $S_{ref}(f)$, and the flow's filtered signal *S(f')*. Respectively, these correspond to the background scattering picked up by the camera system, the iodine cell absorption for a given frequency, the scattering for an ambient reference state, and the scattering from the flow and thermodynamic state of the case of interest.

Given the four parameters of interest, three of the four (the background signal, reference signal, and flow signal) are obtained *in situ*; the reference flatfield signal is obtained prior to each run of the experiment and normalizes the corresponding flow-on signal. The background signal, since it may be assumed to be constant for each field of view, is considered a dark count value on the sensor as a subtracted per-pixel value from the flatfield and flow-on images. The flow signal is simply acquired by recording the images for the flow-on condition. The fourth parameter, the transmission of the iodine cell, is not obtained in situ and rather requires an external calibration across the operating frequency range of the laser.

5.1.2 Iodine Cell Calibration

Figure 57 on the next page gives the schematic of the optical set-up that measures the transmission profile *t(f)* of the iodine absorption filter. This schematic differs from the conceptual schematic for experimental data collection shown in Figure 22 of Section 2.3.6 by moving the iodine cell in front of the third photodiode (PD 3 in the schematic). In doing so, the transmission of the iodine cells may be determined by normalizing the response of the experimental cell photodiode by the signal received by the first photodiode (PD 1). It is also noted that absorptive neutral density filters were used to equilibrate the amount of laser power incoming on the three photodiodes prior to the inclusion of the iodine cells. This frequency trace had two purposes:

primarily, to fully define the transmission profile of the experimental and reference iodine cell; secondarily, to determine the operating frequency range of the laser.

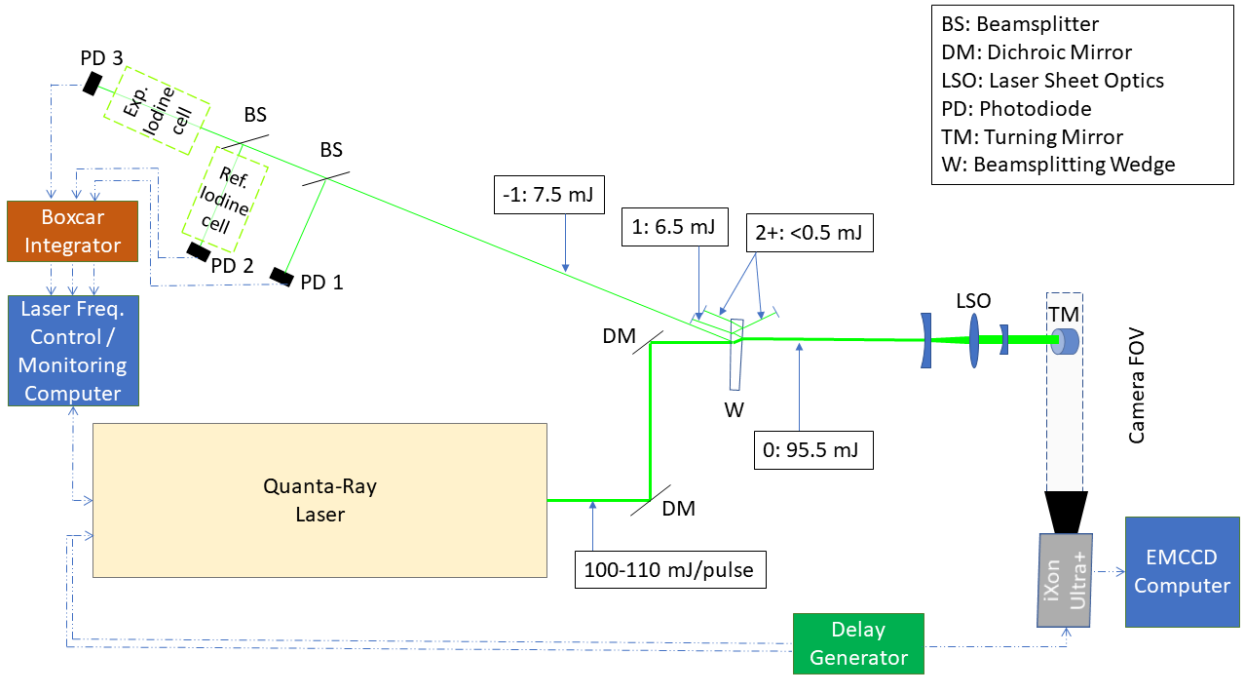

Figure 57. FRS conceptual schematic for iodine cell calibration

Once the profiles had been determined for both cells, they were compared to a computed profile using the model of Forkey et al. (1997), as shown in Figure 27 of Section 2.3.6.[35] The experimental iodine cell profile shows a good match to that of the computed model, especially along the absorption line at 18788.435 cm^{-1}. This absorption line has good absorption characteristics as well; it has a minimum transmission of less than 0.02% through the experimental cell. For the reference cell, there is a small amount transmitted, approximately 3.5%, since the number density, and therefore partial pressure of iodine, is less. While it may seem to be a downside, this actually turns out to be a benefit—it increases its sensitivity to how well the laser frequency matches to the desired value.

From the iodine cell transmission curve, it was determined that the operating range of the laser was from a wavenumber of 18789.318 to 18788.002 cm^{-1}, which included the fine absorption

line centered at 18788.435 cm^{-1}. This absorption line was chosen for two primary reasons: first, it resolved well in the reference cell as well, giving the ability to perform multiple-frequency observations if so desired; and second, it is wider and absorbs more than the other absorption line at 18788.74 cm^{-1}. Since the absorption profile is wider here, it is less susceptible to scatting from particles that experienced a Doppler shift relative to the laser frequency. This effect is illustrated in Figure 28 of Section 2.3.6, showing a comparison of a reference image taken at the two frequencies with otherwise similar settings. There are many more particles visible through the filter at the higher wavenumber; these decrease the quality of the instantaneous images and also present a risk in damaging the image sensor over time.

5.1.3 Imaging System and Laser Sheet Parameters

The imaging system and laser sheet were setup with the primary goal of measuring the temperature profile across the heated compressible shear layer and to obtain information about the development of the temperature profiles as the thermal shear layer grows downstream. An Andor iXon+ EMCCD camera was utilized with a seeded Spectra-Physics Quanta-Ray GCR-230 laser, due to the high quantum efficiency of the camera at the frequency doubled wavelength of the laser. This camera, with its quantum efficiency of over 95% at 532 nm, was a far superior option to less efficient cameras, even given its lower resolution (512x512 pixels).

Figure 58. Laser sheet burn for FRS

The Quanta-Ray laser was tuned to maximize the power output under full oscillator, with no amplifier applied. Timing between the laser and camera was controlled by an external delay generator. The laser sheet itself was collimated to remain as thin as possible and to keep the intensity of the laser sheet constant across the shear layer and freestreams. This gave a usable width across the laser sheet of approximately 14 mm with the lower intensity edges of the width discarded; the burn

paper image of Figure 58 on the previous page illustrates this energy distribution across the laser sheet. Because of space limitations, all measurements made beyond 85 mm in the *x*- direction required an additional "periscoping" assembly of two mirrors, moving the laser sheet further down the test section. This proved to be a stable and highly flexible method of adjusting the position of the laser sheet for the downstream temperature measurements.

The camera itself was side-mounted to a Newport Optics linear stage, allowing it to be moved along the length of the test section at a constant distance, greatly reducing the time spent focusing the lens and also keeping the range of the field of view relatively constant between positions. The iodine filter was also mounted to a linear stage, allowing for minor adjustments to be made, reducing the effects of imperfections and inconsistencies through the filter. The camera sensor was cooled to -20°C to reduce noise; the camera sensor voltage was overclocked in order to reduce a vertical blind effect that occurred at the high framerate required of the system due to the high gain levels required to resolve the Rayleigh scattering signal.

5.1.4 Image Processing and Temperature Calculation

Below is a summary of the image collection process:

- For each field of view, a calibration image was taken using a LaVision calibration plate and physical calibration obtained using the DaVis software.
- Three sets of images were captured: a laser-off background (dark count) image, a laser-on flatfield (reference) image, and a flowfield image using the Andor SOLIS software.
    - The background and flatfield images were taken at ambient temperature and pressure and with no flow in the test section; the flowfield image was taken with the tunnel at its full operating condition.

    - These images were all taken at the same camera gain, exposure time, and aperture settings; one hundred image frames were averaged to form the background and flatfield, and twelve hundred frames were recorded for the flowfield images.
    - The flowfield images were taken in two sets of six hundred images each, in order to maximize the amount of time spent near the goal stagnation temperature condition of 495 K, as well as to stay within the RAM limitations of the imaging computer.
    - For all images, the conditions in the wind tunnel test section, primarily the stagnation temperatures of the two streams, were saved, as well as the laser BURT voltage for the shot (for more on BURT, refer to Section 2.3.6).
- The two flowfield image sets were saved as 16-bit Tagged Image File Format (TIFF) images as well as in the Princeton Instruments SPE image file format.

Once the image data had been saved, it was transferred from the imaging computer to a secure cloud server. The images were then accessed by a custom MATLAB code that loaded in the SPE file, applied a physical calibration to the images, and sorted out images that were outside of the intensity range, indicating the laser frequency had unlocked. The images were then processed using the method below:

- The averaged background (dark count) image was subtracted from the averaged flatfield and each instantaneous flowfield image.
- The mean of the instantaneous flowfield images was calculated. The portion of the image that was not illuminated by the laser sheet was used to determine an average intensity value. This was then compared against the average value of the same non-illuminated area in the flatfield image outside of the laser sheet range. This difference was applied to the flatfield image to

correct for disparities between the shots (particularly variations in camera gain or laser power over the course of the run).

- A Rayleigh signal library is calculated for the run. This library is calculated based on the target locked frequency of the laser, known velocity range from the stereo-PIV results, and static pressure measurements. It also utilizes the stagnation temperatures of the facility to determine the upper and lower bounds of the temperature range: fifty degrees K above/below the maximum/minimum static temperature in the freestreams. This library is ultimately a two-dimensional table giving the signal as a function of temperature and velocity, as discussed in Section 1.2.1. A sample signal library is shown in Figure 3.

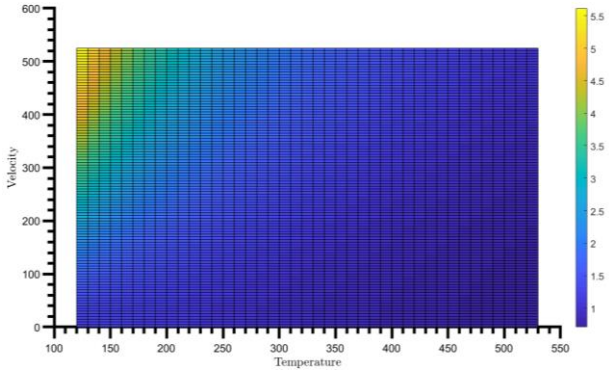

Figure 59. Example FRS signal intensity library

- Using the average stagnation temperature in the primary and secondary streams, as well as the average velocity from the PIV data, the average FRS signal for the freestreams was determined from the signal library using the Tenti formulation[20] and assuming an air composition of 79% nitrogen and 21% oxygen. This signal was then compared to the library signal and normalized image signal; this comparison formed a linear fit to adjust the signal library to fit the range of values found in the image.
- The temperature at each pixel in the normalized flowfield image is then calculated:
    - The velocity for the pixel is determined using the physical calibration of the image and the velocity data from the stereo-PIV.

- The temperature is then determined by using the MATLAB find function, to find the index within the signal library row of that pixel's velocity that is the nearest match between the adjusted signal library value and the intensity of the pixel in the image.

- The entire temperature field is plotted, as well as a temperature trace for the mean value at each transverse location. The thickness and height of the thermal mixing layer is then computed from the location of the two thermal freestreams using the 90% ΔT definition (similar to the method used for calculating the velocity shear layer thickness discussed in Section 3.3.2).

5.1.5 Challenges with FRS

The primary challenges implementing the Filtered Rayleigh Scattering measurements stemmed from the lack of a true background correction. The background correction, which came in two parts in this work (changing the flatfield non-signal area to have the same value as the flowfield, and scaling the signal values in the freestreams), were alternatives from the methods typically seen in the literature[18,22-33,48] where the background is calculated from a vacuum or very low-density environment with the laser sheet present in the image. However, physical limitations related to the mixing layer facility itself meant that the Rayleigh signal background could not be determined in this manner or in a similar one. The background images in this work are correcting for the background signal from the room lights and associated with the camera not the effects of the entire imaging system and laser sheet. Compounding this difficulty, the vibrational environment encountered by the laser while running the wind tunnel led to unlock from the desired frequency far more often than in normal operation. While these vibrations did not affect the laser sheet itself, it did of course reduce the number of useable images in a run and therefore decreased the ensemble size by an appreciable amount. Furthermore, this behavior precluded the multiple-

frequency approach to taking the data, because the frequency variations are random and would have greatly limited the number of usable images per frequency.

5.2 FRS Temperature Results

5.2.1 Mean Temperature Trace Results

Mean temperature profiles were calculated for four streamwise positions, at x = 33, 89, 128, and 182 mm, approximately evenly spaced through the test section. In particular, the final two positions were intended to verify the FRS temperature results and provide a temperature trace within the portion of the mixing layer that is fully developed in turbulence. These raw temperature profiles are shown in Figure 60; they can be seen to exhibit a nearly linear gradient in temperature across the shear layer, with the exception of the noisier trace taken at x = 89 mm. As with the temperature probe traverses, the temperature profiles are best visualized in a normalized form between the freestream static temperatures, and plotted on an η-coordinate calculated using the previously discussed 10% ΔT formulation. These normalized profiles may be viewed in Figure 61. From the normalizes profiles it is quite clear that after a streamwise distance of 89 mm the profiles collapse upon one another. This corresponds with the behavior

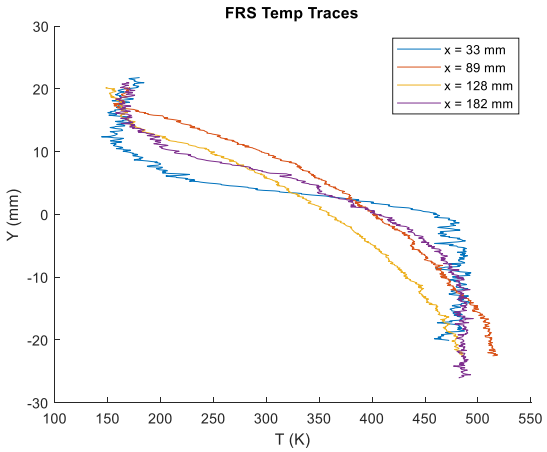

Figure 60. FRS mean static temperature profiles

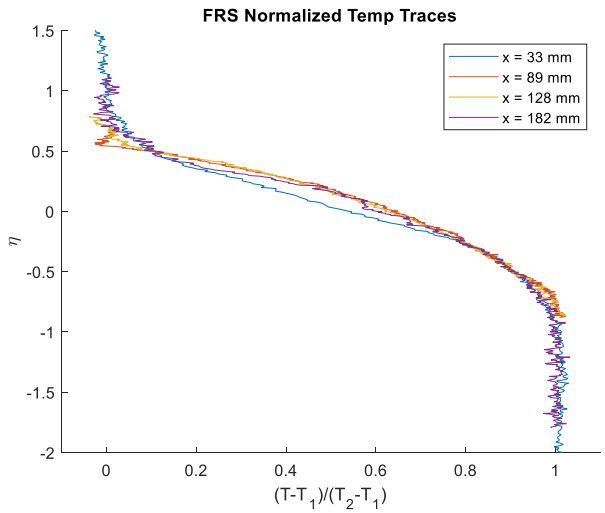

Figure 61. FRS normalized static temperature profiles

of the normalized traces from the temperature probe traverses. Furthermore, it should be noted that the thermally fully developed region begins even sooner than indicated from the temperature probe data. While there is noise in the data, self-similarity is extremely strong evidence to show that the flow is thermally developed by a streamwise position of at least 89 mm.

However, the overall quality of the temperature profiles appears to be poorer than what is possible when compared to the literature. Although the temperature profiles are found to be consistent with the probe measurements, due to the heavy assumptions required and difficulties associated with the experimental setup, the results are more qualitative than quantitative. The large amount of noise in the thermal freestreams is indicative that further work is necessary to improve the results, particularly to resolve the instantaneous profiles not shown here, due to their high level of noise which is smoothed out by the averaging process.

5.2.2 FRS Temperature Fields

Additional information may be gleaned from the two-dimensional temperature fields measured using FRS. The noise inherent to the measurement can have a major effect, and is most noticeable in the initial temperature field obtained between x = 29 to 35 mm, shown in Figure 62.

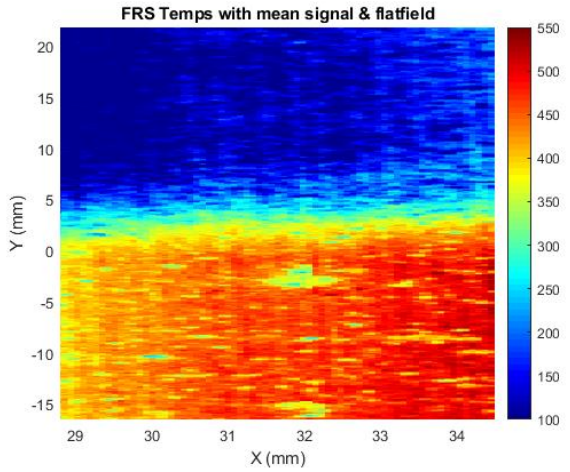

Figure 62. Early FRS temperature field result

The cold spots as calculated from the processing are caused by particles that were not fully filtered by the iodine cell. From this regard it is clear that more preprocessing is necessary in order to better filter out such “hot spots” in the flowfield image stack. The temperature fields with a more stringent filter may be seen in Figure 63; they still show the effects of other noise sources in a few of the images. Even though the more aggressively

preprocessed temperature fields do not suffer from particle noise in the freestreams, their overall quality may still be improved from a more sophisticated method, such as the one proposed by

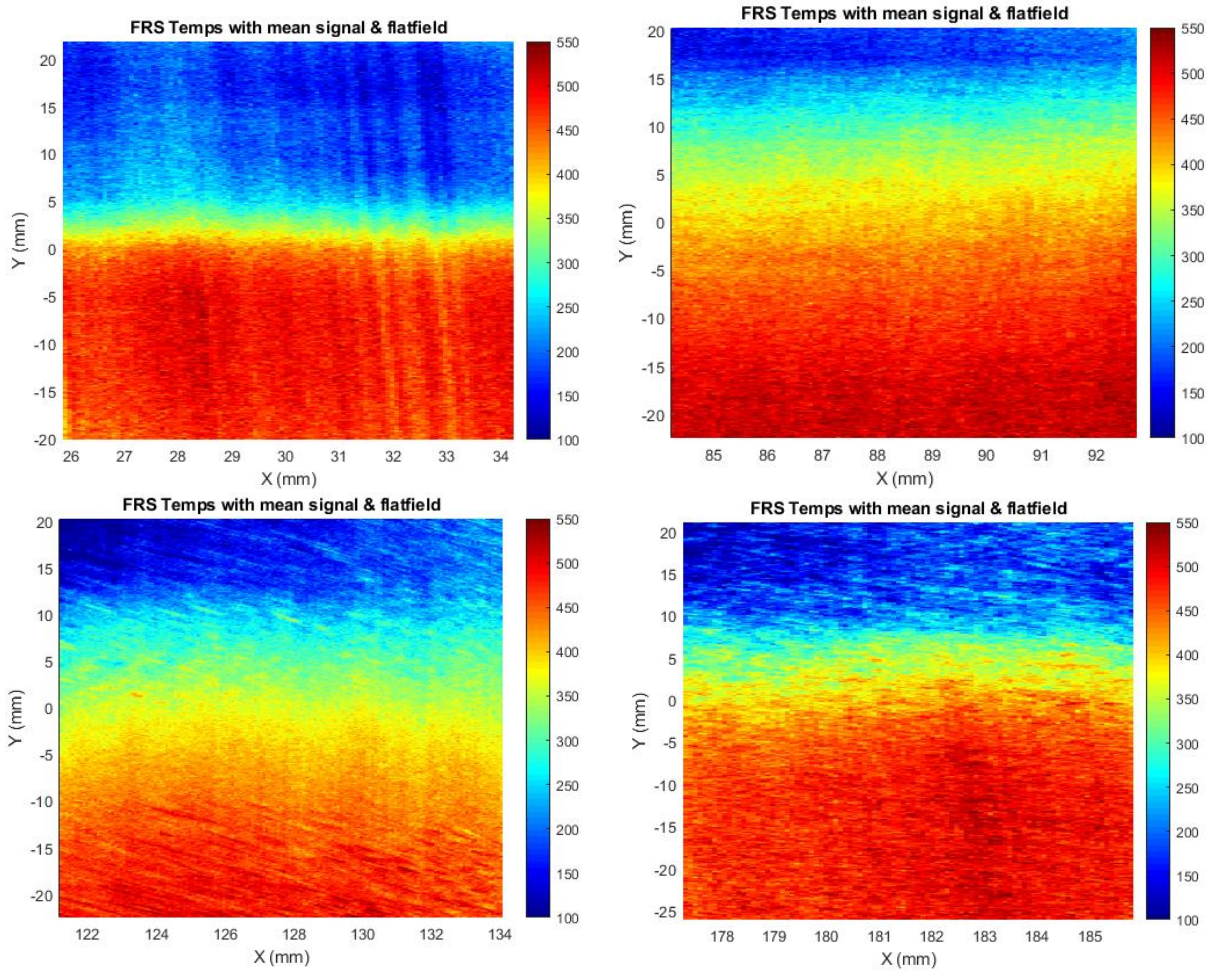

Figure 63. Filtered Rayleigh Scattering temperature field results

McManus and Sutton using a standard deviation rule to find particle-laden images.[33]

Even as the temperature fields have the aforementioned shortcomings, they still show the general behavior of the thermal shear layer at the different streamwise measurement areas along the test section. The fields represent a temperature distribution that logically makes sense across the shear layer and into the freestreams; however, there is not the expected consistency in the mean locations of the shear layer boundaries with the freestreams. This shortcoming is further illustrated by plotting the shear layer growth rate as computed from the traces and mean fields in Figure 64

on the next page. From the temperature fields, a general widening trend across the mixing layer seems to occur from field-to-field; however, it is fairly difficult to discern individually in each field as a result of the noise in resolving the shear layer itself and general uncertainty with respect to the data. This lack of a distinct growth rate trend across each temperature field, and general lack of a consistently linear growth rate from field to field, indicates that the noise across the shear layer is a major area for improvement. However, the mean trend from each field shows that the growth rate can be generally trusted, especially once a line of best fit is plotted. In addition to this weakness, the unevenness of the thermal shear layer as determined through the FRS fields is far more likely to be a negative effect of the experimental setup, rather than a physical one. The diagonal hot/cold lines in the fields are further evidence to this end; they are attributed to inconsistencies in the laser shots, and possibly even minor laser sheet blockages on the bottom incoming window, due to accumulation of oil or other detritus during a test run. Overall, these limitations are not considered to be so much as to wash out the new information given by the mean FRS results, but it is still recommended to utilize the mean TAT probe-trace results prior to the FRS fields.

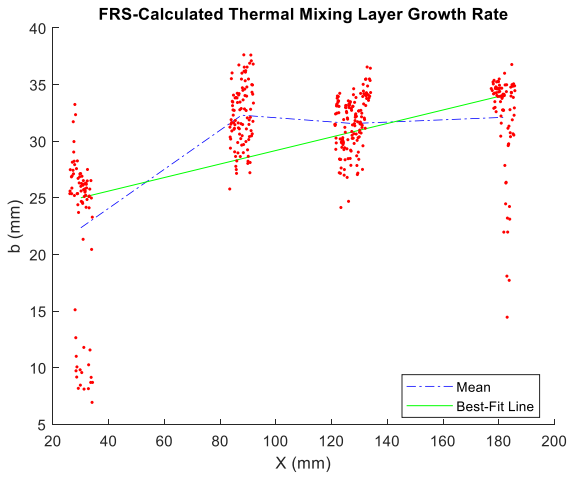

Figure 64. Thermal mixing layer growth rate trend

CHAPTER 6: CONCLUSION

6.1 Summary of Work and Concluding Remarks

This thesis serves to investigate a compressible shear layer with a thermal gradient between the two streams with the goal of obtaining CFD-validation quality temperature and velocity data. The dual-stream wind tunnel facility was modified from its original design in order to incorporate the addition of a heater capable of providing the requisite stagnation temperature in one of the two streams. Supporting measurements in order to qualitatively analyze the flow, including high-speed schlieren videos and static pressure measurements along the sidewall of the tunnel; these provided insights into the shear layer's development. Stereo-PIV results found that the statistical measurements in the compressible mixing layer, including that of the mean velocity profiles, entire Reynolds stress tensor including its anisotropy trends, and triple products, proved consistent with the literature, even though previous works were acquired using ambient stagnation temperature environments for both streams. At the same time, the stereo-PIV indicated a higher shear layer growth rate than for recent experiments at similar convective Mach numbers in the same facility. Stagnation temperature probe profiles were obtained at certain streamwise locations, including in the fully turbulently developed region, indicating the thermal mixing layer may become fully developed well before the turbulent mixing layer. Finally, Filtered Rayleigh Scattering was utilized to successfully capture the temperature fields at specific locations in the mixing layer as well as the freestreams, a first for non-reacting compressible shear layers with a stagnation temperature difference between the two streams. While the FRS temperature field results indicate that there may remain areas for improvement in the temperature determination, it is data of high enough quality to provide a starting point for future research in the field.

6.2 Future Work and Recommendations

This work, while certainly a strong starting point for the direct investigation of temperature mixing in shear layers, remains just that: a starting point. The velocity measurements from the stereo-PIV experiments represent a high-resolution, low-uncertainty dataset that certainly can be of immediate use in CFD validation. Furthermore, the schlieren visualizations, especially the high-speed movies, are quite useful for qualitatively examining the shear layer and provide an underpinning for deeper investigation of the current work. However, both the temperature data from both the Filtered Rayleigh Scattering as well as the total temperature probe traverses appear to need further refinement and examination.

While the mean accuracy of the FRS profiles appears to be correct, the fields show that continued work on their processing could provide better results—and quite possibly deeper insights than just the qualitative trend of the mean transverse temperature profile. On the other hand, the uncertainty of the total temperature probe traverses is quite low—however, they were only conducted for a few streamwise positions, and therefore are unable to offer the kind of spatial resolution needed to determine where the flow becomes fully thermally developed. While the Filtered Rayleigh Scattering data has the capability of a much larger field of view and therefore a much larger field of temperature results, it is still fairly limited by both the laser power density in the sheet as well as the camera resolution limitations. An improved experimental setup, especially FRS results performed at a higher laser power spread over a longer (in streamwise length) laser sheet (therefore corresponding to a similar power density in the sheet as the current experiments), would greatly improve the *utility* of the FRS approach. In doing so, analyses similar to those employed on the mean PIV data would be within reach. The other current limitation of both the FRS and temperature probe data is the lack of instantaneous temperature fields or even profiles.

While sustained analysis of the FRS data may put instantaneous results within reach, the temperature probe traverses by their nature are unable to take such instantaneous data. This limitation of the temperature probe indicates that moving forward, Filtered Rayleigh Scattering should be further developed with a focus on reducing uncertainty and experimental difficulties so that it can be reliably utilized for temperature measurements.

For future measurements of the shear layer, the most compelling result is computing the density from the FRS measurements to then determine the mass entrainment of the shear layer itself. While density is possible to be computed from merely the temperature and then using the static pressures in the flow (which have been shown to be essentially equal to one another and constant throughout) with the ideal gas law, an analysis of that type should likely utilize the multiple-property approach of FRS, be it FARRS or otherwise. Even if the processing is simplified by using an alternate method of computing the velocity, such as from PIV, it still would provide a marked improvement over using the single-property measurement approach. These density measurements could then be combined with an entrainment analysis similar to that employed by Kim[14]; his work specifically lacked such information and would have been greatly assisted in that respect. Of course, in order to use a multiple-property approach, refinements to the laser frequency control scheme are necessary, such that the laser frequency for each shot is well-known and not as affected by the highly vibrational environment induced by running the shear layer facility. The solution of these issues, then, is the clear next step in improving the understanding of a heated compressible shear layer.

REFERENCES

[1]Brown, G.L. and Roshko, A., "On Density Effects and Large Structures in Turbulent Mixing Layers," *Journal of Fluid Mechanics*, Vol. 64, 1974, pp. 774-816.

[2]Bogdonoff, D.W., "Compressibility Effects in Turbulent Shear Layers," *AIAA Journal*, Vol. 21, No. 6, 1983, pp. 926–927.

[3]Papamoschou, D. and Roshko, A., "The compressible turbulent shear layer: an experimental study," *Journal of Fluid Mechanics*, Vol. 197, 1988, pp. 453–477.

[4]Sabin, C. M., "An analytical and experimental study of the plane, incompressible, turbulent free-shear layer with arbitrary velocity ratio and pressure gradient," *Trans. A.S.M.E.*, D 87, No. 421, 1965.

[5]Goebel, S. G. and Dutton, J. C., "Experimental Study of Compressible Turbulent Mixing Layers," *AIAA Journal*, Vol. 29, No. 4, 1991, pp. 538–546.

[6]Barre, S. and Bonnet, J. P., "Detailed experimental study of a highly compressible supersonic turbulent plane mixing layer and comparison with most recent DNS results: "Towards an accurate description of compressibility effects in supersonic free shear flows," *International Journal of Heat and Fluid Flow*, Vol. 51, 2015, pp. 324–334.

[7]Kim, K. U., Elliott, G. S., and Dutton, J.C., "A Three-Dimensional Experimental Study of Compressibility Effects on Turbulent Free Shear Layers," *2018 Fluid Dynamics Conference*, AIAA Paper 2018-3864, 25-29 June 2018.

[8]Ghodke, C., Choi, J., Srinivasan, S., Menon, S., "Large Eddy Simulation of Supersonic Combustion in a Cavity-Strut Flameholder", *49th AIAA Aerospace Sciences Meeting*, AIAA Paper 2011-0323, 4–7 Jan. 2011.

[9]Grady, N. R., Pitz, R. W., Carter, C. D., Hsu, K., Ghodke, C., Menon, S., "Supersonic Flow over a Ramped-Wall Cavity Flame Holder with an Upstream Strut," *Journal of Propulsion and Power*, Vol. 28, 2012, pp. 982-990.

[10]Rossmann, T., Mungal, M. G., and Hanson, R. K., "Evolution and growth of large-scale structures in high compressibility mixing layers," *Journal of Turbulence*, Vol. 3, No. 9, 2002, pp. 1–18.

[11]Abraham, J., Magi, V., "Exploring Velocity and Density Ratio Effects in a Mixing Layer Using DNS," *International Journal of Computational Fluid Dynamics*, Vol. 8, No. 2, 1999, pp. 147-151.

[12]Zhang, Y., Wang, B., Zhang, H., Xue, S., "Mixing enhancement of compressible planar mixing layer impinged by oblique shock waves," *Journal of Propulsion and Power*, Vol. 31, No. 1, 2015, pp. 156-169.

[13]Kim, K. U., Elliott, G. S., and Dutton, J.C., "Three Dimensional Experimental Study of Compressibility Effects on Turbulent Free Shear Layers," *AIAA Journal*, Vol. 58, No. 1, 2020, pp. 133-147.

[14]Kim, K., "Compressibility Effects on Large-Scale Structures and Entrainment in Turbulent Planar Mixing Layers," Ph.D. Thesis, Dept. of Aerospace Engineering, University of Illinois, Urbana, IL, 2020.

[15]Kim, K. U., Elliott, G. S., and Dutton, J.C., "Compressibility Effects on Large Structures and Entrainment Length Scales in Mixing Layers," *AIAA Journal*, Vol. 58, No. 12, 2020, pp. 5168-5182.

[16]Freund, J. B., Lele, S. K., and Moin, P., "Compressibility effects in a turbulent annular mixing layer. Part 1. Turbulence and growth rate," *Journal of Fluid Mechanics*, Vol. 421, 2000, pp. 229–267.

[17]Pantano, C. and Sarkar, S., "A study of compressibility effects in the high-speed turbulent shear layer using direct simulation," *Journal of Fluid Mechanics*, Vol. 451, 2002, pp. 329–371.

[18]Forkey, J. N., Finkelstein, N.D., Lempert, W.R., Miles, R.B., "Demonstration and Characterization of Filtered Rayleigh Scattering for Planar Velocity Measurements," *AIAA Journal*, Vol. 34, No. 3, 1996, pp. 442-448.

[19]Shardanand and Rao, A.D.P., "Absolute Rayleigh Scattering cross sections of gases and freons of stratospheric interest in the visible and ultraviolet regions," NASA TN-D-8442, March 1977.

[20]Tenti, G., Boley, C. D., and Desai, R. C., "On the Kinetic Model Description of Rayleigh-Brillouin Scattering from Molecular Gasses," *Canadian Journal of Physics*, Vol. 52, No. 4, 1974, pp. 285-290.

[21]Yen, Y., and Cummins, H. Z., "Localized Fluid Flow Measurements with an He-Ne Laser Spectrometer," *Applied Physics Letters*, Vol. 4, No. 10, 1964, pp. 176-178.

[22]Elliott, G. S., Samimy, M., and Arnette, S. A., "A Study of Compressible Mixing Layers Using Filtered Rayleigh Scattering," *30th Aerospace Sciences Meeting and Exhibit*, AIAA Paper 92-0175, Jan. 1992.

[23]Miles, R. B., Forkey, J. N., and Lempert, W. R., "Filtered Rayleigh Scattering Measurements in Supersonic/Hypersonic Facilities," *28th Joint Propulsion Conference and Exhibit*, AIAA Paper 92-3894, July 1992.

[24]Forkey, J. N., Lempert, W. R., Bogdonoff, S. M., Russell, G., and Miles, R. B., "Volumetric Imaging of Supersonic Boundary Layers Using Filtered Rayleigh Scattering Background Suppression," *32nd Aerospace Sciences Meeting and Exhibit*, AIAA Paper 94-0491, Jan. 1994.

[25]Elliott, G.S., Glumac, N., Carter, C.D., Nejad, A.S., "Two-dimensional temperature field measurements using a molecular filter based technique," *Combustion Science and Technology*, Vol. 125, 1997, pp. 351-369.

[26]Elliott, G.S., Boguszko, M., Carter, C., "Filtered Rayleigh Scattering: Toward Multiple Property Measurements," *39th AIAA Aerospace Sciences Meeting and Exhibit*, AIAA Paper 2001-0301, Jan. 2001.

[27]Boguszko, M., Elliott, G.S., "On the use of filtered Rayleigh scattering for measurements in compressible flows and thermal fields," *Experiments in Fluids*, Vol. 38, 2005, pp. 33-49.

[28]Boguszko, M., Huffman, R., Elliott, G.S., "Property and velocity measurements in a supersonic flow," *44th AIAA Aerospace Sciences Meeting and Exhibit*, AIAA Paper 2006-1390, Jan. 2006.

[29]Huffman, R.E., Boguszko, M., Elliott, G.S., "Mean and Fluctuating Property Measurements with Filtered Angularly Resolved Rayleigh Scattering," *AIAA Journal*, Vol. 49, No. 10, 2011, pp. 2081-2089.

[30]Most, D., Leipertz, A., "Simultaneous two-dimensional flow velocity and gas temperature measurements by use of a combined particle image velocimetry and filtered Rayleigh scattering technique," *Applied Optics*, Vol. 40, No. 30, 2001, pp. 5379-5387.

[31]McManus, T.A., Papageorge, M.J., Fuest, F., Sutton, J.A., "Spatio-temporal characteristics of temperature fluctuations in turbulent non-premixed jet flames," *Proceedings of the Combustion Institute*, Vol. 35, 2015, pp. 1191-1198.

[32]Papageorge, M.J., McManus, T.A., Fuest, F., Sutton, J.A., "Recent advances in high-speed planar Rayleigh scattering in turbulent jets and flames: increased record lengths, acquisition rates, and image quality," *Applied Physics B,* Vol. 115, 2014, pp. 197-213.

[33]McManus, T.A., Sutton, J.A., "Simultaneous 2D filtered Rayleigh scattering thermometry and stereoscopic particle image velocimetry measurements in turbulent non-premixed flames," *Experiments in Fluids,* Vol. 61, No. 134, 2020.

[34]Lee, G. S., "Design and Development of a Wind Tunnel for the Investigation of Turbulent Compressible Mixing Layers," M.S. Thesis, Dept. of Aerospace Engineering, University of Illinois, Urbana, IL, 2017.

[35]Forkey, J.N., Lempert, W.R., Miles, R.B., "Corrected and calibrated I_2 absorption model at frequency doubled Nd:YAG laser wavelengths," *Applied Optics,* Vol. 36, 1997, pp. 6729.

[36]Forkey, J.N., Lempert, W.R., Miles, R.B., "Accuracy limits for planar measurements of flow field velocity, temperature, and pressure using Filtered Rayleigh Scattering," *Experiments in Fluids,* Vol. 24, 1998, pp. 151-162.

[37]Sun, C., and Childs, M. E., "A Modified Wall Wake Velocity Profile for Turbulent Compressible Boundary Layers," *Journal of Aircraft,* Vol. 10, No. 6, 1973, pp. 381–383.

[38]Mathews, D. C., Childs, M. E., and Paynter, G. C., "Use of Coles' Universal Wake Function for Compressible Turbulent Boundary Layers," *Journal of Aircraft,* Vol. 7, No. 2, March-April 1970, pp. 137-140.

[39]Ikawa, H. and Kubota, T., "Investigation of supersonic turbulent mixing layer with zero pressure gradient," *AIAA Journal,* Vol. 13, No. 5, 1975, pp. 566–572.

[40]Chinzei, N., Matsuya, G., Komura, T., Murakami, A., and Kudou, K., "Spreading of Two-Stream Supersonic Turbulent Mixing Layers," *Physics of Fluids,* Vol. 29, No. 5, 1986, pp. 1345–1347.

[41]Elliott, G. S. and Samimy, M., "Effects of Compressibility on the Characteristics of Free Shear Layers," *AIAA Journal,* Vol. 28, No. 3, 1990, pp. 439–445.

[42]Fourguette, D. C., Mungal, M. G., and Dibble, R. W., "Time evolution of the shear layer of a supersonic axisymmetric jet," *AIAA Journal,* Vol. 29, No. 7, 1991, pp. 1123–1130.

[43]Clemens, N.T. and Mungal, M.G., "Large-scale structure and entrainment in the supersonic mixing layer," *Journal of Fluid Mechanics,* vol. 284, 1995, pp. 171–216.

[44]Hall, J., Dimotakis, P., and Rosemann, H., "Experiments in Nonreacting Compressible Shear Layers," *AIAA Journal,* Vol. 31, No. 12, 1993, pp. 2247–2254.

[45]Gruber, M. R., Messersmith, N. L., and Dutton, J. C., "Three-dimensional velocity field in a compressible mixing layer," *AIAA Journal,* Vol. 31, No. 11, 1993, pp. 2061–2067.

[46]Debisschop, J. R., Chambres, O., and Bonnet, J. P., "Velocity Field Characteristics in Supersonic Mixing Layers," *Experimental Thermal and Fluid Science,* Vol. 94, No. 9, 1994, pp. 147–155.

[47]Mehta, R. D. and Westphal, R. V., "Near-field turbulence properties of single and two-stream plane mixing layers," *Experiments in Fluids,* Vol. 4, 1986, pp. 257–266.

[48]Urban, W. D. and Mungal, M. G., "Planar Velocity Measurements in Compressible Mixing Layers," *Journal of Fluid Mechanics,* Vol. 431, 2001, pp. 189–222.

[49]Lazar, E., DeBlauw, B., Glumac, N., Dutton, J. C., and Elliott, G. S., "A Practical Approach to PIV Uncertainty Analysis," *27th AIAA Aerodynamic Measurement Technology and Ground Testing Conference,* AIAA Paper 2010-4355, 2010.

[50]Hortensius, R., "The Fluid-Structure Interaction of an Axisymmetric Underexpanded Jet Flowing Across an Adjacent Compliant Surface," Ph.D. Thesis, Dept. of Aerospace Engineering, University of Illinois, Urbana, IL, 2017.
[51]Weineke, B., "PIV uncertainty quantification from correlation statistics," *Measurement Science and Technology*, Vol. 26, No. 7, 2015, pp. 1–10.

MODEL: CHP0824S-60-74Y-483
SERIAL: 02-2676-1A

DESIGN DATA:
Temperature Limits: -20° F Min., 1175° F Max.
Pressure Limits: -15 PSIG Min., 525 PSIG Max.
Empty Weight of Unit: 800 Pounds
Terminal House Classification: NEMA 12

OPERATIONAL DATA:
Fluid: Air
Fluid Temperature Range: 70°F to 1100°F
Heater Rating: 60 KW on 480 VAC, 3-Phase, 60-Hz, 72 Amp
Heater Watt density: 13.4 Watts/sq. in.
Remarks:
High Temperature Stainless Steel Construction
Type "K" thermocouples used for over-temperature protection
Calcium Silicate Insulation with Stainless Steel Jacket

UTILITIES:
Power: 480 VAC, 3ø, 60 Hz, 100 FLA

Heated Compressible Mixing Layer Facility Standard Operating Procedure Supplement

PPE & Safety Considerations/Checks:

1. At least two people should be present in the lab when running the heated compressible mixing layer facility.
2. All those present must utilize ear and eye protection.
3. Be sure that all PPE is also rated for use with any diagnostic techniques in use (e.g., laser goggles if using lasers).
4. This is a high pressure and temperature facility. As such, care needs to be taken when operating the wind tunnel, especially with the windows. Avoid passing the windows while running, particularly during tunnel startup and shutdown (as shock waves pass the windows at these times). Be cognizant of the potential window blast zone.

Start-up:

1. Verify that all instrumentation is powered on and properly connected. Turn on computer.
2. Verify that the laboratory manifold valve is open and that the wind tunnel manual globe valve is shut.
3. Utilize appropriate PPE (safety glasses and hearing protection are minimums).
4. Ensure that wind tunnel is ready to run. Check the following:
    a. All bolts are installed and tight
    b. All windows are in place and properly secured
    c. All pressure lines and taps are properly plumbed and secured
    d. All data acquisition equipment (i.e., pressure systems) used by the LabVIEW program is turned on, has been allowed to warm up, and is operational. Pressure systems typically require approximately 30 min. to warm up.
    e. Ensure no objects are near the secondary stream inlet when facility is configured to entrain air from the room for the secondary stream.
    f. Heater is plugged in, and both the circuit breakers are turned to allow power through the system. Heater itself is turned on.
    g. All additional experimental equipment is properly secured and readied for operation.
5. Turn on the pressure and temperature measurement box.
6. Note the tank farm pressure, then turn on the compressors (ARL mechanical room) according to their operating procedure.
7. Lock the entrance to GDL and place caution sign on both entrances.
8. Turn on laser light if laser is being operated.
9. Start the LabVIEW control program. Check that there are no errors and that data does record. Do not apply current to the pneumatic valve.
10. Open the valve supplying house air to the wind tunnel control pneumatic valve. Set the regulator to supply air at 80 psi to the control valve. When adjusting pressure, air may vent from the regulator.
11. Open the manual globe valve, and open pneumatic valve slightly to allow a “trickle” flow.
12. Verify that the setpoint for the heater is at the desired temperature. If necessary, change the setpoint.

13. Turn on the heater. While maintaining the “trickle” flow, monitor system status through the LabVIEW program.
14. **Tunnel is now ready to run**. Keep far away from the wind tunnel windows, especially during startup and shutdown (due to passing shock waves). Keep in mind the possible blast zone.
15. Verify LabVIEW mode is set to “Manual” and apply 4 mA of current to the pneumatic valve to open it fully. Then manually open the globe valve to achieve desired stagnation pressures.
16. Conduct your experiment – monitor the tank farm pressure and remember to avoid the windows during operation.
17. At end of experiment, close both manual globe valve and pneumatic valve to “trickle” flow conditions and turn off heater. Monitor system status until system has cooled for at least 15 min. and is at a temperature where flow can be turned off.
18. **Press red “stop” button in LabVIEW to turn off tunnel when desired (standard shutoff or emergency).**
19. Close the manual globe valve fully.
20. Close the house air valve.
21. Depower heater and close circuit breakers.
22. Save both experimental data and LabVIEW run profile data.

Shut-down:

1. STOP the LabVIEW program.
2. Close manual globe valve and pneumatic valve to “trickle” flow settings.
3. Turn off heater.
4. Wait until system temperature has cooled to reasonable level under the trickle flow.
5. Close the manual globe valve fully.
6. Close the house air supply valve.
7. Depower heater.
8. Turn off circuit breakers to heater and unplug.
9. Check condition of the wind tunnel model, windows, seals, etc. **once system has cooled sufficiently.**
10. Turn off other experimental equipment. Shut down computer.
11. Remove caution signs from GDL entrance/exit doors and shut off caution lights.
12. Turn off compressors in the ARL mechanical room according to their operating procedure.

In an emergency:

1. Push the STOP button in the LabVIEW program.
2. Close the manual globe valve. If possible, close to “trickle” flow setting.
3. Turn off heater (throw breaker if necessary).
4. Activate any other emergency kill-switches (or otherwise turn off) any other instrumentation.
5. Call Professor Elliott and, if necessary, emergency responders.

Appendix B: Bill of Materials for Facility Addition of Heater

	Part Name	Size	Length	Material	Notes	McMaster Part #	Amt	Cost
TANK FARM SUPPLY								
Air Supply to Heater	Flange	6		SS 304/304L	Threaded, Forged, Raised	44685K21	1	$ 244.00
	Flange Gasket	6	1/8"	Buna-N		8516T143	1	$ 3.64
	Reducing Flange	6 to 4		SS 304/304L	Threaded, Forged, Raised	44685K134	1	$ 277.88
	Reinforced Hose	4	36"	316 SS (int), 304 SS (braid)	Threaded, 290# rated	5793K3	1	$ 467.31
	Reducing Fitting	4 to 2	1.84"	SS 304/304L	Threaded, 150# rated	4464K187	1	$ 120.18
HEATER								
Heater to Tee	Expanding Fitting	1.5 to 4	1.84"	SS 304/304L	Threaded, 150# rated	4464K615	1	$ 120.18
	Reinforced Hose	4	48"	316 SS (int), 304 SS (braid)	Threaded, 290# rated	5793K3	1	$ 542.91
	Flange	4		SS 304/304L	Threaded, Forged, Raised	44685K19	1	$ 145.25
	Flange Gasket	4	1/8"	Vermiculite	Ultra-Hi-Temp	1089N19	1	$ 78.35
	Flange	4		SS 304/304L	Threaded, Forged, Raised	44685K19	1	$ 145.25
	Pipe	4	4"	SS 304/304L	Threaded	4830K376	1	$ 38.67
	Tee	4		SS 304/304L	Threaded	4464K143	1	$ 212.88
Tee to Ambient	Pipe	4	4"	SS 304/304L	Single-Threaded	9157K503	1	$ 39.23
	Flange	4		SS 304/304L	Unthreaded, Forged	44685K228	1	$ 168.87
	Flange Gasket	4	1/8"	Buna-N		8516T141	1	$ 2.23
	Gate Valve	4	7.66"	Cast Iron / Steel	Flanged, Cl: $ 679.16	49505K54 / 49265K14	1	$ 927.33
Tee to Mixing Layer Facility	Pipe	4	4"	SS 304/304L	Single-Threaded	9157K503	1	$ 39.23
	Flange	4		SS 304/304L	Unthreaded, Forged	44685K228	1	$ 168.87
	Flange Gasket	4	1/16"	Vermiculite	Ultra-Hi-Temp	1089N31	1	$ 153.95
MIXING LAYER FACILITY								
Misc.	Bolts	3/4"-10	6"	Steel	ASTM A193, Grade B7	98750A317	16	$ 41.28
	Bolts	5/8"-18	6"	Steel	ASTM A193, Grade B7	98750A491	16	$ 79.84
						Total (before shipping):		$ 3,896.21

Appendix C: Engineering Drawing of TAT Probe